Spectral Behaviour of
Free Electron Masers

Pieter Jan Eecen

Spectral Behaviour

of

Free Electron Masers

PROEFSCHRIFT

ter verkrijging van de graad van doctor aan de
Technische Universiteit Eindhoven, op gezag
van de Rector Magnificus, prof.dr. M. Rem,
voor een commissie aangewezen door het
College van Dekanen in het openbaar te
verdedigen op donderdag 28 november 1996
om 16.00 uur

door

PIETER JAN EECEN

geboren te Harenkarspel

Dit proefschrift is goedgekeurd door de promotoren:

prof.dr.ir. T.J. Schep

en

prof.dr.ir. H.L. Hagedoorn

Cover Figure:
Artist's impression of nonlinear behaviour
by Christina Maartje Wilhelmina Eecen.

This thesis is based on the following papers

P.J. Eecen, A.V. Tulupov, and T.J. Schep,
"Investigation of multi-frequency generation in the FEM",
Nucl. Instrum. Methods Phys. Res. A 341 (1994) 309.

P.J. Eecen, A.V. Tulupov, and T.J. Schep,
"Spectral Dynamics of the FEM",
Nucl. Instrum. Methods Phys. Res. A 358 (1995) 178.

P.J. Eecen, T.J. Schep, and A.V. Tulupov,
"Spectral Dynamics of a Free Electron Maser
with a Step-Tapered Undulator",
Phys. Rev. E. 52 (1995) 5460.

P.J. Eecen, T.J. Schep, and A.V. Tulupov,
"Spectral Dynamics of a collective Free Electron Maser",
Nucl. Instrum. Methods Phys. Res. A 375 (1996) 190.

P.J. Eecen and T.J. Schep,
"Spectral Dynamics of a collective Free Electron Maser
 with a Step-Tapered Undulator",
Submitted for Publication.

Contents

Chapter 1

Preliminaries

Prologue *The interaction of electromagnetic waves with matter is a fascinating subject of study. Coherent electromagnetic waves from micro-watts to Tera-watts and from X-rays to mm-waves have wide ranging applications. As matter in the universe is mostly in plasma state, the study of electromagnetic waves in plasmas is of importance in many fields of physics. For example, the heating of magnetically confined plasmas to higher temperature with high-power electromagnetic waves and using strong electromagnetic fields in laser fusion [1] revealed exciting physics.*

At present, sources of coherent radiation operate from microwaves to the ultraviolet region. In this thesis, the emission of high-power, electromagnetic radiation by relativistic electrons is considered. A free-electron maser is a free-electron laser in the millimeter range. The actual FEM that is studied in this thesis is being built at Rijnhuizen. This device employs a high density electron beam, therefore, it has plasma-like behaviour. The microwave power can, for example, be used for heating magnetised plasmas. The spectral behaviour of the microwave radiation that is generated by the free-electron maser is quite complicated. The temporal behaviour of the frequency spectrum of the generated radiation is investigated in this thesis.

1.1   General Introduction

A Free-Electron Laser (FEL) [2, 3] is a source of intense, tunable, coherent radiation. Since Madey and co-workers built and operated a free-electron laser device at infrared wavelengths in 1975 [4, 5], lasing has been achieved from near ultra-violet [6] to microwave frequencies [7]. The active medium of a free-electron laser is a high-energy electron beam, instead of an atomic, molecular or crystal system. The employed electron beams have energy from hundreds of kilo-electronvolts to giga-electronvolts. Since the radiation wavelength depends among others on the electron energy, the free-electron laser has the capacity to operate in the frequency range from microwaves to X-rays.

The ingredients of a free-electron laser are an electron gun, an accelerator and an undulator. When the amplification factor (gain) of the radiation field is small an oscillator setup, which uses a cavity, is required. A typical oscillator free-electron laser is shown in Fig. 1.1. An electron gun and an accelerator provide an electron beam at the desired energy. The electron beam is coupled to the co-propagating electromagnetic wave by a spatially periodic magnetic structure, the undulator, that can be of various type and geometry. The planar magnetostatic undulator, that is shown in the figure, consists of two rows of magnets with alternating magnetisation such that a linearly polarised, periodic, magnetic field is available on the axis of symmetry. Each pass, the radiation field interacts with newly injected electrons. The electron beam is separated from the radiation field at the end of the undulator and a fraction of the generated radiation field is coupled out of the cavity [8, 9]. At successive passes through the cavity, the radiation field grows until saturation is reached. The operating frequency of the system that we will investigate will be tuneable over a large frequency range. The tunability of the operating frequency requires a broadband reflecting structure. The intensity of the intra-cavity field builds up initially from spontaneous radiation and grows when the gain of the radiation field is larger than the cavity losses. The steady state is determined by the condition that the saturated gain just balances the cavity losses.

When the gain is very large, the free-electron laser saturates within the interaction length of a single pass. In that case, no cavity is needed. The free-electron laser operates as an amplifier when a seed field is provided by an external source. The FEL operates in SASE (Self Amplified Spontaneous Emission) when there is no externally applied seed field.

The standard periodic structure that deflects the electron beam is an undulator. However, the periodic acceleration of the electron beam can have several origins. For example, when a periodic axial force is applied on the electrons or the dielectric constant for the co-propagating electromagnetic
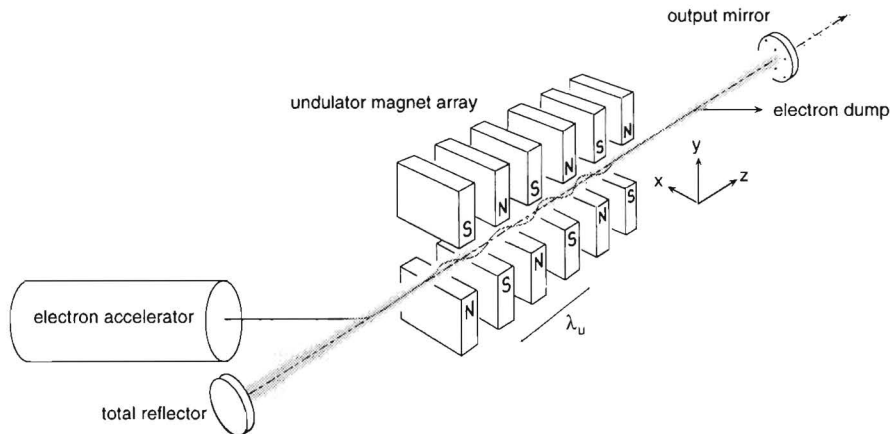
Figure 1.1: *Basic layout of an oscillator free-electron laser. Each pass, newly injected electrons perform an undulating motion in a spatially periodic magnetic field, which causes the electrons to radiate. The radiation is coherently amplified in the undulator during successive passes through the cavity.*

wave is changed periodically, the electrons can also radiate in a coherent way. The free-electron laser is closely related to the Smith-Purcell FEL [10], where the electrons radiate while passing over a grating. The Cherenkov FEL [11] produces coherent radiation from electrons moving superluminously through a periodic medium. These kinds of free-electron lasers are characterised by the interaction of the electrons with the longitudinal component of the electric field. High-power electromagnetic waves [12]–[14] or periodic plasma structures [15] can be used as undulators with extremely short wavelengths. However, only free-electron lasers with planar magnetostatic undulators are discussed in this thesis.

In this thesis the Free-Electron Maser (FEM) [16]–[18] that is under construction at the FOM-Institute for Plasma Physics 'Rijnhuizen' is considered. An FEM is a free-electron laser that operates in the millimeter regime. The FEM is designed to provide continuous millimeter radiation in the range from 130 GHz to 260 GHz with high output power. The high power microwave radiation at these high frequencies will have new applications, for example, the radiation can be used for heating of magnetised (tokamak) plasmas. An overview of the FEM is presented in Chapter 3.

1.2   Principles of the FEL operation

In the free-electron laser, a high-energy electron beam is injected into a periodic magnetic structure, the undulator. This field is the predominant contribution to the electromagnetic field that acts upon the electrons. It forces an oscillatory motion on the electrons that is perpendicular to the direction of propagation. The electrons that perform a transversely wiggling motion produce dipole radiation. This 'spontaneous' radiation [19, 20] is emitted in a small forward cone. The spontaneous radiation is incoherent and weak, but it fulfils an important role in the startup of the free-electron laser. This radiation field provides the seed field for the interaction.

The radiation field has the same polarisation as the undulator field. These fields combine to form the so-called ponderomotive wave. The frequency of this wave is the same as the one of the electromagnetic field (ω) and its wavenumber is the sum of the wavenumbers of the electromagnetic (k) and undulator (k_u) fields. The ponderomotive wave has a lower phase velocity than light in vacuo and is in synchronism with electrons with axial velocity v_z that satisfies

$$v_z = \frac{\omega}{k + k_u}. \tag{1.1}$$

In first instance, electrons with axial velocity v_z are in resonance with the ponderomotive wave and experience a nearly constant force in the direction of the bottom of the ponderomotive potential well. This axial Lorentz force perturbs the electron beam density and causes bunches. The transverse current density is determined by the velocity that is induced by the undulator field times the charge density. The averaged charge density does not contribute to the current density because initially the electrons are evenly distributed in the ponderomotive potential. The perturbed charge density, on the other hand, is periodically perturbed with wavenumber $k + k_u$ and frequency ω. In combination with the undulator induced velocity, the perturbed density generates a transverse current with wavenumber and frequency equal to (ω, k). This is the source for transversely polarised, coherent radiation [21]–[23] that is in phase with the existing radiation. In the case of low electron beam densities, the coherent radiation spectrum is strongly peaked for frequency and wavenumber (ω, k) that satisfy both the dispersion relation for the electron beam wave $\omega = v_z(k + k_u)$ and the electromagnetic wave $\omega = ck$. Therefore, the resonant wavelength λ is

$$\lambda = \lambda_u \frac{1 + \frac{1}{2}a_u^2}{\beta_z(1 + \beta_z)\gamma^2}, \tag{1.2}$$

where the pump parameter $a_u = eB_u/(m_e c k_u)$ is proportional to the maximum amplitude of the undulator field on axis B_u and $\lambda_u = 2\pi/k_u$ is the undulator period. The averaged normalised axial velocity $\beta_z = v_z/c$ is close to unity. When all electrons start at the resonant energy, an equal number of electrons is decelerated as is accelerated, and on average, there is no amplification of radiation. Electrons in near resonance with the ponderomotive wave lose energy to the wave if their velocity is slightly larger than the phase velocity of the wave, and gain energy at the expense of the wave in the opposite case. When, on average, the electrons initially have slightly higher energies than the resonant energy, the interaction leads to spatial growth of the radiation field. The growth rate is proportional to a power of the coupling constant between the two waves.

1.2.1 Effects of the Density

In the outline of the free-electron laser interaction in the previous Section, Coulomb forces between the electrons are assumed to be negligibly small. The larger the charge and current density and the lower the energy γ of the employed electron beam, the more pronounced the effects of Coulomb forces are, as will be shown later. The axially perturbed beam density is a source for Poisson's equation and starts to play a role when it is sufficiently large. When the electron beam is bunched, this leads to repulsive Coulomb forces within these bunches. Then the free-electron laser operation is different than described above. The Coulomb forces lead to wave-like disturbances in the electron beam: these are called space-charge or plasma waves. The dispersion relation for the electron beam wave is split into a positive and negative-energy space-charge wave. It turns out that the negative-energy space-charge wave is unstable and lasing interaction takes place when the electromagnetic wave interacts with that branch. The coupling between these waves is determined by a number of undulator and beam parameters. The value of the coupling parameter determines the growth rate of the radiation field. Two operating regimes are distinguished, depending on whether the interaction between the electrons is negligible or not.

When the Coulomb forces between the electrons are negligibly small, the electrons can be treated as single particles and the free-electron laser operates in the single-particle regime as is described in Section 1.2. An FEL operates in this regime when the ponderomotive potential dominates the space-charge potential (see Section 2.3),

$$
\frac{\omega_p}{c k_u \gamma_z \sqrt{\gamma}} \ll \frac{\gamma_z^2}{16\gamma^2} a_u^2, \tag{1.3}
$$

where the plasma frequency in the frame of reference moving with the electrons $\omega_p^2 = n_0 e^2 / (\epsilon_0 m_e)$ is proportional to the electron beam density n_0. Free-electron lasers operating in this regime generally apply high-energy electron beams and usually operate at wavelengths from the infrared down to the visible. This regime is also called the strong-pump regime, which is obvious from the condition (1.3). The interaction can also be viewed at as a scattering process. The electrons experience the undulator as a backward propagating wave, that can scatter off a forward propagating electromagnetic wave. When the radiation field is scattered of single electrons, the FEL operates in the so-called Compton regime. In the case the density is so high that the gain of the radiation is exponential, the FEL is said to operate in the high-gain Compton regime.

When the density is so high that the electrostatic potential due to the electron beam space-charge wave is dominant over the ponderomotive potential,

$$\frac{\omega_p}{ck_u\gamma_z\sqrt{\gamma}} \gg \frac{\gamma_z^2}{16\gamma^2}a_u^2, \tag{1.4}$$

the electron beam behaves as a collective electron plasma. The space-charge fields result in electrostatic waves that co-propagate with the electron beam. Radiation is no longer scattered from single electrons as in the high-gain Compton regime, but rather from plasma waves. The interaction results from a stimulated three-wave scattering process. The electrons experience the undulator as a backward propagating wave, that can scatter off the negative-energy space-charge wave to produce a forward propagating electromagnetic wave. The resulting operating wavelength is

$$\lambda = \frac{\lambda_u \left(1 + \frac{1}{2}a_u^2\right)}{\beta_z(1+\beta_z)\gamma^2 \left(1 - \dfrac{\omega_p}{\gamma_z\sqrt{\gamma}ck_u\beta_z}\right)}, \tag{1.5}$$

which is red shifted with respect to the operating wavelength in the Compton regime (1.2). In analogy with atomic Raman scattering [24], this regime is called the Raman regime. Free-electron lasers operating in this regime usually apply a low-energy electron beam and operate at long wavelengths. The Raman regime is also referred at as weak-pump regime. The second term in parentheses in the denominator we will refer at as Raman frequency shift.

There are generally two additional criteria [25] to determine whether the free-electron laser operates in the Raman regime. One criterium required for space-charge effects to be important is that the Raman frequency shift

must exceed the line width due to the finite number of undulator periods. The physical interpretation of this criterium is that the undulator must be long enough for several plasma oscillations to occur during the course of the interaction. Another criterium is that the Landau damping of the space-charge waves due to the thermal spread of the electron beam must be small. When the wavelength of the space-charge wave is of the order of the Debye length, the wave is strongly damped. The Debye length [26] is the longitudinal distance a thermal electron travels with respect to the (high) average axial velocity within the time ω_p^{-1} and is determined from the energy spread and emittance of the electron beam.

Between the high-gain Compton regime and Raman regime there is an intermediate regime, where the space-charge potential is of the same order as the ponderomotive potential. In the intermediate regime, unstable interaction occurs at the intersection of the negative-energy space-charge wave and the electromagnetic wave in the dispersion diagram. As the axial bunching of the electrons in the ponderomotive potential well grows, the radiation field is amplified and, accordingly, the corresponding longitudinal space-charge field grows. The space-charge field counteracts the bunching process of the free-electron laser interaction and reduces the growth rate.

The FEM, to be described in this thesis, employs an electron beam that has an energy of 1.75 MeV and a current of 12 A. With these parameters the space-charge potential is of the same order as the ponderomotive potential. Therefore, the FEM operates in the regime between the high-gain Compton and the Raman regime. The Raman frequency shift exceeds the line width of the microwave field. The wavelength of the space-charge wave is more than 10 times larger than the Debye length. This means that the negative-energy space-charge wave is not strongly damped. The corresponding space-charge forces strongly influence the interaction, resulting in a strong reduction of the gain. This intermediate regime is investigated in this thesis.

At start-up, in the absence of radiation, the growth of the radiation field is determined by the spontaneous emission. This field is the seed field for the stimulated emission of radiation, that at first grows due to interference. The power of the radiation field increases as the cube of distance z [27]. This complicated phase of the interaction is determined by the power level of the spontaneous emission and the gain of the device. The exponentially growing part of the stimulated emission quickly dominates the interaction in the device that is considered here.

1.2.2   The Step-Tapered Undulator

The extraction efficiency is the ratio of the energy transferred to the microwave field and the initial electron energy. The maximum extraction efficiency is reached when all electrons have travelled to the bottom of the potential well. In order to amplify the radiation field again with these electrons, the potential well must be deepened, or equivalently, the resonant energy must be reduced. This can be achieved by so-called 'tapering' of the undulator, which can be produced in several ways. In the FEM, the step-tapered undulator consists of two planar magnetostatic undulators. The undulator field of the second section is smaller. This way, the electrons, while emitting radiation, experience a deepened potential well in the second section and the efficiency of the microwave generation is improved. This is illustrated in Fig. 1.2, where the positions of the electrons in phase space are plotted at the end of the first and second section of the undulator, respectively. These results are obtained from the code MFF that is described in Chapter 3. The energy of the electrons is given as a function of the relative position of the electrons in the ponderomotive well, the ponderomotive phase. The resonant energies for both sections are indicated by γ_{r1} and γ_{r2}. The upper plot of Fig. 1.2 shows the electron distribution in phase space at the end of the first section. The microwave field has been amplified and, on average, the electrons are at lower energies. When the undulator would be longer, the electrons, that are trapped in the ponderomotive potential well, would rebound and gain energy at the expense of the microwave field. Like a pendulum, the trapped electrons loose and gain energy as they rise and fall in the stable area. In the second section a potential well is generated with lower resonant energy ($\gamma_{r2} < \gamma_{r1}$). As is shown in the middle plot of Fig. 1.2, the electrons again lose energy and amplify the microwave beam further. Thus, the second section increases the extraction efficiency. Correspondingly, the output power is increased. This is indicated in the third plot of Fig. 1.2, where the extraction efficiency (thick line) is given as a function of the axial position in the undulator. It shows the saturation of the radiation field at the end of the first section. The second section amplifies the radiation field further and the radiation field saturates again at higher energy. For the step-tapered undulator that is considered in this thesis and is described in Chapter 3, the following numbers apply. The first section of this step-tapered undulator operating as a single-section undulator can achieve a maximum extraction efficiency at saturation of approximately 2.7%. This is shown in Section 6.2.1. The electron efficiency at saturation of the step-tapered undulator exceeds 6%.

The phase-space plots of the electrons in Fig. 1.2 visualise the formation of bunches. The longitudinal electric field that is associated with these
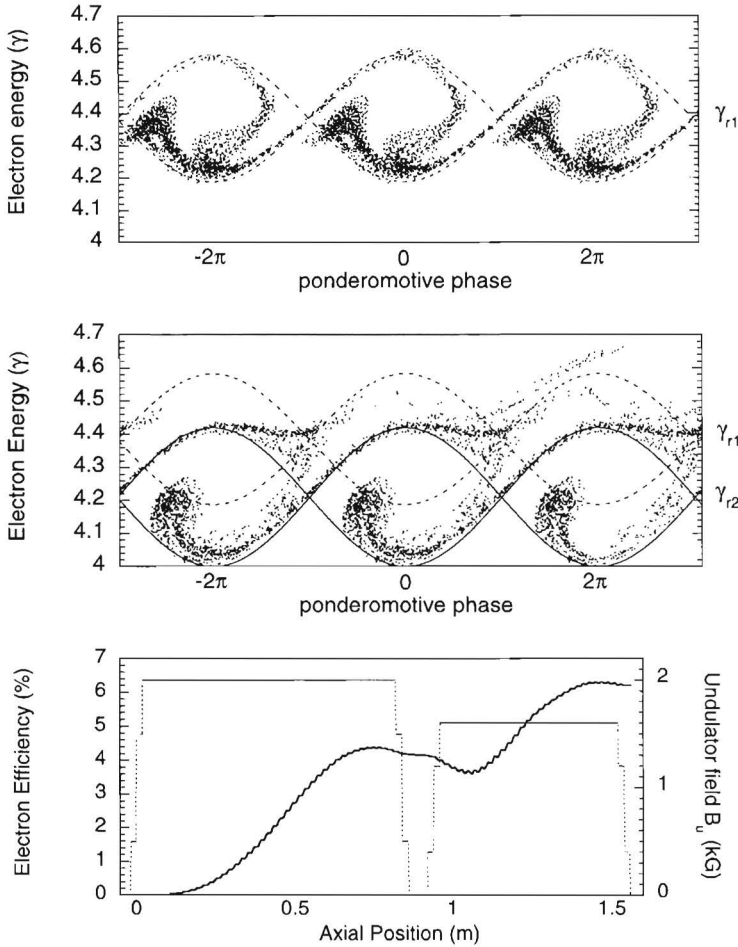
Figure 1.2: *In the upper figures, snap shots of the evolution of the electrons in phase space are plotted at the end of the first and second section of the step-tapered undulator employed in the FEM, respectively. The ponderomotive phase is a measure for the position of the electrons in the ponderomotive potential well. The separatrix, that separates the trapped and untrapped electrons, is indicated by the dashed line for the first section of the undulator, and by the solid line for the second. At the end of the first section, the electrons have minimum kinetic energy. The resonant energy in the second section is lower than the corresponding one in the first section. This means that the electrons can loose energy again so that the microwave field can be amplified again. In the lower figure, the extraction efficiency is shown by the thick line, which is proportional to the output power and is strongly increased in the second section. Also the undulator field strength (thin line) as a function of the axial position is indicated.*

bunches induces a repulsive force within these bunches. Therefore these fields counteract the bunching process, reducing the growth of the radiation field.

1.3   Spectral Dynamics of the FEM

An important question that is addressed in this thesis is whether the free-electron maser can generate microwave power within a small bandwidth. In the previous outline of the free-electron laser mechanism we silently adopted a single-frequency approach. However, this is a dangerous approach because the spectral evolution of the radiation is complicated. There are a number of reasons why a multi-frequency treatment is required. The spontaneous emission from a step-tapered undulator is emitted at two wavelengths and several interference peaks (see Section 4.2). After a while, the stimulated emission dominates the spontaneous emission. During the start-up of the interaction, the field amplitude is low. Then the bunching of the electrons is small and the gain of each frequency component of the field is independent of the initial power. That determines a linear gain curve. The maximum value is large; the undulator is a few number of gainlengths long. The different undulator field strengths result in different resonant frequencies for both sections. Additionally, the field-free gap between the two sections of the step-tapered undulator introduces a change in the relative phase of the electromagnetic field and the undulator. As a result, the small-signal gain curve exhibits multiple peaks as will be shown in Chapter 5. These peaks are well separated. The FEM has an oscillator setup and the value of the peaks in the gain curve can be larger than the inverse of the reflection coefficient. The peak in the linear gain curve corresponding to the resonant position of the first section is the largest and grows fastest over the passes through the cavity. The width of this peak in the linear gain curve is several percent of the central frequency. We would like to address mode competition. Although the frequency components that we use to describe the microwave field are not 'pure' modes of operation, the competition between the various microwave frequency components is called mode competition. In the small-signal regime there is no mode competition and in this regime, the growth of each component is exponential and independent of its initial power and the power in the other frequency components.

The FEM has a low-quality cavity that reflects less than a third of the intra-cavity power. This power is used as input field for the next pass through the undulator. Hence, in order to compensate for the outcoupled power, the gain remains large in the stationary regime. The consequence of a low-quality cavity is that the cavity hardly improves the selection of a specific cavity

mode. Accordingly, because of the low-quality cavity one would expect the microwave power to be generated in a broad spectrum.

At the onset of saturation, the gain of all frequency components start to level off. As the field grows in amplitude, the interaction process becomes highly nonlinear and the field grows to saturation. In this nonlinear regime, mode competition occurs and the second section of the undulator behaves more and more as an amplifier of the microwave field generated in the first section. This modifies the spectral characteristics of the gain. The determination of the frequency to which the radiation field evolves after multiple passes through the system is a non-trivial problem. The peak in the linear gain spectrum and in the nonlinear gain spectrum are at different frequencies. Although the system starts at the frequency of maximum linear gain, it turns out that the system evolves toward lower operating frequency. This shift of the operating frequency goes hand in hand with competition between the various frequency components of the microwave field.

As is sketched in the foregoing, the spectral behaviour of the free-electron maser is rather complicated. The FEM operates with a large gain both in the linear and in the nonlinear regime; therefore, when complicating instabilities occur, they may grow rapidly. The investigation of the spectral dynamics of the free-electron maser is interesting and necessary for the final performance. The stable operation in a narrow frequency band is a crucial requirement for the success of the FEM. In Ref. [28], it was pointed out that in multi-mode calculations there is the possibility of unstable operation. In Ref. [29] it is shown that, when space-charge fields are included, multimode excitation can be avoided by properly adjusting the system parameters. Important parameters that influence the spectral behaviour are the length of the field-free gap and the reflection coefficient. These calculations are one-dimensional. In this thesis, calculations of the spectral dynamics of the FEM are done with a newly developed numerical code, that is called the multi-frequency FEM (MFF) code and is described in Chapter 3. The electron orbits are calculated three-dimensionally and the electromagnetic fields are calculated two dimensionally. The AC-space-charge fields as well as the DC-space-charge fields are included in the code. The equations are not averaged over an undulator period. The slippage of the electrons with respect to the microwave field is included in the code through the setup of the model. Different portions in the microwave beam at different longitudinal positions are able to communicate with one another through this process of slippage.

We will show in Chapter 5 and 6, that the generated spectrum evolves generally toward a very small bandwidth, that is smaller than one would expect from the previous considerations. The power in the frequency components around the resonant frequency of the second section is effectively

suppressed by the interaction. This is a nonlinear process and occurs at an early stage. The behaviour of the generated spectrum as the interaction evolves from the small-signal (linear) to the large-signal (nonlinear) regime is quite complicated. The numerically observed spectral behaviour cannot be predicted by single frequency calculations. Furthermore, it will be shown that three-dimensional effects, like the oscillations of the electron beam radius (see Section 2.2.1), have large influence on the spectral behaviour.

The mode competition has been studied analytically for long pulse FELs [30, 31]. In these Refs. the mode-competition is determined by an artificial, ad-hoc coupling parameter between the frequency components and single frequency operation of a long-pulse FEL is predicted. As we will show in this thesis, this description is far from complete and various mechanisms will complicate the evolution of the frequency components of the microwave field. The conditions under which a FEL operates in a 'single-moded' spectrum is addressed by various other authors. In Refs. [33, 34] a one-dimensional model is used to parameterise the regime where single-mode operation in a low-gain oscillator is possible. Extensive multi-frequency studies are reported in Refs. [35]–[37], where perturbation expansions in the radiation field as well as in the density is taken. An oscillator setup is described in the Compton limit. The latter Refs. describe an oscillator setup in the Compton limit and similar characteristics of the evolution of the power spectrum is found as is reported in this thesis.

In this thesis a multi-frequency description is presented that describes the power spectrum in the small-signal as in the large-signal regimes. The microwave field may vary considerably over the interaction length and space-charge forces are included. The coupling between the various frequency components of the radiation field is self-consistently incorporated through the electron motion, that is calculated in the six-dimensional phase-space. A microwave field that consists of various frequency components is time-dependent. Therefore, the region in time that is described in the code is large and slippage of the electrons with respect to the microwave field is important.

1.4   Outline of the Thesis

In the next Chapter, the basic equations are given that govern the free-electron laser interaction. The discussion is restricted to the system with the magnetostatic undulator with a planar configuration. All fields that influence the free-electron laser interaction are discussed and special attention is paid to the effects of the electron beam density. The related space-charge waves

lead to the effects that are described in Section 1.2.1. The dispersion relation gives the conditions for operation in the different regimes. The phase-space evolution is discussed in order to derive the saturation efficiencies and to show the effects of tapering. Finally, the multi-frequency description of the free-electron laser interaction is presented. The microwave field is expanded into transverse waveguide modes and into longitudinal cavity modes. The latter expansion is valid near a central cavity mode. The longitudinal space-charge field has a large effect on the interaction. This field is generated and amplified as the bunching of the electrons develops. This field counteracts the bunching process, as is described before.

The numerical free-electron maser is described in Chapter 3. The spectral dynamics of the free-electron maser for fusion applications is calculated with the numerical code MFF. The various components of this FEM are shortly discussed. A key element of the FEM is the step-tapered undulator. The code MFF includes the various frequency components of the microwave field that interact with the negative-energy space-charge waves of the electron beam. Both the AC and the DC-space-charge fields are self-consistently included in the code.

In Chapter 4, the evolution of the spectrum of a step-tapered undulator in the Compton limit is investigated. This way, the highly nonlinear evolution is studied without the complicating effects of the longitudinal space-charge fields. Since the space-charge fields are disregarded, the linear gain is quite large. The large signal regime is quickly reached and the spectral behaviour exhibits heavy mode competition. It is found that the sideband at lower frequencies than the frequency of the main peak in the power spectrum actually improves the extraction efficiency by acting as an intermediary in phase-space between the potential wells corresponding to the first and second section of the undulator. An investigation of the sideband behaviour is presented. The spontaneous emission spectrum of the step-tapered undulator is derived that is valid for low-energy electron beams.

The results of numerical calculations with the MFF code, including all space-charge fields are presented in Chapter 5. The fast-oscillating longitudinal (AC) space-charge forces counteract the bunching process and the slowly-varying equilibrium (DC) space-charge forces enlarge the electron beam radius. The linear gain spectrum exhibits multiple peaks. The actually measured frequency profile of the reflection coefficient is used in this Chapter. The spectral evolution is calculated in the ranges of 130, 200, and 250 GHz. It is found that after a complicated phase with mode-competition, narrow single-peaked power spectra are excited. The width of the power spectrum is a few GHz. In order to reach maximum output power, the maximum value of the reflection coefficient should be positioned where $\Delta\gamma/\gamma$ is maximum,

which is a few GHz below the frequency corresponding to maximum linear gain. The fast tunability of the operating frequency of the FEM, keeping the profile of the reflection coefficient fixed, is investigated.

In Chapter 6, the evolution of the power spectrum is investigated for a flat profile of the reflection coefficient. As the microwave field grows in successive roundtrips through the cavity, the the response of the system at the resonant frequency of the second section disappears and the main peak shifts toward the frequency in the spectrum where maximum extraction efficiency occurs. A multi-peaked power spectrum is generated. By comparing these results with the results obtained with a narrow profile of the reflection coefficient as are shown in Chapter 5, the influence of the frequency profile of the reflection coefficient is investigated. The role of the fast oscillating longitudinal space-charge fields on the spectral dynamics is investigated by comparing the spectral evolution when all space-charge forces are disregarded (see Chapter 4) with the case that the DC-forces are neglected and only the fast oscillating longitudinal space-charge fields are taken into account. It is found that the DC-forces have a large effect on the spectral evolution.

References of Chapter 1

[1] W.L. Kruer, *The physics of laser plasma interactions*, (Addison-Wesley, 1987).

[2] T.C. Marshall, *Free-Electron Lasers*, (Macmillan, New York, 1985).

[3] C.W. Robertson and P. Sprangle, "Review article, A review of free-electron lasers", Phys. Fluids B **1** (1989) 3.

[4] L.R. Elias, W.M. Fairbank, J.M.J. Madey, H.A. Schwettmann, and T.I. Smith, "Observation of stimulated emission of radiation by relativistic electrons in a spatially periodic transverse magnetic field", Phys. Rev. Lett. **36** (1976) 717.

[5] D.A.G. Deacon, L.R. Elias, J.M.J. Madey, G.J. Ramian, H.A. Schwettmann, and T.I. Smith, "First operation of a free-electron laser", Phys. Rev. Lett. **38** (1977) 892.

[6] W.B. Colson, "Short wavelength free-electron lasers in 1994", Nucl. Instrum. Methods A **358** (1995) 555;
W.B. Colson, "Short wavelength free-electron lasers in 1996", Nucl. Instrum. Methods A **375** (1996) 669.

[7] H.P. Freund and V.L. Granatstein, "Long wavelength free-electron lasers in 1994", Nucl. Instrum. Methods A, **358** (1995) 551;
H.P. Freund and V.L. Granatstein, "Long wavelength free-electron lasers in 1995", Nucl. Instrum. Methods A **375** (1996) 665.

[8] D.E. McCumber, "Eigenmodes of a symmetric cylindrical confocal laser resonator and their perturbation by output-coupling apertures", Bell System Technical Journal **44** (1965) 333-363.

[9] B. Faatz, R.W.B. Best, D. Oepts, and P.W. van Amersfoort, "Hole coupling in free-electron lasers", IEEE J. Quantum Electron. **QE-29** (1993) 2229.

[10] S.J. Smith and E.M. Purcell, Phys. Rev. **92** (1953) 1069.

[11] J. Walsh, T.C. Marshall, and S.P. Schlesinger, "Generation of coherent Cerenkov radiation with an intense relativistic electron beam", Phys. Fluids **20** (1977) 709.

[12] J. Gea-Banacloche, G.T. Moore, R.R. Schlicher, M.O. Scully, and H. Walter, "Soft X-ray free-electron laser with a laser undulator", IEEE J. Quantum Electron. **QE-23** (1987) 1558.

[13] E. Esarey, P. Sprangle, and A. Ting, "Laser synchrotron radiation as a compact source of tunable, short pulse hard X-rays", Nucl. Instrum. Methods A **331** (1993) 545.

[14] I. Kimel and L. Elias, "A compact, bright and tuneable CW source of soft X-rays", Nucl. Instrum. Methods A **358** (1995) 20.

[15] T.J. Schep, A.V. Tulupov, V.A. Bazylev, and V.V. Goloviznin, J. Phys. D.: Appl. Phys. **28** (1995) 1.

[16] W.H. Urbanus, R.W.B. Best, W.A. Bongers, A.M. van Ingen, P. Manintveld, A.B. Sterk, A.G.A. Verhoeven, and M.J. van der Wiel, "Design of the 1 MW, 200 GHz, FOM fusion FEM", Nucl. Instrum. Methods A **331** (1993) 235.

[17] W.H. Urbanus et. al., "A 130-260 GHz, 1 MW free-electron maser for fusion", Nucl. Instrum. Methods A **358** (1995) 155.

[18] A.G.A. Verhoeven, W.A. Bongers, C.A.J. van der Geer, P. Manintveld, F.C. Schüler, W.H. Urbanus, and M.J. van der Wiel, "A broad-tuneable free electron maser for ECW applications", Proceedings of the ninth joint workshop on electron cyclotron emission and electron cyclotron heating, Borrego Springs, California, (1995) 309.

[19] N.M. Kroll, "Relativistic synchrotron radiation in a medium and its implications for stimulated shock radiation", in *Physics of Quantum Electronics: Free-electron Generators of Coherent Radiation*, Vol. 7 (1980) 335.

[20] J.M.J. Madey, "Relationship between mean radiated energy, mean squared energy and spontaneous power spectrum in a power series expansion of equations of motion in a free-electron laser", Nuovo Cimento **50B** (1979) 64.

[21] T. Kwan, J.M. Dawson, and A.T. Lin, "Free-electron laser", Phys. Fluids **20** (1977) 581.

[22] N.M. Kroll and W.A. McMullin, "Stimulated emission from relativistic electrons passing through a spatially periodic transverse magnetic field", Phys. Rev. A **17** (1978) 300.

[23] P. Sprangle, R.A. Smith, and V.L. Granatstein, in *Infrared and millimeter waves*, Vol. 1, ed. K.J. Button (Academic Press, New York, 1979), p. 279.

[24] P.W. Milonni and J.H. Eberly, *Lasers*, (John Wiley & Sons, 1988).

[25] H.P. Freund, "Space-charge effects in free-electron lasers", Nucl. Instrum. Methods A **331** (1993) 496;
H.P. Freund and T.M. Antonsen, jr, *Principles of free-electron lasers*, (Chapman and Hall, 1992).

[26] J.D. Jackson, *Classical Electrodynamics, second edition*, (John Wiley & Sons, Inc., 1975).

[27] H.P. Freund, P. Sprangle, D. Dillenburg, E.H. da Jordana, B. Liberman, and R.S. Schneider, "Coherent and incoherent radiation from free-electron lasers with an axial guide field", Phys. Rev. A **24** (1985) 1965.

[28] V.L. Bratman and A.V. Savilov, "Competition of longitudinal modes and the scenario of single-mode regime build-up for the FOM-Fusion-FEM project", Nucl. Instrum. Methods A **358** (1995) 182.

[29] M. Caplan, T. Antonsen, B. Levush, A. Tulupov, and W.H. Urbanus, "Predicted operating conditions for maintaining mode purity in the 1 MW 200 GHz FOM free electron maser", Nucl. Instrum. Methods A **358** (1995) 174.

[30] I. Kimel and L.R. Elias, "Mode competition in long-pulse FELs", Nucl. Instrum. Methods A **285** (1989) 132.

[31] I. Kimel and L.R. Elias, "Computer simulation of mode evolution in long pulse FELs", Nucl. Instrum. Methods A **341** (1994) 191.

[32] J.C. Gallardo, L.R. Elias, G. Dattoli, and A. Renieri, "Integral equation for the laser field in a long-pulse free-electron laser", Phys. Rev. A **36** (1987) 3222.

[33] T.M. Antonsen, Jr and B. Levush, "Mode competition and suppression in free electron laser oscillators", Phys. Fluids B **1** (1989) 1097.

[34] B. Levush and T.M. Antonsen, Jr, "Nonlinear mode competition and coherence in low gain FEL oscillators", Nucl. Instrum. Methods A **285** (1989) 136.

[35] D. Iracane and H. Delbarre, "Stability of a free-electron lasers spectrum in the continuous beam limit", Phys. Rev. Lett. **66** (1991) 33.

[36] D. Iracane, P. Chaix, and J.L. Ferrer, "Spectral behavior of high-power Compton free-electron lasers. I. Broadening and asymptotic equilibrium", Phys. Rev. E **49** (1994) 800.

[37] D. Iracane, P. Chaix, and H. Delbarre, "Spectral behavior of high-power Compton free-electron lasers. II. Effect on filtering and tapering on sideband generation", Phys. Rev. E **49** (1994) 815.

[38] Ya.L. Bogomolov, V.L. Bratman, N.S. Ginzburg, M.I. Petelin, and A.D. Yunakovsky, Opt. Commun. **36** (1981) 209.

[39] W.B. Colson and R.A. Freedman, Opt. Commun. **46** (1983) 37.

Chapter 2

Theoretical Framework

Abstract *A short survey is presented of the theory of the free-electron laser. The assumptions and approximations that are made to describe the fields and the electron beam in the free-electron laser are introduced. The effects of focussing and self-fields on the electron motion in the absence of radiation are discussed. Subsequently, the equations are derived that describe the free-electron laser interaction. The electron beam density modifies the dispersion relation for the electromagnetic wave and the electron beam wave. The generation of stimulated coherent radiation as a function of the electron beam density is discussed. The beam density largely determines the operating regime with its specific growth rate of the radiation field. A step-tapered undulator is considered which has a complicated linear gain spectrum. This undulator enhances the final efficiency at saturation. The radiation is generated in a broad spectrum and the gain is high in the small-signal and large-signal regime. The spectral dynamics of the free-electron maser are studied. The multi-frequency formalism of the free-electron laser interaction is presented. In this formalism, the microwave field is represented as a sum over cavity modes that satisfy the paraxial wave-equation.*

2.1   Introduction

The free-electron laser is a device that amplifies coherent radiation by a beam of relativistic electrons passing through a periodic transverse magnetic field [1]-[6]. The radiation source is continuously tuneable in operation frequency. The free-electron laser was first envisioned by Motz [7, 8] who showed analytically that an electron beam wiggling through a magnetic undulator will amplify coherent radiation. The amplification process that he described became the physical basis for the free-electron laser mechanism. In 1960, Phillips [9, 10] first demonstrated the ubitron (Undulating Beam Interaction), a microwave source based on this mechanism. However, one of the problems with these devices was the quality of the electron beam and the full potential of the free-electron laser was not recognised. It was only in 1970 that the quantum description of the free-electron laser interaction by Madey [11, 12] placed the free-electron laser in the spotlight. Quantum mechanics of the free-electron laser have been studied since then [13]-[16]. For most applications of practical interest, quantum mechanical effects are negligible and the free-electron laser is well described by classical electrodynamics [17]. In this thesis the description of the interaction in the free-electron laser is described with Maxwell's equations and classical mechanics. In 1975, Madey and co-workers built and operated a device at infrared wavelengths [18, 19], that they called a free-electron laser. Since then, interest in free-electron lasers grew and lasing has been achieved from visible to microwave frequencies [20, 21].

Pursuing the formalism of a multi-frequency treatment of the free-electron maser interaction, the following subjects are addressed in this Chapter. The basic equations that govern the free-electron laser interaction are presented. The important contributions to the electromagnetic field are discussed. These fields are solutions of Maxwell's equations and the source terms are determined by the electron dynamics, described with Hamiltonian equations of motion. The equations of motion in the absence of radiation [22]-[24] reveal the effects of slowly-varying self-fields and the effects of the inhomogeneous undulator field. This periodic motion is the source for spontaneous radiation [25]-[30] in a narrow forward cone of angular width $1/\gamma$. This relatively weak incoherent radiation often is the seed field for the coherent free-electron laser mechanism. The stimulated emission of free-electron lasers is analysed by investigating the dispersion relation. The dispersion relation reveals the characteristics for the various operating regimes. When the electron energy is high and the current density is low, the free-electron laser operates in the low-gain Compton regime, that is well described by a pendulum equation [31, 32]. According to Madey's theorem [27], the gain in an FEL is propor-

tional to the derivative of the spontaneous emission spectrum with respect to the electron energy and, therefore, with respect to the radiation frequency of the spontaneous emission. When high-current electron beams are employed, the free-electron laser operates in the exponential gain regime. The free-electron laser operates in the high-gain Compton regime [33] when the ponderomotive potential dominates the space-charge potential. In that case, collective effects can be neglected. When the current density is larger and the electron energy lower, the effects of the Coulomb forces are larger. When the space-charge potential dominates the ponderomotive potential, the free-electron laser operates in the Raman regime [34]–[37]. In this regime, the unstable space-charge wave modifies the interaction to a three-wave interaction. The charge and current density have their effect on the propagation of electromagnetic and the space-charge waves through the electron beam. Linear theory [37]–[39] reveals the behaviour of the density perturbation as the electrons experience a force due to the ponderomotive potential well. This leads to a dispersion relation that is a tool to distinguish the operating regimes of the free-electron laser. In these regimes, the growth rates and the maximum efficiency at saturation can be determined for a standard undulator.

However, the maximum efficiency at saturation can be enhanced in several ways. For example, one can decrease the undulator field along the beam, while keeping the undulator period fixed [40, 41]. This thesis considers the step-tapered undulator, consisting of two sections with equal periodicity and polarisation. The undulator amplitude of the second section is smaller than the amplitude of the first. This introduces a taper in one step that considerably enhances the efficiency. The two sections of the step-tapered undulator have different resonant frequencies, therefore, the linear gain curve has multiple peaks. This makes the evolution of the spectrum an interesting object of investigation. The nonlinear evolution towards higher power in a low-quality cavity, that reflects only 30% of the power at the end of the interaction length can lead to fast growing instabilities, such as the sideband instability. An intrinsic property of the free-electron laser interaction is that the frequency at which there is maximum linear gain and the frequency at which there is maximum extraction efficiency at saturation are different. Shifting the operating frequency from highest linear gain to highest extraction efficiency is accompanied by mode-competition. Any other spectral phenomena, like sidebands go together with increased mode-competition. The investigation of the spectral dynamics of the free-electron maser is therefore interesting and necessary. A number of studies considering the behaviour of spectral dynamics of free-electron lasers have been performed in [42]–[45].

2.2   Basic Equations

We describe the particle motion with a Hamiltonian formalism. The sum over all particle positions and velocities give the source terms that describe the process of stimulated emission of the free-electron laser in Maxwell's equations. In this thesis the electron beam propagates in the positive z-direction. The wave equations for the normalised electromagnetic potentials are

$$\left(\nabla_\perp^2 + \partial_z^2 - \partial_{ct}^2\right)\boldsymbol{a} = -\frac{e}{\epsilon_0 m_e c^3}\boldsymbol{J}, \tag{2.1}$$

$$\left(\nabla_\perp^2 + \partial_z^2 - \partial_{ct}^2\right)\varphi = -\frac{e}{\epsilon_0 m_e c^2}\rho, \tag{2.2}$$

where (in cartesian coordinates) the transverse gradient is $\nabla_\perp = \hat{\boldsymbol{e}}_x\partial_x + \hat{\boldsymbol{e}}_y\partial_y$, ϵ_0 is the vacuum dielectric constant, $e = |e|$ is the electron charge, m_e is the electron mass and c is the speed of light. The scalar and vector potentials φ and $\boldsymbol{a}$ are normalised to $m_e c^2/e$ and $m_e c/e$, respectively. The normalised electric field is $\boldsymbol{e} = e\boldsymbol{E}/m_e c^2 = -\nabla\varphi - \partial\boldsymbol{a}/\partial ct$ and the normalised magnetic induction field is $\boldsymbol{b} = e\boldsymbol{B}/m_e c = \nabla\times\boldsymbol{a}$. The potentials φ and $\boldsymbol{a}$ are related by the Lorentz gauge equation

$$\nabla\cdot\boldsymbol{a} + \partial_{ct}\varphi = 0, \tag{2.3}$$

where $\nabla = \nabla_\perp + \hat{\boldsymbol{e}}_z\partial_z$. The electric charge and current densities ρ and $\boldsymbol{J}$ are obtained by adding all contributions of the electrons

$$\rho(\boldsymbol{r},t) = -\sum_{j=1}^{N_p} e\delta(\boldsymbol{r} - \boldsymbol{r}_j(t)), \quad \boldsymbol{J}(\boldsymbol{r},t) = -c\sum_{j=1}^{N_p} e\boldsymbol{\beta}_j\delta(\boldsymbol{r} - \boldsymbol{r}_j(t)), \tag{2.4}$$

where N_p is the number of electrons, $c\boldsymbol{\beta}_j$ is the velocity and $\boldsymbol{r}_j(t)$ the position of the jth electron. The electric charge and current densities are related through the equation of continuity

$$\partial_t\rho + \nabla\cdot\boldsymbol{J} = 0. \tag{2.5}$$

The relativistic relation between energy ε (normalised to $m_e c^2$) and canonical momentum $\boldsymbol{p} = \gamma\boldsymbol{v}/c - \boldsymbol{a}$ (normalised to $m_e c$) of an electron in the presence of a normalised electromagnetic field described by the vector potential $\boldsymbol{a}$ and scalar potential φ, is given by

$$\gamma = \varepsilon + \varphi = \sqrt{(\boldsymbol{p} + \boldsymbol{a})^2 + 1}. \tag{2.6}$$

It is convenient to use the axial position z instead of the time t as the independent variable along the particle orbits. This is allowed since $z(t)$ is an

invertible function. Then the Hamiltonian is $\mathcal{H}(\boldsymbol{r}_\perp, ct, \boldsymbol{p}_\perp, -\varepsilon | z) = -p_z$. The conjugate variables are $(\boldsymbol{r}_\perp, ct, \boldsymbol{p}_\perp, -\varepsilon)$, where $\boldsymbol{r}_\perp$ and $\boldsymbol{p}_\perp$ are the transverse components of position $\boldsymbol{r}$ and canonical momentum $\boldsymbol{p}$. The equations of motion are

$$\frac{\mathrm{d}\boldsymbol{r}_\perp}{\mathrm{d}z} = \frac{\partial \mathcal{H}}{\partial \boldsymbol{p}_\perp}, \quad \frac{\mathrm{d}ct}{\mathrm{d}z} = \frac{\partial \mathcal{H}}{\partial(-\varepsilon)}, \quad \frac{\mathrm{d}\boldsymbol{p}_\perp}{\mathrm{d}z} = -\frac{\partial \mathcal{H}}{\partial \boldsymbol{r}_\perp}, \quad \frac{\mathrm{d}(-\varepsilon)}{\mathrm{d}z} = -\frac{\partial \mathcal{H}}{\partial ct}. \tag{2.7}$$

The explicit expression of the Hamiltonian $\mathcal{H}(\boldsymbol{r}_\perp, ct, \boldsymbol{p}_\perp, -\varepsilon | z)$ is

$$\begin{aligned} \mathcal{H}(\boldsymbol{r}_\perp, ct, \boldsymbol{p}_\perp, -\varepsilon | z) &= a_z - \gamma \beta_z \\ &= a_z - \sqrt{(\varepsilon + \varphi)^2 - 1 - (\boldsymbol{p}_\perp + \boldsymbol{a}_\perp)^2}. \end{aligned} \tag{2.8}$$

The explicit differential equations describing the electron orbits (2.7) are

$$\frac{\mathrm{d}\boldsymbol{p}_\perp}{\mathrm{d}z} = -\nabla_\perp a_z + \frac{1}{\beta_z}\nabla_\perp \varphi - \sum_j \frac{1}{\gamma \beta_z}(\boldsymbol{p}_\perp + \boldsymbol{a}_\perp)_j \nabla_\perp a_{\perp j}, \tag{2.9}$$

$$\frac{\mathrm{d}\boldsymbol{r}_\perp}{\mathrm{d}z} = \frac{1}{\gamma \beta_z}(\boldsymbol{p}_\perp + \boldsymbol{a}_\perp), \tag{2.10}$$

$$\frac{\mathrm{d}\varepsilon}{\mathrm{d}z} = \partial_{ct} a_z - \frac{1}{\beta_z}\partial_{ct}\varphi + \frac{1}{\gamma \beta_z}(\boldsymbol{p}_\perp + \boldsymbol{a}_\perp) \cdot \partial_{ct}\boldsymbol{a}_\perp, \tag{2.11}$$

$$\frac{\mathrm{d}ct}{\mathrm{d}z} = \frac{1}{\gamma \beta_z}(\varepsilon + \varphi) = \frac{1}{\beta_z}. \tag{2.12}$$

The scalar and vector potentials in the equations of motion contain contributions that have different origins. The scalar potential φ is induced by the averaged charge density of the electron beam and by the perturbed charge density generated by the interaction with the high-frequency field. The scalar potential can therefore be split into a potential φ_r that is fast oscillating in space-time and a slowly-varying potential φ_s,

$$\varphi = \varphi_r + \varphi_s. \tag{2.13}$$

Inside the undulator, the electromagnetic potential consists of three contributions, the undulator field $\boldsymbol{a}_u$, the radiation field $\boldsymbol{a}_r$ and the slowly-varying self-field $\boldsymbol{a}_s$ that is associated with the averaged beam current,

$$\boldsymbol{a} = \boldsymbol{a}_u + \boldsymbol{a}_r + \boldsymbol{a}_s. \tag{2.14}$$

The magnetostatic field of the undulator is the predominant contribution to the electromagnetic field, $|\boldsymbol{a}_u| \gg |\boldsymbol{a}_r|, |\boldsymbol{a}_s|$. It is a solution of the wave equation in vacuum: $\nabla^2 \boldsymbol{a}_u = 0$. The undulator field is a periodic function of z and depends only weakly on transverse coordinates. The period of the undulator field is λ_u. The wavelength of the amplified electromagnetic wave

λ that is determined by the resonance condition (1.2) is small compared to the undulator period,

$$\lambda \ll \lambda_u \ll L_u, \tag{2.15}$$

where $L_u = N_u \lambda_u$ is the total length of the undulator.

The electron beams that are employed in free-electron lasers have a small emittance which implies that the perpendicular velocities are small. Therefore, the electrons have a small canonical momentum $\boldsymbol{p}_\perp$ when entering the undulator. The electron beam is injected close to the axis of symmetry of the undulator. We assume that this injection is adiabatic such that the perpendicular momentum is conserved. This implies $|\boldsymbol{p}_\perp| \ll |\boldsymbol{a}_u|$ so that the amplitude of the wiggle motion to leading order is

$$\boldsymbol{v}_\perp \simeq \frac{c\boldsymbol{a}_u}{\gamma}. \tag{2.16}$$

The leading order contribution to the transverse beam current is the contribution of the undulator field: $\boldsymbol{J}_\perp \simeq c\rho\boldsymbol{a}_u/\gamma$. The longitudinal beam current is to leading order $J_z \simeq \rho v_{z0}$, where v_{z0} is the longitudinal velocity of the electron beam inside the undulator that is averaged over an undulator period. The axial velocity v_{z0} is smaller than the axial velocity of the electrons before injection because of the finite transverse component.

The transverse excursions from the leading motion (2.16) are small and the important (longitudinal) equations of motion are (2.11) and (2.12). The largest contribution to the fast oscillating field $\boldsymbol{a}_r$ is the radiation field $\boldsymbol{a}_{r\perp}$. To leading order Eq. (2.11) and (2.12) are

$$\frac{\mathrm{d}\varepsilon}{\mathrm{d}z} = \partial_{ct}a_z - \frac{1}{\beta_z}\partial_{ct}\varphi + \frac{1}{\gamma\beta_z}\boldsymbol{a}_u \cdot \partial_{ct}\boldsymbol{a}_{r\perp},$$

$$\frac{\mathrm{d}ct}{\mathrm{d}z} = \left(1 - \frac{1 + a_u^2 + 2\boldsymbol{a}_u \cdot \boldsymbol{a}_{r\perp}}{\gamma^2}\right)^{-\frac{1}{2}}. \tag{2.17}$$

The ponderomotive potential corresponds to $\boldsymbol{a}_u \cdot \boldsymbol{a}_{r\perp}$. Note that only the component of the radiation field parallel to the undulator field plays a role in the ponderomotive potential. The motion of the electrons in this potential leads to bunches. The perturbed density gives a resonant contribution to the transverse beam current. This contribution to the source term in Maxwell's equation (2.1) amplifies the radiation field at the same wavenumber and frequency as the initial field $\boldsymbol{a}_{r\perp}$. This will be discussed in Section 2.3. The amplified radiation field then induces a larger ponderomotive potential that perturbs the beam density even more. Ultimately, most electrons are trapped within the potential well and the wave amplification saturates.

2.2.1 Electron Motion in the Absence of Radiation

In this Section, the unperturbed electron beam that performs a wiggle motion due to the undulator field is considered. The presence of a co-propagating electromagnetic field is disregarded. Besides the homogeneous undulator field, there are forces related with the finite size of the beam and the dependence of the undulator field on the transverse spatial dimensions x and y. Another force is the total Lorentz force associated with the beam current and charge density. It is assumed that the response of the electrons to these forces is slowly-varying and has small amplitude such that the electron energy $\gamma m_e c^2$ can be considered constant.

Slowly-Varying Self-Fields

The slowly-varying self-fields (a_s, φ_s) are induced by the slowly-varying charge and current density. The self-fields are generally very small for the electron beams employed in free-electron lasers. We consider an initially cylindrically symmetrical electron beam with radius r_b and with uniform radial density profile $n = n_0$, $(r = \sqrt{x^2 + y^2} \leq r_b)$. The undulator motion is small and can be neglected in the present calculation. The slowly-varying fields consist of the radial electric and azimuthal magnetic field, that are solutions of Maxwell's equations (2.1), (2.2). With $J_z \simeq v_{z0}\rho_0$, where $\rho_0 = -en_0$ is the unperturbed averaged charge density, these self-fields are,

$$\partial_r \varphi_s = \frac{\omega_p^2}{2c^2} r, \qquad \partial_r a_{sz} = \frac{\omega_p^2}{2c^2} \frac{v_{z0}}{c} r, \qquad (r \leq r_b), \tag{2.18}$$

where v_{z0} is the average longitudinal electron velocity (2.22) inside the undulator and the plasma frequency ω_p is defined as

$$\omega_p^2 = \frac{e^2 n_0}{\varepsilon_0 m_e}. \tag{2.19}$$

Outside the electron beam $(r > r_b)$, the fields decay as $1/r$. At relativistic energies, the forces due to the radial electric and azimuthal magnetic field almost cancel, and yield a net radially outward Lorentz force on the electron beam. The total force is

$$F_{\text{self}} = m_e c^2 \frac{\omega_p^2}{2c^2} r \left(1 - \frac{v_{z0}^2}{c^2} \right), \qquad (r \leq r_b). \tag{2.20}$$

This force is very small for the electron beams used for free-electron lasers. The wiggle motion induces small perturbations in the density, that lead to small corrections to (2.20).

In the cases of interest, the transverse forces due to the transverse dependence of the undulator field are larger than the self forces (2.20). The corrections to the slowly-varying self-fields due to the perturbed beam density can be neglected. These self-fields are constant in time and do not contribute to the ponderomotive potential.

Electron Motion in a Single Undulator

The undulator field is a solution of Maxwell's equation (2.1) in vacuum $\nabla^2 \boldsymbol{a}_u = 0$, with boundary conditions that the field has periodicity in z with λ_u and has even symmetry in x and y. We assume that the undulator has a large number of periods, $N_u \gg 1$ and that end effects may be neglected. The undulator field is written as:

$$\boldsymbol{a}_u(x, y, z) = \hat{\boldsymbol{e}}_x a_u \cos(k_u z) \cosh(k_x x) \cosh(k_y y) \tag{2.21}$$

where $a_u = eB_u/(m_e c k_u)$, B_u is the on-axis undulator amplitude and $k_u = 2\pi/\lambda_u = \sqrt{k_x^2 + k_y^2}$ is the undulator wavenumber. On axis, the magnetic field of the undulator is directed purely in the y-direction. The wiggle motion is in the x-z plane. According to Eq. (2.16) the transverse velocity is $v_x = c a_u \cos(k_u z)/\gamma$. This modulates the longitudinal velocity,

$$v_z = v_{z0} \sqrt{1 - \frac{c^2 a_u^2 \cos(2 k_u z)}{2 v_{z0}^2 \gamma^2}}, \qquad v_{z0} \equiv c \sqrt{1 - \frac{1 + \frac{1}{2} a_u^2}{\gamma^2}}. \tag{2.22}$$

The planar undulator field near the axis ($k_x x, k_y y \ll 1$) is

$$\boldsymbol{a}_u(z) = a_u \hat{\boldsymbol{e}}_x \cos(k_u z) \left(1 + \frac{k_x^2 x^2}{2} + \frac{k_y^2 y^2}{2} \right). \tag{2.23}$$

Off-axis, the undulator field has a component directed in the z-direction that induces a transverse force on the electron beam, which leads to focussing in both transverse directions [24]. In the inhomogeneous undulator field (2.23). small deviations from the on-axis wiggle motion lead to betatron oscillations.

The orbits of the electrons in the combined fields of the undulator field (2.23) and the self-fields (2.18), near the axis, are determined by the equation of motion for the momentum (2.9). The right-hand side (RHS) of this equation is approximated with the use of the leading order wiggle motion Eq. (2.16). It follows that

$$\frac{dp_{x_i}}{dz} = -\frac{\partial a_{sz}}{\partial x_i} + \frac{1}{\beta_z} \frac{\partial \varphi_s}{\partial x_i} - \frac{k_{x_i}^2 a_u^2 \cos^2(k_u z)}{\gamma \beta_z} x_i, \qquad x_i = x, y. \tag{2.24}$$

We take that $k_x^2 = k_y^2 = k_u^2/2$, so that in this linear approximation a circular electron beam will remain so in time. Then the slowly-varying self-fields a_{sz} and φ_s are described by equations (2.18). The orbit equations are expanded around the leading order solution for the on-axis motion (2.16), $x = ca_u \sin(k_u z)/(k_u \gamma v_{z0}) + \delta x$, $y = \delta y$. The displacements from the axis of the electron beam δx and δy are so small that $|k_u \delta x|, |k_u \delta y| \ll 1$. To lowest order, δx and δy satisfy

$$\frac{d^2 \delta x_i}{dz^2} = -\frac{k_u^2 a_u^2}{4\beta_z^2 \gamma^2} \delta x_i + \frac{\omega_p^2}{2c^2 \beta_z^2 \gamma^3}(1 + \frac{1}{2}a_u^2)\delta x_i, \qquad \delta x_i = \delta x, \delta y. \quad (2.25)$$

The equations are averaged over an undulator period and the approximation $1 - \beta_z^2 = (1 + a_u^2/2)/\gamma^2$ has been made. The first term on the right-hand side of equation (2.25) originates from the inhomogeneity of the undulator field. This is an oscillatory contribution to the electron motion. The second term originates from the defocussing force of the slowly-varying self-fields. The ratio of these terms is M^2,

$$M^2 = \frac{a_u^2 \gamma k_u^2 c^2}{2\omega_p^2(1 + \frac{1}{2}a_u^2)}. \quad (2.26)$$

The ratio M^2 is dependent on the beam density through the plasma frequency. Note that the terms on the right-hand side of equation (2.25) have opposite signs. Therefore, the forces due to the self-fields decrease the effect of betatron oscillations. In the case of $M^2 \gg 1$ the forces due to the slowly-varying self-fields can be neglected. Such a beam is called an emittance dominated electron beam. The periodic solutions are the betatron oscillations and the corresponding betatron wavenumber is $k_{\beta 0} = k_u a_u/(2\gamma\beta_z)$. The amplitude of the betatron oscillations depends on the initial velocity and displacement from the axis of symmetry. In the combined fields of the undulator and the slowly-varying self-fields, the (modified) betatron wavenumber is $k_\beta = k_{\beta 0}(1 - 1/M^2)^{1/2}$. Near the Brillouin density limit, $M^2 = 1$, the forces of the self-fields are equal to the forces due to the inhomogeneous undulator field. Such a beam is called a space-charge dominated electron beam. It is clear that electron beam equilibria do not exist for densities above the Brillouin density limit (or $M^2 < 1$), because then the defocussing space-charge force is too large.

The FEM design has an electron beam current of $I = 12 \, \text{A}$ with a circular cross-section with radius of $r_b = 1.3 \, \text{mm}$, as is given in Table 3.1. With these parameters, M^2 is of order 10 and the force due to the inhomogeneity of the undulator is the dominant one. The ratio M^2 becomes of the order of one when $r_b = 0.35 \, \text{mm}$.
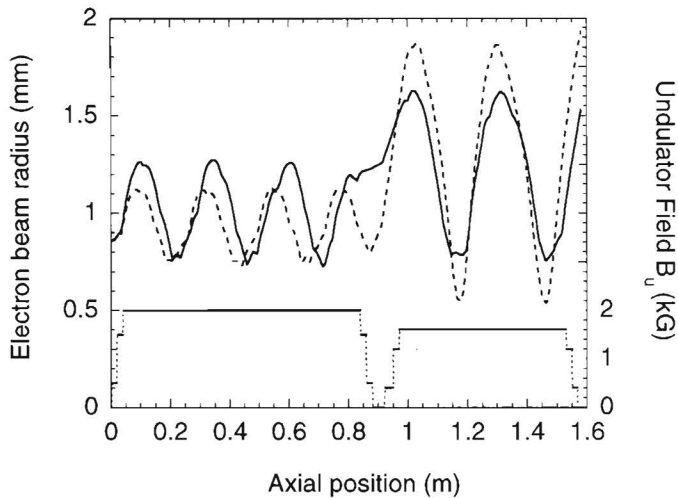
Figure 2.1: *The radius of the electron beam while interacting with the microwave field is plotted. The electron beam interacts with the step-tapered undulator, of which the field amplitude is plotted. The electrons experience radial forces due to the inhomogeneous undulator field and the self-fields. The radius of the electron beam is depicted by the solid line. The dashed line is the radius of the electron beam when the self-fields are disregarded.*

The effect of the inhomogeneous undulator field and the slowly-varying self-fields on the electron beam radius is depicted in Fig. 2.1 (solid line). There the radius of the electron beam with respect to the wiggling centre of the beam is plotted. The radius is calculated in the presence of radiation with the numerical code MFF that is described in Chapter 3. The undulator is the step-tapered undulator (see Chapter 3). The period of the betatron oscillation is k_β. The second section, that has lower field amplitude a_u, has longer betatron wavelength than the first section. The dashed line is the radius in the case without the self-fields.

2.3   Stimulated Emission

In Chapter 1, a global explanation of the free-electron laser mechanism has been given. In the present Section we will explain the physics in more detail and in particular we will analyse the influence of density effects with the use of an one-dimensional approach.

The electron beam can support two distinct types of fast waves. Let the

electric field $\boldsymbol{E}$ be a monochromatic plane wave, $\exp[\mathrm{i}(\boldsymbol{k} \cdot \boldsymbol{r} - \omega t)]$, that is a solution of Maxwell's equations and assume that the field is weak enough to neglect nonlinear effects. The two types of waves are classified according to the direction of the field $\boldsymbol{E}$ with respect to the direction of the propagation vector $\boldsymbol{k}$.

Electromagnetic (EM) waves are characterised by $\boldsymbol{E} \cdot \boldsymbol{k} = 0$. Hence, according to Poisson, these waves do not perturb the density in the longitudinal direction. The dispersion relation is

$$\omega_r = \sqrt{c^2 k_z^2 + c^2 k_c^2 + F \frac{\omega_p^2}{\gamma}}, \tag{2.27}$$

where k_c is the cutoff wavenumber of the waveguide and F is the ratio of the cross-sectional areas of the electron beam and the radiation field. The last term under the square root is small in standard free-electron lasers and also in the cases considered in this thesis. According to the dispersion relation (2.27), the phase velocity of these waves is larger than c and consequently, these waves cannot couple directly to the electron beam.

Longitudinal or electrostatic (ES) waves are characterised by the fact that $\boldsymbol{E}$ is parallel to $\boldsymbol{k}$. The dispersion relation for these space-charge waves is

$$\omega_{\pm} = (k_z + k_u)v_z \pm \frac{\omega_p}{\gamma_z \sqrt{\gamma}}, \tag{2.28}$$

where $\gamma_z = 1/\sqrt{1 - \beta_z^2}$. In the limit $\omega_p \to 0$, the two electron beam space-charge waves coincide. Two waves can be distinguished; the positive-energy, fast space-charge wave ω_+, with phase velocity that is larger than the one of the beat wave $v_{pon} = \omega/(k_z + k_u)$, and the negative-energy, slow space-charge wave ω_-, with phase velocity that is smaller than v_{pon}. The first is stable and the other is unstable.

Their response to small disturbances is quite different. This can be shown by investigating the energy density of electrostatic waves, that is proportional to $\omega \partial_\omega \varepsilon_r$ [47]. The dielectric constant is $\varepsilon_r = 1 - \omega_p^2/(\gamma_z^2 \gamma(\omega - (k_z + k_u)v_z)^2)$ and from $\varepsilon_r \simeq 0$ the space-charge waves (2.28) are obtained. The space-charge wave with the negative sign ω_- has $\omega \partial_\omega \varepsilon_r < 0$, therefore it is a negative-energy wave. As the space-charge wave feeds energy to the radiation field its energy decreases, leading to simultaneous growth of the beam space-charge wave and the radiation field.

The interaction in a free-electron laser occurs at the intersections of the electromagnetic wave (2.27) and the unstable, slow space-charge wave (2.28) in the dispersion diagram. The intersections of the two dispersion relations determine the frequency and wavenumber (ω, k_z) of the radiation field. The

ponderomotive potential is determined by the undulator field and the radiation field $\boldsymbol{a}_u \cdot \boldsymbol{a}_{r\perp}$, as in Eq. (2.17). The motion of the electrons in this potential leads to longitudinal bunching. This leads to an amplification the radiation field.

The fast longitudinal charge and current oscillations due to the bunching process also give another contribution to the electromagnetic potentials, a longitudinal electric field. The one-dimensional, linear model of the free-electron laser [33, 48] is a nice tool to reveal the response of the charge and current density on the free-electron laser interaction.

We start with the radiation field $\boldsymbol{a}_{r\perp}$ that has the same polarisation as the undulator field $\boldsymbol{a}_u$ so that a ponderomotive potential is generated. The radiation field $|\boldsymbol{a}_{r\perp}| \ll |\boldsymbol{a}_u|$ is guided in a waveguide with cutoff wavenumber k_c and satisfies Maxwell's equation (2.1),

$$(\partial_z^2 - \partial_{ct}^2 - k_c^2)\boldsymbol{a}_{r\perp} = -\frac{e}{\epsilon_0 m_e c^3}F\boldsymbol{J}_\perp, \tag{2.29}$$

where $\boldsymbol{J}_\perp$ is the induced transverse current density and $F = \sigma_b/\sigma_r$ is the filling factor associated with the radiation field that is defined as the ratio of the cross-sectional areas of the electron beam σ_b and radiation field σ_r. In the present case σ_r is approximately equal to the cross-sectional area of the waveguide. Assume again that the transverse canonical momentum $\boldsymbol{p}_\perp$ remains small. Then the transverse velocity is induced by the undulator field and the radiation field. The transverse current density is given by

$$\boldsymbol{J}_\perp(z, t) = -en\boldsymbol{v}_\perp \simeq -\frac{ce}{\gamma}(n_0 + \delta n)(\boldsymbol{a}_u + \boldsymbol{a}_{r\perp}), \tag{2.30}$$

where n_0 is the averaged beam density and δn is the perturbed beam density. The perturbed beam density is generated by the electron motion in the ponderomotive potential well. Only terms that have the same phase as the high-frequency field, $(n_0\boldsymbol{a}_{r\perp} + \delta n\boldsymbol{a}_u)$, play a role in the coherent amplification. The small term $\delta n\boldsymbol{a}_r$ leads to a low level of higher harmonics. Substituting the transverse current density in the wave equation leads to

$$(\partial_z^2 - \partial_{ct}^2 - k_c^2 - F\frac{\omega_p^2}{\gamma c^2})\boldsymbol{a}_{r\perp} = F\frac{\omega_p^2}{\gamma c^2}\frac{\delta n}{n_0}\boldsymbol{a}_u. \tag{2.31}$$

Since δn is perturbed at the beat wave frequency and wavenumber, $\delta n\boldsymbol{a}_u$ is a non-vanishing contribution to the transverse current density that has the same wavelength and wavenumber as the driving field $\boldsymbol{a}_{r\perp}$. Therefore, the radiation field is driven by the undulator field $\boldsymbol{a}_u$ and the perturbed beam density δn.

The axial electric field $e_z = -\partial_z\varphi - \partial_{ct}a_z$ is associated with the bunching process. It is a solution of Poisson's equation, that is equivalent to Eq. (2.2). This field is confined within the electron beam and perpendicular dependencies play no role, therefore,

$$\partial_z e_z = \frac{\omega_p^2}{c^2}\frac{\delta n}{n_0}. \tag{2.32}$$

The perturbed density δn can be found from the continuity equation (2.5), $e\partial_t\delta n = \partial_z\delta J_z$, where the longitudinal current density is written as $J_{z0} + \delta J_z$. The perturbed axial beam current density is $\delta J_z(z,t) = -e(n_0\delta v_z + v_{z0}\delta n)$, where v_{z0} is the unperturbed and δv_z is the perturbed axial velocity. This leads to the following expression for the perturbed beam density

$$\frac{d\delta n}{dz} = -\frac{n_0}{v_{z0}}\partial_z\delta v_z. \tag{2.33}$$

We assume that the spread in transverse momentum and the spread in energy are small. In that case, the equations of motion in the fluid model are formally identical to those in the particle model. The perturbed axial velocity δv_z is found from $dp_z/dz = -\partial_z\mathcal{H}$. Keeping terms to first order in the radiation field and using Eq. (2.16), we find,

$$\frac{d\delta v_z}{dz} = -\frac{c^2}{\gamma v_{z0}}(\partial_z\phi + \partial_{ct}a_z) - \frac{v_{z0}}{\gamma}\frac{d\delta\gamma}{dz} - \frac{c^2\boldsymbol{a}_\perp}{\gamma^2 v_{z0}}\partial_z\boldsymbol{a}_\perp. \tag{2.34}$$

Combining Eq. (2.33) and Eq. (2.34) and using Eq. (2.17) for $d\delta\gamma/dz$ leads to an expression for the evolution of the perturbed charge density,

$$\frac{d^2\delta n}{dz^2} + \frac{\omega_p^2}{v_{z0}^2\gamma\gamma_z^2}\delta n = -\frac{n_0 c^2}{v_{z0}^2\gamma}\frac{\partial}{\partial z}\left(\frac{\partial}{\partial z} + \frac{v_{z0}}{c^2}\frac{\partial}{\partial t}\right)\Phi_{\text{pon}}(z,t), \tag{2.35}$$

where $\Phi_{\text{pon}}(z,t)$ is called the (effective) ponderomotive potential, that is given by

$$\Phi_{\text{pon}}(z,t) = -\frac{1}{\gamma}\boldsymbol{a}_u \cdot \boldsymbol{a}_{r\perp}. \tag{2.36}$$

The perturbed density and the undulator induced velocity lead to a resonant contribution to the transverse beam current. This contribution to the source term in Maxwell's equation amplifies the radiation field at the same frequency as the radiation field $\boldsymbol{a}_{r\perp}$. The planar undulator field is specified by Eq. (2.23). For simplicity we take that the radiation field is represented by a single frequency component (ω, k_z),

$$\boldsymbol{a}_{r\perp}(z,t) = \hat{\boldsymbol{e}}_x a_r e^{i(k_z z - \omega t)} + \text{c.c.}, \tag{2.37}$$

Only the resonant contribution to the ponderomotive potential is relevant
and the explicit expression is

$$\Phi_{\text{pon}} \simeq -\frac{1}{2\gamma} a_u a_r e^{i[(k_z + k_u)z - \omega t]} + \text{c.c.} \tag{2.38}$$

The neglected contribution corresponds to a phase velocity that is larger
than c. The perturbed density modulation is driven by the oscillatory mo-
tion of the electrons in the ponderomotive potential (2.38) and has a similar
dependence in the time-asymptotic limit,

$$\delta n(z, t) = \delta \tilde{n} e^{i[(k_z + k_u)z - \omega t]} + \text{c.c.} \tag{2.39}$$

After substitution of the ponderomotive potential Φ_{pon} (2.38) in Eq. (2.35),
this equation can be solved for δn. When these explicit expressions are
substituted in the wave equation (2.31), one obtains a dispersion relation,

$$\left(\omega^2 - c^2 k_z^2 - c^2 k_c^2 - F \frac{\omega_p^2}{\gamma} \right) \left\{ \left[\omega - v_{z0}(k_z + k_u) \right]^2 - \frac{\omega_p^2}{\gamma_z^2 \gamma} \right\} =$$

$$\frac{F \omega_p^2 c^2 a_u^2}{2\gamma^3} (k_z + k_u) \left(k_z + k_u - \frac{v_{z0}\omega}{c^2} \right). \tag{2.40}$$

The coupling constant in the RHS of the dispersion relation (2.40) is small
compared to ω^4 and provides the coupling between the electromagnetic and
the space-charge waves. The coupling constant is only nonzero within the
undulator. The first term (in parentheses) in the dispersion relation repre-
sents two uncoupled electromagnetic waves in an underdense electron beam,
that are guided in a waveguide with cutoff wavenumber k_c. The second term
(in braces) in the dispersion relation (2.40) represents the two uncoupled
electron beam space-charge waves. The coupling constant of the waves plays
only a role in the dispersion relation close to the intersection of the uncoupled
waves, as is indicated in Fig. 2.2. The intersection of the electromagnetic ω_r
and the negative-energy space-charge ω_- waves at high frequency is the rel-
evant solution. This intersection is indicated by the star in Fig. 2.2. Solving
$\omega_r = \omega_-$, the corresponding frequency ω is

$$\omega = \frac{c\beta_z k_u}{1 - \beta_z^2} \left[1 - \frac{\omega_p}{c\beta_z k_u \gamma_z \sqrt{\gamma}} + \right.$$

$$\left. \beta_z \left(1 - \frac{2\omega_p}{c\beta_z k_u \gamma_z \sqrt{\gamma}} - \frac{k_c^2}{\beta_z^2 k_u^2 \gamma_z^2} + \frac{\omega_p^2}{c^2 \beta_z^2 k_u^2 \gamma \gamma_z^2}(1 - F) \right)^{\frac{1}{2}} \right]. \tag{2.41}$$

The Compton regime is a single-particle scattering regime, where the pon-
deromotive potential dominates the space-charge potential. In this regime,

the linear terms in ω_p in Eq. (2.41) are negligibly small. In the collective regime these terms are large and modify the operating frequency with respect to the Compton regime. Since the operating frequency is changed, this regime is called the Raman regime, in analogy with atomic Raman scattering [49]. In this regime, the radiation field is not amplified by single electrons, but by the collective behaviour. In the case the cross sectional areas of the electron and radiation beam coincide, for example, when the optical guiding of the radiation field by the electron beam is very strong, then $F = 1$ and the last term in Eq. (2.41) vanishes. For FEM parameters, this term is the smallest. The factor F is not important for the determination of k_z and ω, since it is always a small term in the dispersion relation for the electromagnetic waves. However, it is an important factor in the coupling constant and therefore equally important for the imaginary part of k_z, that corresponds to growth. The cutoff wavenumber of the waveguide is responsible for the term $k_c^2/(\beta_z^2 k_u^2 \gamma_z^2)$, which, for FEM parameters, is the largest contribution besides 1 in the root.

Although we are interested in the intersection marked by the star in Fig. 2.2, there is another intersection of the waves. This intersection of the waves at low frequency can lead to a forward propagating $(\omega/k_z > 0)$ or a backward propagating $(\omega/k_z < 0)$ wave. The frequency of this wave is quite different from the actual operating frequency. The forward propagating wave initially interacts with an unperturbed electron beam. The wave corresponding to the solution indicated with the star has larger growth rate and will dominate the interaction. The boundary condition for the backward propagating wave is quite different, because in the presence of the forward propagating radiation indicated with the star, the electrons are bunched at the exit of the undulator. Output of the backward propagating wave can be generated even in the absence of any input. This is referred to as backward-wave instability. Since this wave may modify the electron beam at the entrance, it is a parasite that must be carefully avoided.

Both the intersections of the negative-energy electron beam line and the electromagnetic wave have positive phase velocities $(\omega/k_z > 0)$ when

$$\sqrt{c^2 k_c^2 + \frac{F\omega_p}{\gamma}} > v_{z0} k_u - \frac{\omega_p}{\gamma_z \sqrt{\gamma}}. \qquad (2.42)$$

For a rectangular waveguide, with height a, the fundamental waveguide mode has cutoff wavenumber $k_c = \pi/a$, which means that the condition imposes an upper limit on the waveguide size $a < \beta_z k_u/\pi$. In the case of intersecting electromagnetic and electron beam lines at positive phase velocities, the dispersion relation is approximated to

$$(k_z - \kappa_{em})(k_z - \kappa_-)(k_z - \kappa_+) = -\alpha^2, \qquad (2.43)$$

where the electromagnetic wavenumber κ_{em} and the wavenumbers of the positive and negative-energy space-charge wave $\kappa_\pm$ are given by

$$\kappa_{em} = \sqrt{\frac{\omega^2}{c^2} - k_c^2 - \frac{F\omega_p^2}{\gamma c^2}}, \qquad \kappa_\pm = \frac{\omega}{v_{z0}} - k_u \mp \frac{\omega_p}{v_{z0}\gamma_z\sqrt{\gamma}}. \qquad (2.44)$$

The coupling coefficient α^2 is

$$\alpha^2 = \frac{F\omega_p^2 a_u^2}{4\kappa_{em}v_{z0}^2\gamma^3}(k_z + k_u)\left(k_z + k_u - \frac{v_{z0}\omega}{c^2}\right) \simeq \frac{F\omega_p^2 k_u a_u^2}{2v_{z0}^2\gamma^3}. \qquad (2.45)$$

which is approximated with the use of $\omega \simeq ck_z \simeq v_{z0}(k_z + k_u) \gg ck_u$, such that $(k_z + k_u)(k_z + k_u - v_{z0}\omega/c^2) \simeq 2k_u k_z$ and $\kappa_{em} \simeq k_z$.

Fig. 2.3 shows the stable and unstable solutions of the dispersion relation (2.43) in the neighbourhood of the star in Fig. 2.2. The coupling between the electromagnetic wave and the negative-energy electron beam space-charge wave leads to a solution with imaginary part, of which the negative imaginary part for k_z corresponds to spatial (exponential) growth of the radiation field. In terms of δk, where $\delta k = k_z - \kappa_-$, the dispersion relation is

$$(\delta k - \Delta)(\delta k)\left(\delta k + \frac{2\omega_p}{v_{z0}\gamma_z\sqrt{\gamma}}\right) = -\alpha^2, \qquad (2.46)$$

where $\Delta = \kappa_{em} - \kappa_-$ is the mismatch of the wavenumbers; δk is in general complex and $|\delta k| \ll k_z$.

2.3.1 Free-Electron Laser Operating Regimes

In order to distinguish the different operating regimes, it is convenient to normalise δk in the dispersion relation (2.46) to $2\omega_p/(\gamma_z\sqrt{\gamma}v_{z0})$.

In the high-gain Compton regime, the effect of the ponderomotive potential dominates that of the space-charge potential. The corresponding condition is $\alpha^{2/3} \gg 2\omega_p/(\gamma_z\sqrt{\gamma}v_{z0})$, i.e.

$$\frac{\omega_p}{v_{z0}k_u\gamma_z\sqrt{\gamma}} \ll \frac{Fa_u^2\gamma_z^2}{16\gamma^2}. \qquad (2.47)$$

A high energy, low density electron beam satisfies this relation. The wiggler amplitude must be strong, therefore this regime is also called the strong-pump regime. In this regime, the dispersion relation (2.46) may be written as $(\delta k - \Delta)(\delta k)^2 = -\alpha^2$. Maximum growth occurs at exact frequency matching $(\Delta = 0)$. Then the root of the dispersion relation with negative imaginary part is

$$\delta k = \frac{1}{2}\left(1 - i\sqrt{3}\right)\alpha^{2/3}. \qquad (2.48)$$
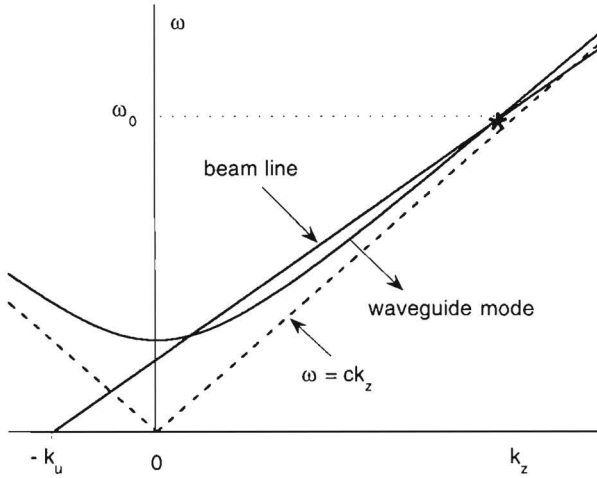
Figure 2.2: *Intersection of the electron beam line* $\omega = (k_z + k_u)v_{z0}$ *and the guided electromagnetic wave* $\omega = (c^2k_z^2 + c^2k_c^2)^{1/2}$ *in the Compton regime. The star marks the intersection where maximum growth occurs.*
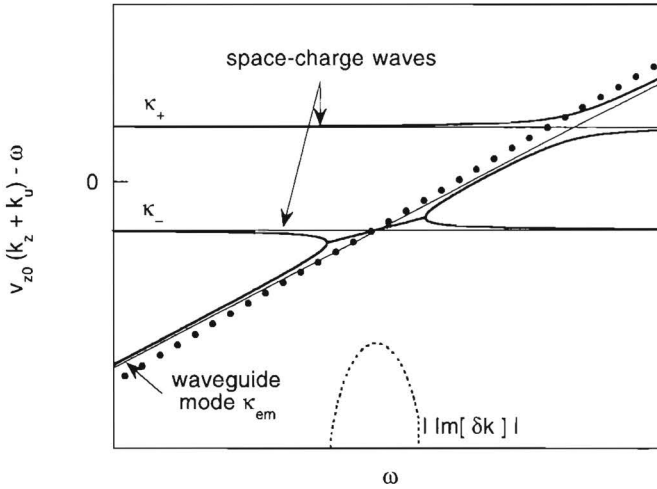
Figure 2.3: *Stable and unstable solutions of the FEL dispersion relation (2.43). The unstable coupling occurs between the electromagnetic wave and the negative-energy electron beam space-charge wave. The dotted line indicates the (enlarged) imaginary part of the wavenumber, corresponding to spatial growth, that is zero outside the unstable region. The dots indicate the approximated sets* (ω_l, k_{zl}) *(see Section 2.4) that have the same phase velocities.*

The negative imaginary root indicates spatial growth $-\mathrm{Im}[\delta k]$.

In the Raman regime, the space-charge potential dominates the pondero-motive potential, $\alpha^{2/3} \ll 2\omega_p/(\gamma_z \sqrt{\bar\gamma} v_{z0})$, i.e.,

$$\frac{\omega_p}{ck_u\gamma_z\sqrt{\bar\gamma}} \gg \frac{Fa_u^2\gamma_z^2}{16\gamma^2}.\tag{2.49}$$

This regime is also called the weak-pump regime. In this regime, the dispersion relation (2.46) reduces to a quadratic equation in δk, $(\delta k - \Delta)(\delta k) = -\gamma_z\sqrt{\bar\gamma}v_{z0}\alpha^2/(2\omega_p)$. The solution δk at maximum negative imaginary part $(\Delta = 0)$ is

$$\delta k = -\frac{\mathrm{i}}{2}\sqrt{2\alpha^2\frac{\sqrt{\bar\gamma}\gamma_z v_{z0}}{\omega_p}}.\tag{2.50}$$

There are generally two extra criteria [46] that determine whether the free-electron laser operates in this regime. The normalised Raman frequency shift must exceed the line-width due to finite undulator length,

$$\frac{\omega_p}{\gamma_z\sqrt{\bar\gamma}ck_u\beta_z} > \frac{\lambda_u}{L_u},\tag{2.51}$$

where $L_u = N_u\lambda_u$ is the length of the undulator. The physical interpretation of this criterium is that the undulator is long enough for several plasma oscillations to occur during the course of the interaction. The other criterium is that Landau damping of the space-charge waves due to thermal spread of the electron beam must be small. The space-charge wave is strongly damped if its wavelength is less or of the order of the Debye length. In the electron reference frame [17] the Debye length is $\lambda_D = 2\pi v_{th}/(\omega_p/(\gamma_z\sqrt{\bar\gamma}))$. The Debye length can be understood as the longitudinal distance electrons move with thermal speed v_{th}, given by the energy spread in the beam, within the typical time of the plasma oscillation ω_p^{-1}.

The regime in between the Compton and Raman regime is of interest in this thesis. In this intermediate regime, there is competition between the ponderomotive and space-charge potential. The resulting effect is a reduction of the gain of the radiation field. In this intermediate regime, maximum growth corresponds to a small, finite detuning. This is shown in Fig. 2.4, where the detuning normalised to $b_p = 2\omega_p/(v_{z0}\gamma_z\sqrt{\bar\gamma})$ that corresponds to maximum growth rate is plotted as a function of the coupling parameter normalised to b_p^3. The function goes linearly to zero for $\alpha^2/b_p^3 \to 0$ and grows asymptotically to $\frac{1}{2}$ for large values of α^2/b_p^3. Note that the value of α^2/b_p^3 determines the operating regimes. It follows that in the high-gain Compton regime $(\alpha^2/b_p^3 \to \infty)$, maximum growth corresponds to zero detuning $\Delta \simeq$
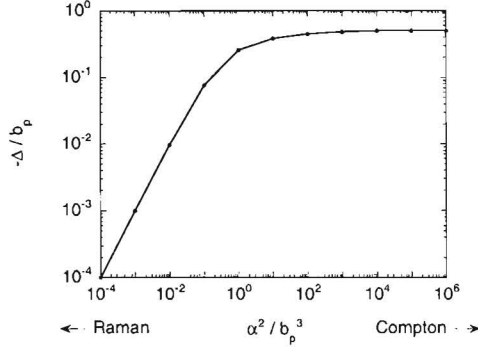
Figure 2.4: *The detuning* $-\Delta/b_p$ *at maximum growth rate is plotted as a function of the coupling parameter* α^2/b_p^3. *The Raman regime is determined by* $\alpha^2/b_p^3 \to 0$ *and the high-gain Compton regime by* $\alpha^2/b_p^3 \to \infty$.

$-b_p/2 = 0$. In the Raman regime ($\alpha^2/b_p^3 \to 0$), maximum growth occurs at zero detuning $\Delta \to 0$. In the intermediate regime, the value of α^2/b_p^3 is in the order of one. Here, the detuning corresponding to maximum growth rate can be found from Fig. 2.4

2.3.2 Evolution in Phase Space and Extraction Efficiency

In order to get insight in the interaction between the beam electrons and the ponderomotive wave, the Eq. (2.17) is simplified to a pendulum equation. The previous definition for the undulator field (2.23) is applied and for simplicity the electromagnetic field in the single-frequency approximation (2.37) is taken. We assume that all transverse effects can be disregarded and that the interaction is well described by Eq. (2.17). We linearise this equation and assume that the self-fields can be neglected and $1/\gamma^2$ is small. The resulting equation is averaged over an undulator period,

$$\frac{d\gamma}{dz} = -\frac{\beta_{ph}k_z}{\beta_z\gamma}a_u a_r \sin\psi, \quad \frac{d\psi}{dz} = k_u - \frac{\beta_{ph}k_z}{2\gamma^2}(1 + \frac{a_u^2}{2} + a_u a_r \cos\psi) \quad (2.52)$$

where $\psi = (k_z + k_u)z - \omega t$ is the phase in the ponderomotive potential and $d\psi/dz$ is a measure of the electron streaming velocity that describes the electron velocity as a function of the phase of the ponderomotive wave. After differentiation a pendulum equation remains that can once be integrated,

$$\frac{1}{2}\left(\frac{d\psi}{dz}\right)^2 - K^2 \cos\psi = E, \quad (2.53)$$

where E is the total energy of the system, the 'oscillator' energy and the pendulum constant is $K^2 = \beta_{ph}^2 k_z^2 a_u a_r / (\beta_z \gamma^2 \gamma_z^2)$. The electron trajectories through the wiggler, therefore, are expressed as

$$\frac{\mathrm{d}\psi}{\mathrm{d}z} = \pm\sqrt{2E + 2K^2 \cos(\psi)}. \tag{2.54}$$

The separatrix (the energy E is equal to the potential K^2) describes the transition between two classes of electron trajectories; trapped and untrapped orbits. The separatrix is given by a pair of curves ($\mathrm{d}\psi/\mathrm{d}z = 0$) in the phase space ($\mathrm{d}\psi/\mathrm{d}z, \psi$). Free-streaming, untrapped orbits are characterised by $E > |K^2|$ and are outside the separatrix in phase space. The free-streaming electrons pass over many crests of the ponderomotive wave. Trapped orbits are those for which $E < |K^2|$ and are within the bounds of the separatrix. The evolution in phase space ($\mathrm{d}\psi/\mathrm{d}z, \psi$) is indicated in Fig. 2.5. Plotted are the positions of the electrons in phase space that are the solutions of the set of equations (2.9)–(2.12) as are implemented in the numerical code and are explicitly given in Section 2.4 and 2.6. The radiation field is taken in the single-frequency limit, and the exact equations for the electrons are solved.

The saturation mechanism is the particle trapping in the combined ponderomotive and space-charge potentials. The height of the separatrix (K^2) increases as the radiation field $a_{r\perp}$ grows and more electrons become trapped within the separatrix. Approximately all electrons are trapped when the height of the separatrix reaches the initial phase space positions of the electrons. The trapped electrons perform a rotation. The growth of the wave continues until the electrons reach the bottom of the stable area. At that point the electrons start to absorb energy from the wave. Saturation is reached when the energy absorption of the leading electrons is balanced by the emission of the trailing electrons in the rotation.

With the foregoing description of the FEM interaction, we can make an ad hoc estimate of the extraction efficiency at saturation. The extraction efficiency is defined as the percentage of energy the electrons transfer to the microwave field with respect to their initial energy. The electrons initially have a velocity v_{z0} and the trapping potential propagates with phase velocity $v_{ph} = \omega/(k_u + \mathrm{Re}[k])$, where the real part of the wavenumber depends on the operating regime, as we have seen in the previous Section. At saturation, the electrons have lost on average an amount of energy that corresponds to twice the difference in axial velocity $\Delta v \simeq v_{z0} - v_{ph}$,

$$\Delta E_{\mathrm{kin}} \simeq 2\gamma_z^3 m_e v_{z0} \Delta v, \tag{2.55}$$

where $\gamma_z^2 = 1/(1 - v_{z0}^2/c^2)$. The extraction efficiency, that is defined as the ratio of the energy lost by the electrons to the initial electron kinetic energy
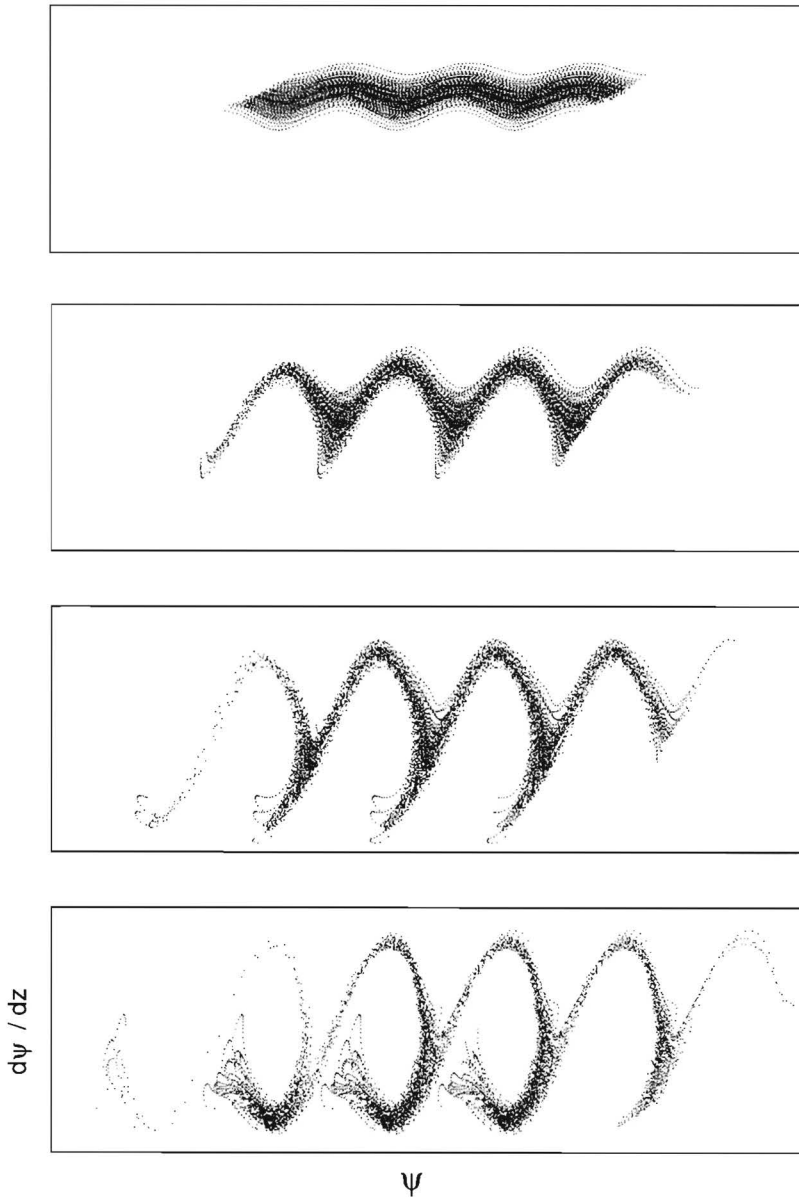
Figure 2.5: *The longitudinal phase space* $(\mathrm{d}\psi/\mathrm{d}z, \psi)$ *of the beam electrons for different axial positions* z *in the undulator are plotted. The positions are the solutions of the set of equations (2.9) -(2.12) as are implemented in the numerical code and are explicitly given in Section 2.4 and 2.6. The radiation field (here taken in the single-frequency limit) is strongly amplified during the interaction.*

is

$$\eta \simeq \frac{2\gamma_z^3 v_{z0}\Delta v}{(\gamma_z - 1)c^2}. \tag{2.56}$$

The velocity difference can be determined as follows. In the expression for the phase velocity, the real part of the wavenumber occurs. The wavenumber is given by Eq. (2.44). In terms of δk the wavenumber is

$$\text{Re}[k] = \frac{\omega}{v_{z0}} - k_u + \frac{\omega_p}{v_{z0}\gamma_z\sqrt{\gamma}} + \text{Re}[\delta k]. \tag{2.57}$$

This yields an expression for v_{ph} and thus for Δv. It follows that, with the approximated value of ω, determined by Eq. (2.41), the efficiency can be written as

$$\eta \simeq \frac{2v_{z0}^2}{(1 + v_{z0}/c)c^2 k_u} \frac{\gamma_z}{(\gamma_z - 1)} \left(\frac{\omega_p}{v_{z0}\gamma_z\sqrt{\gamma}} + \text{Re}[\delta k] \right). \tag{2.58}$$

In the high-gain Compton and Raman regime, δk is given by the solutions (2.48) and (2.50), respectively. The phase velocity at the frequency of zero mismatch $\Delta = 0$ results in a saturation efficiency in the high-gain Compton regime of

$$\eta_C \simeq \frac{v_{z0}^2}{c^2(1 + v_{z0}/c)} \frac{\gamma_z}{(\gamma_z - 1)} \left(\frac{F\omega_p^2 a_u^2}{2v_{z0}^2 k_u^2 \gamma^3} \right)^{1/3} \tag{2.59}$$

and in the collective Raman regime of

$$\eta_R \simeq \frac{2}{(1 + v_{z0}/c)} \frac{\gamma_z}{(\gamma_z - 1)} \frac{v_{z0}\omega_p}{c^2 k_u \gamma_z\sqrt{\gamma}}. \tag{2.60}$$

Note that in the high-gain Compton regime, the real part of δk is a function of the mismatch parameter Δ. The real part of δk grows to a maximum value $\text{Re}[\delta k] = (2\alpha^2)^{1/3}$ when $\Delta = \frac{3}{2}(2\alpha^2)^{1/3}$. For this value of the detuning the growth rate vanishes. The maximum value of $\text{Re}[\delta k]$ corresponds to the maximum extraction efficiency at saturation, see Eq. (2.58).

2.4   The Multi-Frequency Microwave Field

The basic equations, the boundary conditions, the approximations and the physical mechanism of the free-electron maser interaction have been discussed in the previous sections. In the previous Section, the one-dimensional model is used, in the following a rigourous three-dimensional approach is considered. There are fundamental reasons why a single-frequency approach is not

sufficient for the description of the microwave generation in the FEM. The physical dynamics can only be described with a multi-frequency model. In the remaining sections, the multi-frequency aspects of the free-electron maser interaction are addressed and the final equations that are implemented in the numerical code are derived.

Transverse Structure of the Microwave Field

The natural distance over which a Gaussian wave beam with wavelength λ diverges is the Rayleigh length $\pi w_0^2/\lambda$, where w_0 is the size of the waist. This effect becomes more important for long wavelengths, as in the FEM. This free-space diffraction will diverge the beam away from the co-propagating electron beam. Therefore, in a practical device, the millimeter wave is confined around the electron beam by means of a waveguide.

The electromagnetic field is described as a sum over vacuum waveguide modes, each of which satisfies the boundary conditions. The electron beam is injected on-axis and only waveguide modes that have a transverse electric field with a maximum on-axis contribute to the interaction.

Optical guiding is the effect of amplification of the radiation field within the narrow electron beam with the result that the cross-section of the radiation field becomes smaller. This results in a redistribution of the radiation power over waveguide modes. In the cases that are considered in this thesis, optical guiding is a marginal effect and will be neglected. We assume that a single mode representation is a good description of the transverse profile of the microwave field. The boundary conditions of the corrugated waveguide are such that the HE_{11}-eigenmode exists,

$$\boldsymbol{a}_{r\perp}(x, y, z, t) = \hat{\mathbf{e}}_x a(z, t) \cos\left(\frac{\pi x}{b}\right) \cos\left(\frac{\pi y}{a}\right), \tag{2.61}$$

where a and b are the dimensions of the rectangular waveguide. For future reference we define $a_{11}(x, y) = \cos\left(\pi x/b\right) \cos\left(\pi y/a\right)$.

Longitudinal Structure of the Microwave Field

The electromagnetic field has a complicated axial and temporal behaviour. This behaviour is contained in the z and t dependence of $a(z, t)$. This amplitude is expressed as a discrete sum over contributions with fixed frequencies $\omega_l = (1 + l/N)\omega_0$, where N determines the resolution ω_0/N and l labels the mode ($l \ll N$),

$$a(z, t) = \sum_{l \ll N} a_l(z) e^{i\left(1 + \frac{l}{N}\right)(k_{z0} z - \omega_0 t)} + \text{c.c.}, \tag{2.62}$$

where (ω_0, k_{z0}) satisfy the real part of the dispersion relation (2.43). The corresponding phase factors are chosen such that they are equal, $v_{ph} = \omega_l/k_{zl} = \omega_0/k_{z0}$. The corresponding wavenumbers $k_{zl} = (1 + l/N)k_{z0}$ lead to wavelengths that fit $N + l$ times in the cavity. The choice of equal phase factors is allowed since the solutions of the full dispersion relation (2.43) corresponding to the frequencies ω_l are all on a line, with only small deviations from $v_{ph} = \omega_0/k_{z0}$. This is depicted in Fig. 2.3, where the dots indicate the approximated sets (ω_l, k_{zl}). For FEM parameters, the difference in the phase factors corresponding to the solutions (ω, k_z) of Eq. (2.43) and the approximated phase factor is smaller than 0.05% for variations in the frequency as large as 10%. This difference in phase velocity corresponds to a shift of less than a wavelength over the undulator region.

In general, the slowly-varying amplitudes $a_l(z)$ are complex quantities. We can describe growth of the microwave field by keeping the z-dependence of $a_l(z)$. Small deviations from the wavenumbers k_{zl} are described by the real part of the phase of $a_l(z)$. Note that the amplitude $a_l(z)$ is independent of t, therefore the frequencies are fixed. The time-dependence is scanned with l points with a resolution of ω_0/N. The amplitudes $a_l(z)$ are assumed to be slowly-varying in z, i.e., $|\partial_z a_l(z)| \ll |k_{zl}a_l(z)|$, which is allowed since the spatial growth occurs at the system size, that is a few orders of magnitude larger than the wavelength of the microwave field (see Eq. (2.15)). On the basis of this inequality, the higher order derivative will be neglected in the wave equation.

The approximated sets (ω_l, k_{zl}) are very close to the electromagnetic-wave solution of the dispersion relation near the relevant intersection, that is marked by the star in Fig. 2.3. Each set (ω_l, k_{zl}) satisfies the dispersion relation (2.43) upto order $\mathcal{O}\left(lk_c^2/(k_{z0}^2 N)\right)$. For parameters of the Free-Electron Maser that is described in the next Chapter, the factor $k_c^2/(k_{z0}^2)$ is of order 4.10^{-3} and l/N is smaller than 10^{-1}.

The multi-frequency field may drastically change the phase space for the electrons with respect to the single frequency case. This is shown in Fig. 2.6. In the figure on the left, the particle motion is shown in the single frequency case. In that case, phase space is periodic with the ponderomotive wavelength $\lambda_{pon} = \lambda_{z0} + \lambda_u$. Trapped electrons are confined in the local potential wells (buckets). The multi-frequency case is represented on the right. In that case, the power of the microwave field is distributed over several frequency components. On the right in Fig. 2.6 the separatrix (dashed line) is plotted in the multi-frequency case, where $N = 5$ and the frequency components $l = \pm 1$ have twenty percent of power of the $l = 0$-component. The overall ponderomotive potential is not split in separate buckets of a ponderomotive wavelength. The structure of the phase space is larger, consisting of N
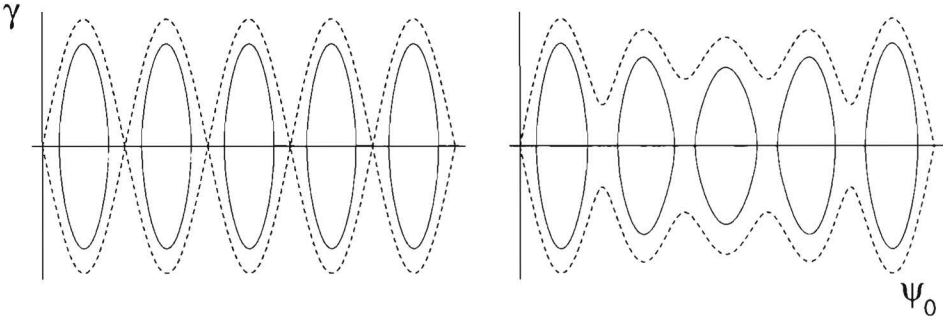
Figure 2.6: *Plotted is the electron energy γ against ψ_0. The dashed line in the figure on the left side is the separatrix for a single frequency case. The dashed line in the figure on the right side is the same separatrix, but disturbed by the microwave field of two neighbouring frequency components $(N = 5, l = 0, \pm 1)$.*

ponderomotive wavelengths, for the case that the difference between two frequencies is a multiple of ω_0/N. It is clear that in general not all electrons will be confined to oscillating trajectories as in the single frequency case. When the contributions of other frequency components are larger, less and less electrons will be confined to local buckets and more and more electrons will move through the whole periodic region in phase space.

The Wave-Equation

The source in the wave-equation (2.1) for the radiation field is the transverse current density that consists of a sum of the contributions of all electrons. The transverse momentum is assumed to be small and the transverse velocity for each electron is approximated to be the undulator induced velocity (2.16). The field of the planar magnetostatic undulator is described by $a_u(x, y, z) = \hat{e}_x a_u(x, y, z) \cos(k_u z)$, where

$$a_u(x, y, z) = \frac{eB_u(z)}{m_e c k_u} \left(1 + \frac{k_u^2 x^2}{4} + \frac{k_u^2 y^2}{4}\right). \tag{2.63}$$

The actual form of $B_u(z)$ is discussed in the next Chapter. When we substitute the corresponding transverse velocity (2.16) in Eq. (2.4), the transverse

current density is

$$
J_x = e \sum_{j=1}^{N_p} \frac{1}{\gamma_j \beta_{zj}} \delta\left(t - t_j\right) \delta\left(\boldsymbol{x}_\perp - \boldsymbol{x}_{\perp j}\right) a_u\left(x_j, y_j, z\right) \cos k_u z. \qquad (2.64)
$$

We substitute the transverse current density (2.64) and the explicit expression for the maser field (2.62) into Maxwell's equation (2.1). After multiplying the resulting expression with $a_{11}(x, y)$ (see below Eq. (2.61)) and integrating over the transverse coordinates, we obtain the paraxial wave equation:

$$
\left[2\left(1 + \frac{l}{N}\right) k_{z0} \partial_z + 2i\left(1 - \beta_{ph}^2\right) \frac{l}{N} k_{z0}^2\right] a_l(z) = \frac{8i}{ab} \frac{e}{m_e \epsilon_0 c^3}
$$
$$
\frac{I}{N_p} \sum_{j=1}^{N_p} \frac{e^{-i\left(1 + \frac{l}{N}\right)\left(k_{z0} z - \omega_0 t_j\right)}}{\gamma_j \beta_{zj}} a_{11}\left(x_j, y_j\right) a_u\left(x_j, y_j, z\right) \cos k_u z. \qquad (2.65)
$$

Terms of order $\mathcal{O}\left((1 - \beta_{ph}^2) k_{z0}^2 l^2 / N^2\right)$ and the second order derivative of the slowly-varying amplitude $a_l(z)$ are neglected in the wave operator. The normalising factor is the electron beam current I, defined as $I/N_p = e v_{ph}/N\lambda_{z0}$, where N_p is the total number of electrons in the device.

2.5   The Longitudinal Space-Charge Field

The longitudinal space-charge field results from the motion of the electrons in the ponderomotive potential well. This motion leads to bunching and thus to space-charge forces. The longitudinal space-charge field is solved from

$$
\left(\nabla^2 - c^{-2} \partial_t^2\right) E_z = \epsilon_0^{-1}\left(\partial_z \rho + c^{-2} \partial_t J_z\right). \qquad (2.66)
$$

The continuity equation (2.5) gives a relation between the charge and current density, $\partial_t \rho = -\partial_z J_z$, when $|\nabla_\perp \cdot \boldsymbol{J}_\perp| \ll |\partial_z J_z|$. The latter approximation is justified since in a planar undulator the transverse current density is $J_x = ec\delta n a_u/\gamma$. In the focussing forces of the undulator field and assuming that the density of the electron beam is $n(r) = n_0(1 - r^2/r_b^2)$, it is found that $|\partial_x J_x/\partial_z J_z| \simeq (k_u^2 + 1/r_b^2) r a_u/(k_z + k_u)\gamma \ll 1$. The beam density ρ is perturbed because of the motion of the electrons in the ponderomotive potential well. In the multi-frequency approach adopted in the previous Section, the beam density may be written as $\rho = \sum_l \rho_l \cos k_u z \exp(i[k_{zl} z - \omega_l t])$, where ρ_l is slowly-varying in temporal position t and spatial position z. This expansion is in agreement with the source of the wave-equation for the radiation

field (2.65). The longitudinal space-charge field E_z is expanded[1] accordingly,

$$E_z(x, y, z, t) = e^{ik_u z} \sum_l E_{zl}(x, y, z) e^{i(1+l/N)(k_{z0}z - \omega_0 t)} + \text{c.c.} \tag{2.67}$$

Substituting the expansions for E_z and ρ in the wave equation for the longitudinal space-charge field (2.66) yields an equation in terms of E_{zl} and ρ_l. With the inverse of the expansion for $\rho_l = I/N_p \sum \delta(x - x_j)\delta(y - y_j) \exp(-i[k_{zl}z + k_u]z - \omega_l t)$, the wave-equation for each mode E_{zl} is

$$\left\{ \nabla_\perp^2 + \left[\frac{\omega_l^2}{c^2} - (k_{zl} + k_u)^2 \right] \right\} E_{zl} = -\frac{i}{\epsilon_0} \frac{(k_{zl} + k_u)^2 - \omega_l^2/c^2}{k_{zl} + k_u}$$

$$\frac{I}{N_p} \sum_{j=1}^{N_p} \delta(x - x_j)\delta(y - y_j) \frac{e^{-i([k_{zl}+k_u]z - \omega_l t)}}{c\beta_{zj}}. \tag{2.68}$$

This equation can be numerically solved on a radial grid [51] or solved analytically, assuming a density profile of the electron beam [52]. For the latter approach, we assume that the longitudinal space-charge field E_z is limited to the electron beam and that the electron charge density ρ has a radial density profile $n(r) = n_0(1 - r^2/r_b^2)$, where r_b is the beam radius. The longitudinal space-charge field is determined by the density and is assumed that it can be written as $E_{zl}(x, y, z) = \hat{E}_{zl}(z)\Psi(r)$. Simplifying this calculation, a circular cross section for the conducting wall of the waveguide at $r = a$ is considered, where $r_b \ll a$, and the effect of the waveguide wall on the space-charge field is very small. With boundary conditions of an infinitely conducting waveguide wall and of continuity of the electric field across the beam boundary, the space-charge field is solved as

$$E_z = \frac{i}{c\epsilon_0} \sum_{l \ll N} \frac{1}{k_{zl} + k_u} \frac{I}{N_p} \frac{2}{\pi r_b^2} e^{i([k_z + k_u]z - \omega_l t)}$$

$$\sum_{j=0}^{N_p} \frac{e^{-i([k_z+k_u]z - \omega_l t_j)}}{\beta_{zj}} \left(1 - \frac{r^2}{r_b^2} - \frac{4}{k_{cl}^2 r_b^2} + \right.$$

$$\left. 2\frac{I_0(k_{cl}^2 r)}{I_0(k_{cl}^2 a)} \left[I_0(k_{cl}^2 a)K_2(k_{cl}^2 r_b) - K_0(k_{cl}^2 a)I_2(k_{cl}^2 r_b) \right] \right) + \text{c.c.}, \tag{2.69}$$

where $k_{cl}^2 = (k_{zl} + k_u)^2 - \omega_l^2/c^2$, I_n are the nth order modified Bessel and K_n are the nth order modified Neumann functions. When $a \gg r_b$ the last term

---

[1] As a basis for expansion of the space-charge field, we are looking for a phase that can represent all harmonics of ψ. Intuitively, one is tempted to try a double sum and try to expand E_z as $E_z = \sum_{ml} E_{z,ml}(z) \exp m\psi_l$, where $\psi_l = (1 + l/N)(k_{z0}z - \omega_0 t) + k_u z$. This expansion has no inverse transformation, which is needed to have an expression for ρ_{ml}, that comes about in the corresponding expansion for the charge density ρ.

may be approximated to $I_0(k_{cl}^2 r)K_2(k_{cl}^2 r_b)$, which is much smaller than one for $r < r_b$ in the case of the FEM.

It is illustrative to contrast the method of solving Eq. (2.66) in the single frequency approach. In the single frequency case, the bucket is split into identical buckets, that are one ponderomotive wavelength long as is shown in Fig. 2.6. In that case, the longitudinal field E_z is expanded into harmonics of this lengthscale [50]–[51]. The higher space-charge harmonics are only important for large amplitudes of the microwave field when the electrons start oscillating in the well. In the multi-frequency case, electrons may travel over several ponderomotive wavelengths in phase space. Therefore, the higher harmonics in the ponderomotive phase ψ are less important for the proper description of the microwave field.

2.6   Electron Motion in the Presence of Radiation

The electron motion in phase space is given by a Hamiltonian system (2.7). Substituting the representations for $\boldsymbol{a}_u$ (2.63) and $\boldsymbol{a}_{r\perp}$ (2.61), (2.62), respectively, in the Hamiltonian and using the approximation $a_{r\perp}^2 \ll a_u^2$, we find

$$\gamma\beta_z = \left\{ \gamma^2 - \left[1 + p_x^2 + p_y^2 + 2p_x a_u \cos k_u z + \frac{1}{2}a_u^2\left(1 + \cos 2k_u z\right) \right. \right.$$

$$\left. \left. -2a_u \cos k_u z \operatorname{Re}\left(\sum_l a_{11}(x,y)a_l(z)e^{i(k_{zl}z-\omega_l t)}\right) \right] \right\}^{\frac{1}{2}}, \quad (2.70)$$

The corresponding equations of motion for an electron interacting with the microwave beam are

$$\frac{\mathrm{d}\boldsymbol{p}_\perp}{\mathrm{d}z} = -\frac{1}{4\gamma\beta_z}\frac{\partial a_u^2}{\partial \boldsymbol{r}_\perp}\left(1 + \cos 2k_u z\right) - \frac{\partial a_{sz}}{\partial \boldsymbol{r}_\perp} + \frac{1}{\beta_z}\frac{\partial \varphi_s}{\partial \boldsymbol{r}_\perp}$$

$$+ \frac{p_x}{\gamma\beta_z}\frac{\partial a_u}{\partial \boldsymbol{r}_\perp}\cos k_u z + \frac{1}{\gamma\beta_z}\frac{\partial a_u}{\partial \boldsymbol{r}_\perp}2\cos k_u z$$

$$\operatorname{Re}\left(\sum_l a_{11}(x,y)a_l(z)e^{i(k_{zl}z-\omega_l t)}\right), \quad (2.71)$$

$$\frac{\mathrm{d}x}{\mathrm{d}z} = \frac{p_x - a_u \cos k_u z}{\gamma\beta_z}, \qquad \frac{\mathrm{d}y}{\mathrm{d}z} = \frac{p_y}{\gamma\beta_z}, \quad (2.72)$$

$$\frac{\mathrm{d}\gamma}{\mathrm{d}z} = -\frac{eE_z}{m_e c^2} - \frac{\beta_{ph}}{\gamma\beta_z}2a_u(x,y,z)\cos k_u z$$

$$\operatorname{Im}\left(\sum_l k_{zl}a_{11}(x,y)a_l(z)e^{i(k_{zl}z-\omega_l t)}\right), \quad (2.73)$$

$$\frac{\mathrm{d}ct}{\mathrm{d}z} = \frac{1}{\beta_z}.\tag{2.74}$$

The slowly-varying self-fields ϕ_s and a_{sz} are determined by Eq. (2.18). In the cases that are considered, the field amplitudes vary quite strongly over an undulator period, due to the large gain of the system as well in the small signal as in large signal regimes. In the latter case, besides the large variation of the microwave field during one pass, also the electron energy varies strongly. Therefore, the standard procedure of averaging the equations of motion over an undulator period is dangerous and will not be employed.

The phase velocity of the microwave field is higher than the velocity of the electrons. As a consequence, the electrons stay behind approximately one wavelength per undulator period. This effect is called slippage and is taken fully into account in our description. The system, consisting of the equations of motion for the electrons (2.71) -(2.74) and the two wave-equations Eq. (2.65) and Eq. (2.69), is solved numerically. The multi-frequency code that solves this system is described in the next Chapter.

References of Chapter 2

[1] T.C. Marshall, *Free Electron Lasers*, (Macmillan, New York, 1985).

[2] W.B. Colson, C. Pellegrini, and A. Renieri, *Laser Handbook: Free-Electron Lasers*, (North Holland Press, 1990).

[3] P. Luchini and H. Motz, *Undulators and Free Electron Lasers*, (Clarendon Press Oxford, 1990).

[4] Charles A. Brau, *Free-Electron Lasers*, (Academic Press, 1990).

[5] H.P. Freund and T.M. Antonsen, jr, *Principles of Free Electron Lasers*, (Chapman and Hall, 1992).

[6] G. Dattoli, A. Renieri, and A. Torre, *Lectures on the Free Electron Laser Theory and Related Topics*, (World Scientific, 1993).

[7] H. Motz, "Applications of radiation from fast electron beams", J. Appl. Phys. **22** (1951) 527.

[8] H. Motz, W. Thon, and R.N. Whitehurst, "Experiments on radiation by fast electron beams", J. Appl. Phys. **24** (1953) 826.

[9] R.M. Phillips, "The ubitron, a high power travelling-wave tube based on a periodic beam interaction in unloaded waveguide", IRE Trans. Electron. Devices **ED-7** (1960) 231.

[10] R.M. Phillips, "History of the Ubitron", Nucl. Instrum. Methods A **271** (1988) 1.

[11] J.M.J. Madey, "Stimulated emission of Bremsstrahlung in a periodic magnetic field", J. Appl. Phys. **42** (1971) 1906.

[12] J.M.J. Madey, H.A. Schwettmann, and W.M. Fairbank, "A free-electron laser", IEEE Trans. Nucl. Sci. **NS-20** (1973) 980.

[13] W.B. Colson, "Theory of a free-electron laser", Phys. Lett. A **59** (1976) 187.

[14] W. Becker, "Multiphoton analysis of the free-electron laser", Opt. Commun. **33** (1980) 69.

[15] G. Dattoli, J. Renieri, and M. Richetta, "Quantum statistical properties of free-electron lasers oscillators", IEEE J. Quantum Electron. **QE-21** (1985) 1069.

[16] J. Gea-Banacloche, G.T. Moore, R.R. Schlicher, M.O. Scully, and H. Walter, "Soft X-ray free-electron laser with a laser undulator", IEEE J. Quantum Electron. **QE-23** (1987) 1558.

[17] J.D. Jackson, *Classical Electrodynamics*, (John Wiley & Sons, Inc.) 1962.

[18] L.R. Elias, W.M. Fairbank, J.M.J. Madey, H.A. Schwettmann, and T.I. Smith, "Observation of stimulated emission of radiation by relativistic electrons in a spatially periodic transverse magnetic field", Phys. Rev. Lett. **36** (1976) 717.

[19] D.A.G. Deacon, L.R. Elias, J.M.J. Madey, G.J. Ramian, H.A. Schwettmann, and T.I. Smith, "First operation of a free-electron laser", Phys. Rev. Lett. **38** (1977) 892.

[20] H.P. Freund and V.L. Granatstein, "Long wavelength free-electron lasers in 1994", Nucl. Instrum. Methods A **358** (1995) 551;
H.P. Freund and V.L. Granatstein, "Long wavelength free-electron lasers in 1995", Nucl. Instrum. Methods A **375** (1996) 665.

[21] W.B. Colson, "Short wavelength free-electron lasers in 1994", Nucl. Instrum. Methods A **358** (1995) 555;
W.B. Colson, "Short wavelength free-electron lasers in 1996", Nucl. Instrum. Methods A **375** (1996) 669.

[22] J.P. Blewett and R. Chasman, "Orbits and fields in the helical wiggler", J. Appl. Phys. **48** (1977) 2692.

[23] P. Diament, "Electron orbits and stability in realizable and unrealizable wigglers of free-electron lasers", Phys. Rev. A **23** (1981) 2537.

[24] E.T. Scharlemann, "Wiggler plane focussing in linear wigglers", J. Appl. Phys. **58** (1985) 2154.

[25] H. Motz and M. Nakamura, "Radiation of an electron in an infinitely long waveguide", Ann. Phys. **7** (1959) 84.

[26] W.B. Colson, "The nonlinear wave equation for higher harmonics in free-electron lasers", IEEE J. Quantum Electron. **QE-17** (1981) 1417.

[27] J.M.J. Madey, "Relationship between mean radiated energy, mean squared energy and spontaneous power spectrum in a power series expansion of equations of motion in a free-electron laser", Il Nuovo Cimento B **50** (1979) 64.

[28] N.M. Kroll, "Relativistic synchrotron radiation in a medium and its implications for stimulated shock radiation", in *Physics of Quantum Electronics: Free-electron generators of coherent radiation*, **7** (1980) 335.

[29] H.P. Freund, P. Sprangle, D. Dillenburg, E.H. da Jordana, B. Liberman, and R.S. Schneider, "Coherent and incoherent radiation from free-electron lasers with an axial guide field", Phys. Rev. A **24** (1981) 1965.

[30] G. Spindler and G. Rentz, "On the sideband structure of free-electron laser emission spectra", Phys. Plasmas **3** (1996) 39.

[31] W.B. Colson, "One-body electron dynamics in a free-electron laser", Phys. Lett. A **64** (1977) 190.

[32] A.A. Kolomenskii and A.N. Lebedev, Sov. J. Quantum Electron. **8** (1978) 879.

[33] N.M. Kroll and W.A. McMullin, Stimulated emission from relativistic electrons passing through a spatially periodic transverse magnetic field, Phys. Rev. A **17** (1978) 300.

[34] V.L. Granatstein, S.P. Schlessinger, M. Herdon, R.K. Parker, and J.A. Pasour, Phys. Rev. Lett. **30** (1977) 384.

[35] A. Hasegawa, Bell Syst. Tech. J. **57** (1978) 3069.

[36] P. Sprangle and A.T. Drobot, J. Appl. Phys. **50** (1979) 2652.

[37] P. Sprangle and R.A. Smith, "Theory of free-electron lasers", Phys. Rev. A **21** (1980) 293.

[38] P. Sprangle, C.M. Tang, and C.W. Roberson, Nucl. Instrum. Methods A **239** (1985) 1.

[39] C.W. Roberson and P. Sprangle, "Review of free-electron lasers", Phys. Fluids B **1** (1989) 3.

[40] N.M. Kroll, P.L. Morton, and M.N. Rosenbluth, "Free-electron lasers with variable parameter wigglers", IEEE J. Quantum Electron. **QE-17** (1981) 1436.

[41] D. Prosnitz, A. Szoke, and V.R. Neil, Phys. Rev. A **24** (1981) 1436.

[42] T.M. Antonsen, Jr, and B. Levush, "Mode competition and control in free-electron lasers", Phys. Rev. Lett. **62** (1989) 1488.

[43] D. Iracane and H. Delbarre, "Stability of a free-electron lasers spectrum in the continuous beam limit", Phys. Rev. Lett. **66** (1991) 33.

[44] D. Iracane, P. Chaix, and J.L. Ferrer, "Spectral behavior of high-power Compton free-electron lasers. I. Broadening and asymptotic equilibrium", Phys. Rev. E **49** (1994) 800.

[45] D. Iracane, P. Chaix, and H. Delbarre, "Spectral behavior of high-power Compton free-electron lasers. II. Effect on filtering and tapering on sideband generation", Phys. Rev. E **49** (1994) 815.

[46] H.P. Freund, "Space-charge effects in free-electron lasers", Nucl. Instrum. Methods A **331** (1993) 496.

[47] C.S. Liu and V.K. Tripathi, *Interaction of electromagnetic waves with electron beams and plasmas*, (World Scientific, 1994).

[48] D.B. McDermott and T.C. Marshall, A kinetic small signal gain analysis of a planar wiggler FEL, operating in the high harmonic (strong wiggler) regime, Phys. Quantum Electron. **7** (1980) 509.

[49] P.W. Milonni and J.H. Eberly, *Lasers*, (John Wiley & Sons, 1988).

[50] J.B. Murphy, C. Pellegrini, and R. Bonifacio, "Collective instability of a free-electron laser including space charge and harmonics," Optics Comm. **53** (1985) 197.

[51] P. Jha and J.S. Wurtele, "Three-dimensional simulation of a free-electron laser amplifier," Nucl. Instrum. Methods A **331** (1993) 477.

[52] E.T. Scharlemann, W.M. Fawley, B.R. Anderson, and T.J. Orzechowski, "Comparison of the Livermore microwave FEL results at ELF with 3D numerical simulation," Nucl. Instrum. Methods A **250** (1986) 150.

[53] E.L. Saldin, E.A. Schneidmiller, and M.V. Yurkov, Method for calculating the space charge effects in a free-electron laser, Optics Comm. **103** (1993) 205.

Chapter 3

The Numerical Free-Electron Maser

Abstract *The free-electron maser, that is being constructed at the FOM Institute for plasma physics 'Rijnhuizen', is described in this Chapter. This device is a source of high-power, tuneable microwave radiation that will be used for heating of magnetised (tokamak) plasmas. A crucial part of the free-electron maser is the step-tapered undulator that consists of two sections with equal periodicity and polarisation. The magnetic field amplitude of the second section is lower, so that the electrons stay in resonance while amplifying the microwave field. This undulator improves the efficiency. The undulator is embedded in a low-quality cavity, and the microwave field is guided in a rectangular corrugated waveguide. The complex dynamics of the spectral behaviour of this free-electron maser is analysed. This requires numerical calculations. The description of the multi-frequency code MFF is presented. This code treats the microwave beam as a sum over discrete cavity modes in the paraxial approximation. The trajectories of the electrons are calculated in the six dimensional phase space. The electron density is so high that the space-charge forces are important. The free-electron maser operates in the intermediate regime between the high-gain Compton and the Raman regime. The relevant space-charge fields are included in the numerical code.*

3.1   Introduction

The Free-Electron Maser (FEM) is a source of continuous, high-power, tuneable, coherent radiation with wavelengths in the millimeter range. A free-electron maser [1]–[5] is under construction at the FOM-Institute for Plasma Physics 'Rijnhuizen' in the Netherlands. This device must demonstrate the feasibility of the free-electron maser in the frequency interval 130–260 GHz. We note that, theoretically, there is no limit on the frequency. A source that generates microwave radiation with high power at these high frequencies will have new applications. Tunability of the operating frequency gives further advantages.

One of the applications of high-power microwave radiation is electron cyclotron plasma heating in next generation experimental magnetic confinement reactors for thermonuclear fusion, for example, the international tokamak ITER. It is foreseen that in these reactors the microwave beam will be applied among others for plasma start-up assist, heating, current drive and disruption control. At present, the designed heating power on ITER in the electron cyclotron range is expected to be 50 MW. This requires megawatt power units.

Microwave radiation is absorbed by the electron population of thermonuclear plasmas if the frequency of the applied microwave beam is in resonance with a harmonic of the electron cyclotron frequency f_{ce}

$$f_{ce} = \frac{eB}{2\pi m_e} \simeq 28\, B\,(\mathrm{T})\,\mathrm{GHz}. \tag{3.1}$$

Reviews in this field are Refs. [6, 7]. Note that in a tokamak, the magnetic field is inversely dependent on the radius $B(r) \sim 1/r$, therefore the power deposition is at a specific radial position. In ITER, heating with EC-power at start-up is expected to require heating power with a frequency of 90–135 GHz [8]. Off-axis heating requires 130–220 GHz. Furthermore, current drive is achieved with frequencies ranging from 220–260 GHz.

The advantage of the FEM over other sources in this domain are tunability, higher frequencies and higher power. The generated microwave power in a free-electron maser can in principle be pushed to higher levels continuous power than in its nearest competitor, the gyrotron. This is mainly because the interaction region in the free-electron maser is a few orders of magnitude larger.

The fast tunability of the operating frequency is achieved by adjusting the beam energy. The profile of the reflection coefficient is small, therefore, for large shifts of the frequency, the reflecting structure must be adjusted at the same time. The latter is mechanical, therefore, the operating frequency

is changed over a large frequency interval on a timescale of a minute. The frequency can fast be adjusted over 5% when the reflecting structure is fixed.

The tunability allows one source of microwave power to cover the desired frequency range. The frequency can be tuned within a minute from the frequency that is used at start-up, i.e. 90–135 GHz, to a frequency that is required for heating or current drive at the desired position in the plasma.

Applications of the fast adjustable frequency over 5% are control of the temperature and current profile in tokamaks and disruption control. The place where the power is deposited can continuously be adapted at a position in the plasma depending on current penetration. The power deposition must be localised in order to satisfy the conditions at which the temperature and current profile can be controlled and hence it is required that the microwave power is emitted in a narrow frequency profile. In the next chapters, we will show that the FEM indeed lases in a narrow frequency profile.

The control of disruptions is of major concern in the design of the next generation magnetic confinement reactors. Due to the damage of the large forces on the vessel, the tokamak can tolerate a small number of disruptions. Control and prevention of disruptions by heating or current drive in and around magnetic islands can be done in feedback mode to track the position of the islands in space. Another method to prevent disruptions in these future tokamaks relies on the control of the current profile by local ECCD [9] at the magnetic surface with magnetic winding number of the field lines $q = 2$. The power deposition should follow the $q = 2$ surface and, therefore, this requires a fast adaptable frequency over 5% and microwave power in a narrow frequency profile. Recent experimental results on control of the current profile by local heating are encouraging [10].

3.2   The FOM Free-Electron Maser

The FOM-FEM is under construction at the FOM-Institute for Plasma Physics 'Rijnhuizen' in the Netherlands. This device will demonstrate its ability for heating and current drive on the Rijnhuizen tokamak RTP. The parameters of the FEM are given in Table 3.1. The free-electron maser employs a continuous electron beam that is generated by a gun and accelerated upto the desired energy. A planar undulator gives a periodic deflection on the electron beam. The generated microwave beam is guided by a waveguide and is contained in a low-quality cavity. In order to generate power in frequencies from 130 GHz to 260 GHz, an electron beam with energies between 1.35 MeV and 2 MeV is needed. The electron extraction efficiency is around 6%, therefore, the high output power is reached with an electron current of 12 A. The

electron beam voltage (γ)	1.35–2 MeV
microwave frequency	130–260 GHz
microwave power	> 1 MW
pulse length	100 ms
electron beam current (I)	12 A
electron beam loss current	< 20 mA
normalised electron beam emittance	50 π mm mrad
electron beam radius (at entrance)	1.3 mm
Peak undulator field in section 1 (B_{u1})	0.20 T
Peak undulator field in section 2 (B_{u2})	0.16 T
number of undulator periods in section 1 (N_1)	20
number of undulator periods in section 2 (N_2)	14
undulator period (λ_u)	4.0 cm
length of the gap between the undulators	6.0 cm (adjustable)
waveguide mode	HE_{11}
waveguide dimensions $(a \times b)$	20 × 15 mm
reflection coefficient of microwave system	0.29 (adjustable)

Table 3.1: *Parameters of the FOM Free-Electron Maser.*

FEM employs an electron beam with high current density so that the FEM operates in the intermediate regime between the high-gain Compton and the Raman regime. This implies that collective effects play an important role in the interaction.

Initially, the energy spread of the electron beam is very small. After interaction with the microwave beam, the electron beam still has high energy. The energy distribution at the exit of the undulator is calculated with the numerical code MFF and is plotted in Fig. 3.1. In this figure, the initial electron distribution is indicated by the dashed line. The initial energy is $\gamma = 4.425$ and the energy spread of the electron beam is about 0.5%. After interaction with the microwave beam, there are three peaks in the energy distribution for the electrons. The peak at the highest energy consists of electrons that are accelerated in the first section. The electrons in the peak at the lowest energy have amplified the radiation field in both the first and the second undulator section. The electrons at intermediate energies are decelerated in the first and accelerated in the second section.

An efficient recovery of the unspent electron beam leads to high overall efficiency. For this purpose the free-electron maser is equipped with a decelerator and a depressed collector. The decelerator slows down the electrons to low axial velocity. The beam is deflected off-axis by a rotating magnetic field,
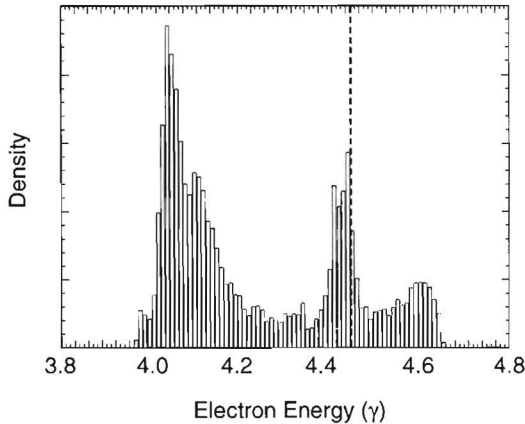
Figure 3.1: *The numerically calculated energy distribution of the electron beam after interaction with the high-power microwave beam at saturation with operating frequency of 195 GHz. The initial energy distribution is indicated by the dashed line.*

to prevent the power deposition of the beam at one particular spot. Three collector plates at different voltages decelerate the electrons backwards and guide them away from the axis. With this setup, the energy of the secondary electrons is low and therefore, these electrons cannot escape. Three collector plates are necessary in order to efficiently recover the charge and energy of the electrons, as each plate recovers a peak in the energy distribution (see Fig. 3.1).

3.2.1   The Step-Tapered Undulator

A key element of the present design is a step-tapered undulator [11] which is essential in order to provide simultaneously a high gain and a high efficiency. A step-tapered undulator consists of two planar hybrid magnet undulators with different lengths and field-strengths. The two sections have the same undulator period and polarisation. The first section consists of 20 periods of 4 cm and with peak magnetic field of 0.2 T. The second section is slightly shorter and consists of 14 periods and a peak magnetic field of 0.16 T. The second section has lower undulator field so that the electrons stay in resonance while amplifying the microwave field. The undulator provides a large linear gain in the small-signal regime, providing a fast start-up of the microwave power. At high microwave power, the second section will act as an amplifier of the microwave power generated in the first section.

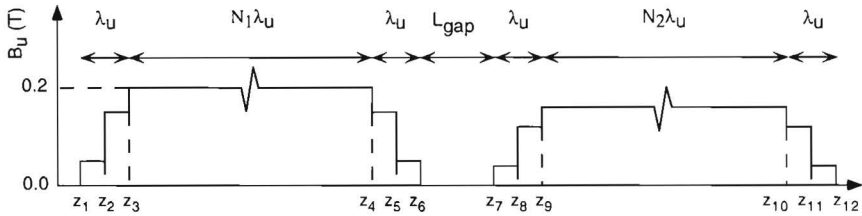The electron beam line is straight from cathode to anode and starts with

Figure 3.2: *Sketch of the profile of the magnetic field amplitude $B_u(z)$ of the step-tapered undulator. Matching cells at both ends of the sections ensure the electron beam to wiggle symmetrical with respect to the undulator axis.*

an electron gun and an electrostatic accelerator. The cross section of the generated electron beam is supposedly circular and the density profile is a step-function. The electron beam radius is kept large outside the undulator (10–15 mm) in order to reduce radial space-charge forces. At the entrance of the undulator, the electron beam cross section is circular and is an image of the cathode [12]. There, the radius is in the order of 1–1.3 mm.

In order to keep the beam centered, each undulator has matching cells at both ends. These cells have lengths of half an undulator period and strengths of $\frac{1}{4}$ and $\frac{3}{4}$ of the central part of the section. Side arrays of correction magnets provide additional adjustable focussing forces on the electron beam, so that there are focussing forces in both transverse directions. These forces shape the undulator field such that via a combination of sextupole and quadrupole fields the focussing strength is equal in both transverse directions. The undulator field is given by Eq. (2.63), where the on-axis field strengths of the two sections and their matching cells are

$$
\begin{aligned}
B_u(z) \;=\; & B_{u1} \sum_{i=1}^{5} f_i \left(h(z - z_i) - h(z - z_{i+1}) \right) + \\
& B_{u2} \sum_{i=1}^{5} f_i \left(h(z - z_{i+6}) - h(z - z_{i+7}) \right),
\end{aligned}
\tag{3.2}
$$

where B_{u1} and B_{u2} are the peak magnetic wiggler fields of the separate sections, as are given in Table 3.1, $h(z)$ is the heaviside function and $f_1 = f_5 = \frac{1}{4}$, $f_2 = f_4 = \frac{3}{4}$, and $f_3 = 1$. The positions z_i along the z-axis are indicated in Fig. 3.2. The two sections are separated by a gap without undulator field. For the FEM, the gap has variable length of about 1–2 undulator periods.
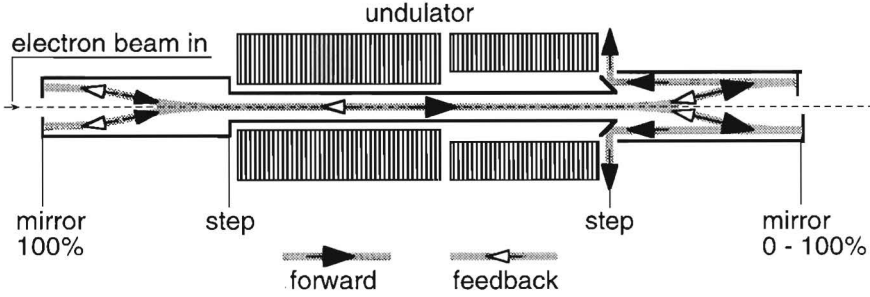
Figure 3.3: *Sketch of the cavity consisting of a waveguide and reflecting structures. Steps in the waveguide split the waveguide mode into two off-axis modes, that are reflected by off-axis mirrors. The shift in axial position of the mirrors determines the part of the microwave power that is coupled out.*

3.2.2   The Microwave Cavity

The low-quality cavity consists of a waveguide with mirrors formed by partially reflecting structures. The cavity must handle circulating microwave power over 1 MW.

   The microwave beam is guided by an oversized, rectangular waveguide with internal dimensions of 15 mm × 20 mm, that has corrugated vertical sides, that are perpendicular to the high-frequency field and parallel to the magnetic field of the undulator. The corresponding waveguide modes are the plane polarised HE_{mn} modes. The odd modes have a maximum amplitude on-axis, which is required for good coupling between the electron beam and the microwave beam. Numerical simulations [13, 14] show that the fundamental waveguide mode HE_{11}, see Eq. (2.61), is the dominant contribution. The higher order modes only appear in the small-signal regime and their power reaches a maximum of 10

   The reflection and outcoupling structures in the waveguide consist of special mirrors such that the microwave beam is coupled out sideways. The cross section of the waveguide changes step-wise from 15 mm × 20 mm to a_{step} × 20 mm just outside the undulator. This is schematically depicted in Fig. 3.3. The step in the waveguide dimensions leads, after a distance of $L = a_{step}^2/(2\lambda)$, to the separation of the microwave beam in two off-axis beams [3, 15]. The two beams are reflected by off-axis mirrors. This setup separates the outcoupling of the electron and microwave beam, leaving the electron beam undisturbed. Downstream, the mirrors have different axial positions which induces a phase difference between the two reflected beams. For a phase
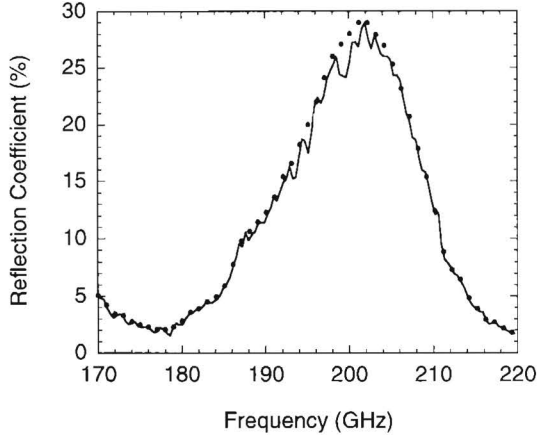
Figure 3.4: *The experimentally measured reflection coefficient of the mirror is indicated by the line. The dots indicate the values that are included in the numerical code MFF.*

difference between 0 and π, one on-axis beam and two off-axis beams are formed while propagating backwards. The two off-axis microwave beams are coupled out. The reflection coefficient can be varied between $0 - 100\%$ of the power, but is typical of the order of 30%. In the upstream structure there is recombination in a single reflected beam and, therefore, total reflection of the power. Note that the height a_{step} is determined by the operating wavelength. This means that adjusting the operation frequency from 130 GHz to 260 GHz requires besides adjusting the electron energy also adjusting the step $a_{step} = \sqrt{2\lambda L}$, where L is the length of the electron beam/microwave splitter.

In the stationary regime the low reflection coefficient is accompanied by a large gain (one over the reflection coefficient). Therefore, the intra-cavity power is at moderate level so that gas breakdown and high Ohmic losses are avoided. An example of the reflection profile is plotted in Fig. 3.4, where the solid line is the experimentally measured reflection coefficient [22]. The reflection profile has 7 GHz half-width. The reflection profile allows a change in frequency over a few percent by changing the electron energy only.

3.3   Spectral Evolution of the FEM

From a physical point of view, the evolution of the spectral power of the FEM is an interesting problem. The distribution of the outcoupled microwave power over the spectrum may change from pass to pass. The dynamics of

this distribution over the passes, we will refer at as spectral evolution. The question is if the spectrum of the free-electron maser evolves toward a narrow band. Furthermore, its stability is of importance.

The spectral evolution of the longitudinal modes is influenced by different factors. The cavity is a low-quality cavity, that couples out more than 70% of the intra-cavity power. This requires a large linear gain in the small-signal regime as well as a large non-linear gain in the stationary regime. The low-quality cavity is expected to generate a broad spectrum. In addition, the different undulator strengths of the two sections of the step-tapered undulator lead to different resonance conditions. The field-free gap between the two sections induces a shift in the relative phase of the microwave field and the undulator field. These effects lead to multiple peaks in the linear-gain curve. Eventually, the microwave power is so high that the FEM is in the nonlinear regime. In this regime, heavy mode competition occurs. The high gain makes the mode-competition vigorous since 'small' perturbations can rapidly grow. Furthermore, it turns out that sidebands are generated. When sidebands are excited, the spectrum may become chaotic and the power of the FEM may be distributed over a wide frequency domain. In that case, the maximum efficiency may vary significantly [16, 17], which is not desirable regarding the design requirements. Hence, the spectral evolution is a complex problem, that is exclusively solved with a multi-frequency treatment.

3.4   The Multi-Frequency FEM Code 'MFF'

As we have seen in the previous Section, investigation of the spectral behaviour of the FEM is required. Multi-frequency numerical calculations are necessary to investigate the complex longitudinal behaviour of the FEM. The numerical code MFF (Multi-Frequency FEM) calculates the spectral dynamics of the generated microwave beam. In this code, the system of equations for the individual electron trajectories and the evolution of the electromagnetic fields is solved self-consistently. The code permits the inclusion of many physical effects like non-uniform undulators and non-ideal electron beams. Basically, the FEM is a continuous device. Hence, the electron beam as well as the radiation field are treated in the continuous beam limit. The velocity of the electrons is lower than the velocity of the radiation field. As a result, the electrons slip approximately one wavelength per undulator period behind the microwave field during their transit through the undulator. This is an important effect, since in the multi-frequency approach the radiation field varies in time t.

The equations that are solved in the numerical code are the wave equation

for the microwave field (2.65), the wave equation for the longitudinal electric field (2.69) and the equations of motion (2.71)–(2.74) for N_p electrons. The $6N_p$ particle equations are solved with the Runge-Kutta method [23]. The 3D treatment of the electrons is important for the proper description of the large transverse excursions that the electrons make in the FEM. The sources for the wave equations consist of the contributions of all electrons. This set of equations is supplemented with initial conditions on the phase space variables $(\gamma, t, p_x, x, p_y, y)$ at the undulator entrance and on the initial electromagnetic field. The undulator field (2.63) is implemented in the numerical code. The z-dependence of the on-axis maximum magnetic field $B_u(z)$ is given by Eq. (3.2). The numerical code is written for an oscillator configuration, which means that multiple roundtrips through the cavity are calculated. Fresh electrons are injected continuously. Outside the step-tapered undulator region the microwave propagates in vacuum and the phase velocities of all frequency components are equal. The evolution of the field in this region is integrated in one step by multiplying the field at the end of the undulator by a mere reflection coefficient. The resulting field is the initial field for the next roundtrip. The reflection coefficient for the microwave beam is frequency dependent. Different profiles for the reflection coefficient will be considered. The actual measured reflection profile is implemented in the numerical code, which is plotted in Fig. 3.4.

Initial Conditions

The initial conditions at the entrance of the undulator at $z = 0$ are given in terms of the electron distribution function $\mathcal{F}(\gamma, t, p_x, x, p_y, y)$ in the 6 dimensional phase space. It is assumed that the distribution $\mathcal{F}$ can be written as $\mathcal{F}_t(t)\mathcal{F}_\gamma(\gamma)\mathcal{F}_4(p_x, x, p_y, y)$, where $\mathcal{F}_t(t)$ is evenly distributed over a fixed number (typically $4N$) of positions in the interval $[0, 2\pi N/\omega_0]$ in t-space. The initial electron energy distribution $\mathcal{F}_\gamma(\gamma)$ is Gaussian in γ. The distribution $\mathcal{F}_4(p_x, x, p_y, y)$ is a 4-D ellipsoid with minor axes Δp_x, r_{bx}, Δp_y and r_{by} that is filled with the Hammersley sequence [24]. The electron beam radius is determined by r_{bx} and r_{by}. The maxima of the distributions for p_x and p_y are determined by the emittance of the beam, $\Delta p_{x,y} = \epsilon_{nx,ny}/r_{bx,by}$, where $\epsilon_{nx,ny}$ is the normalised emittance in both radial directions.

The initial power and phase of each contribution to the microwave field is defined at the undulator entrance before the first pass. The initial longitudinal electric field vanishes, since the axial electron distribution is uniform.

Integration

The integration of the wave equation is done with a first order forward difference scheme. The z-axis is discretised in intervals with end points at

z_{n-1} and $z_n = z_{n-1} + \Delta z$. The centre point of each interval is defined as $z_{n-1/2} = (z_n + z_{n-1})/2$. The particle phase space variables are known at positions z_{n-1} and the electromagnetic fields (radiation field and self-fields) at positions $z_{n-1/2}$. Using the solution of the electromagnetic fields at $z_{n-1/2}$, the particles are advanced from z_{n-1} to z_n. Subsequently, the Maxwell sources are constructed from the new particle variables at z_n. With the new Maxwell sources at z_n, the radiation field at $z_{n-1/2}$ is advanced to $z_{n+1/2}$. In this way the centering of z of the wave equation discretisation is assured.

The DC-space-charge forces

The DC-space-charge forces (Eq. 2.20 in Section 2.2.1) are implemented in the code. This is a radially outward force on the electron beam. In the calculation of these forces, a density profile for the electron beam is considered. The DC-forces are used to calculate the trajectories of the individual electrons. The undulating motion of the electron beam is large with respect to the beam dimensions, see Fig. 3.5, therefore, each integration step the centre and radius of the electron beam is calculated.
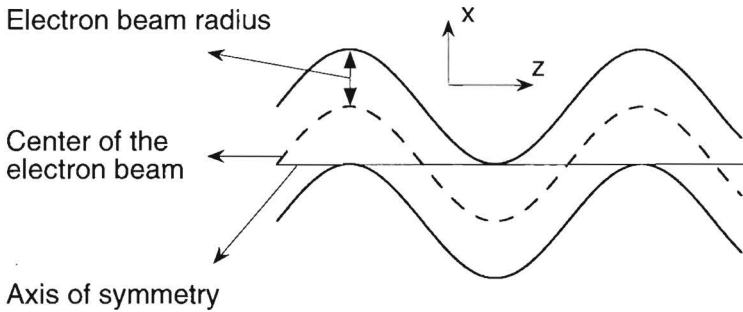

Figure 3.5: *Each integration step the radius of the electron beam is calculated from the centre of the electron beam.*

Typical parameters of the calculations

The parameters that are used to obtain the results that are presented in the following Chapters are carefully determined. With these parameters, the numerical errors are minimal and the calculations are stable. The typical parameters are $N = 200$, which gives a frequency spacing (ω_0/N) of about 1 GHz, with the central frequency (ω_0) at 200 GHz. The number of modes l is such that the total gain curve is described, which is typically 60. The number of particles is about $N_p = 40N$. The number of steps in the longitudinal direction is typically 20 identical steps per undulator period. The parameters

of the physics, i.e. electron energy, undulator strength etc., are those of the
design of the FOM FEM for Fusion applications that are given in Table 3.1.

3.5   Wiggle-Averaged Results

In general, the electron equations and Maxwell's equations may be averaged
over the period of the undulator oscillation [25] when the radiation field
varies little over an undulator period. In the FEM, the undulator is a few
gainlengths long. Therefore, the amplitude of the electromagnetic field may
not be considered constant during one pass and also not over an undulator
period. This means that for FEM parameters averaging over an undulator
period is questionable.

   Nevertheless, it is worthwhile to show the effect of averaging the equations
over an undulator period. The averaging is partial. In the equations of
motion, only the undulator field is averaged. In the source term for the
microwave field (2.65), the oscillation with twice the undulator period is
averaged. The electromagnetic fields of the radiation and space-charge may
vary over the undulator period, therefore, the z-dependence of these fields are
kept. In the simulations, these fields vary significantly and in order to have
the same numerical accuracy, the step-size in the averaged and non-averaged
simulations are about the same.
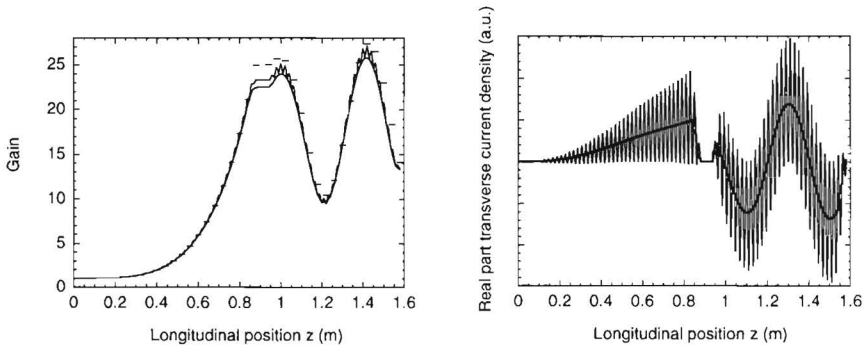
Figure 3.6: *Comparison of averaged and non-averaged calculations in the
small-gain regime. On the left, two gaincurves are plotted as a function
of the longitudinal position z; a smooth curve and a curve that contains
fast oscillations. In addition the bars indicate the solution of the averaged
equations, where the microwave field is constant over an undulator period.
On the right, the real part of the transverse current density is depicted.*
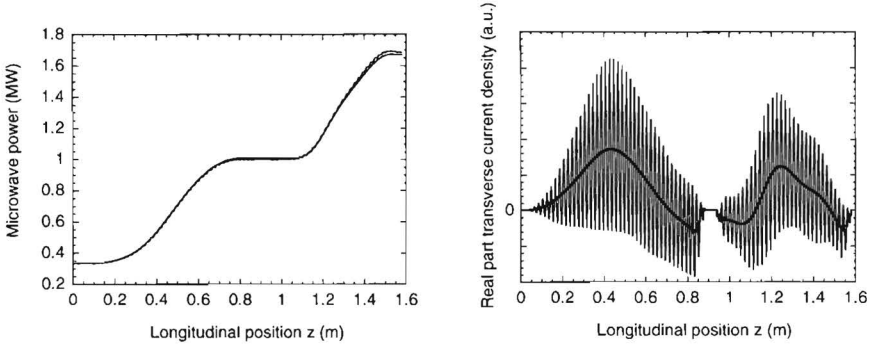
Figure 3.7: *Comparison of averaged and non-averaged calculations at saturation. On the left, the power in the microwave beam is plotted as a function of the longitudinal position z. On the right, the real part of the transverse current density is given.*

Figure 3.6 applies to the small-signal Compton regime. The figure on the left shows two local gain curves that are defined as the ratio of the microwave power at longitudinal position z over the microwave power at the entrance of the undulator $z = 0$. The smooth one is the solution of the averaged equations and the other the solution of the nonaveraged equations. In the figure on the right we show the current density. There is a large difference between the solution of the averaged and nonaveraged equations. The latter oscillates with twice the undulator period, see Eq. (2.65). In Fig. 3.7 the same is shown as in Fig. 3.6, but in the saturated regime. In addition, the bars in Fig. 3.6 indicate the local gain in the case the microwave field and the space-charge fields are constant over an undulator period.

It is clear that the wiggle motion has only a small influence on the power and gain. The solution of the averaged equations are almost indistinguishable from the solutions of the non-averaged equations for these quantities. For parameters of the FEM, the difference between the solutions of the averaged and non-averaged equations is less than 10%. For the transverse current density, the solution of the averaged equations is almost the same as the averaged solution of the non-averaged equations. Although the differences are small, they might lead to large differences due to the nonlinear effects. Therefore, it is important to solve the non-averaged equations.

In comparing Fig. 3.6 and Fig. 3.7, we see that the behaviour of the radiation field and current density in the second section is quite different in the small signal regime and in the large-signal regime. In the small signal regime, the microwave field oscillates in the second section, while at saturation, the

second section amplifies the microwave field.

References of Chapter 3

[1] P.W. van Amersfoort, W.H. Urbanus, A.G.A. Verhoeven, A. Verheul, A.B. Sterk, A.M. van Ingen, and M.J. van der Wiel, "A electrostatic free-electron maser for fusion: design considerations", Nucl. Instrum. Methods A **304** (1991) 168.

[2] W.H. Urbanus, P.W. van Amersfoort, R.W.B. Best, A.B. Sterk, A.G.A. Verhoeven, and M.J. van der Wiel, "A free-electron maser for thermonuclear fusion", Nucl. Instrum. Methods A **318** (1992) 16.

[3] W.H. Urbanus, R.W.B. Best, W.A. Bongers, A.M. van Ingen, P. Manintveld, A.B. Sterk, A.G.A. Verhoeven, and M.J. van der Wiel, "Design of the 1 MW, 200 GHz, FOM fusion FEM", Nucl. Instrum. Methods A **331** (1993) 235.

[4] W.H. Urbanus et. al., "A 130-260 GHz, 1 MW free-electron maser for fusion", Nucl. Instrum. Methods A **358** (1995) 155.

[5] A.G.A. Verhoeven, W.A. Bongers, C.A.J. van der Geer, P. Manintveld, F.C. Schüler, W.H. Urbanus, and M.J. van der Wiel, "A broad-tuneable free electron maser for ECW applications", Proceedings of the ninth joint workshop on electron cyclotron emission and electron cyclotron heating, Borrego Springs, California, (1995) 309.

[6] M. Bornatici, R. Cano, O. De Barbieri, and F. Engelmann, Nucl. Fusion **23** (1983) 1153.

[7] V. Erckmann and U. Gasparino, "Review Article: Electron cyclotron resonance heating and current drive in toroidal fusion plasmas", Plasma Phys. Contr. Fusion **36** (1994) 1869.

[8] B. Lloyd, P.G. Carolan, and C.D. Warrick, "ECRH-assisted start-up in ITER", AEA FUS 330 (1996).

[9] E. Westerhof, "Requirements on heating or current drive for tearing mode stabilization by current profile tailoring", Nucl. Fusion **27** (1987) 1929.

[10] D.C. Sing, M.E. Austin, D.L. Brower, J.Y. Chen, R.F. Gandy, C.X. Yu, X.-H. Wang, A. Bhattacharee, and D.D. Schnack, "Suppression of $m = 2$ islands by electron cyclotron heating in the Texas Experimental Tokamak: Experiment and theory", Phys. Fluids B **5** (1993) 3239.

[11] A.A. Varfolomeev, S.N. Ivanchenkov, A.S. Khlebnikov, N.S. Osmanov, M.J. van der Wiel, W.H. Urbanus, and V.F. Pavluchenkov, "Performance of the undulator for the FOM-FEM project", Nucl. Instrum. Methods A **341** (1994) 466.

[12] M. Caplan, M. Valentini, C. van der Geer, and W. Urbanus, "Design and characterization of the DC acceleration and transport system required for the 1 MW free electron maser experiment", Nucl. Instrum. Methods A **375** (1996) 91.

[13] M. Caplan, R.W.B. Best, A.G.A. Verhoeven, M.J. van der Wiel, W.H. Urbanus, V.L. Bratman, and G.G. Denisov, "Predicted performance of a DC beam driven FEM oscillator designed for fusion applications at 200-250 GHz", Nucl. Instrum. Methods A **331** (1993) 243.

[14] A.V. Tulupov, M.J. van der Wiel, W.H. Urbanus, and M. Caplan, "Simulations of the performance of the FEM oscillator for fusion at 130-250 GHz", Nucl. Instrum. Methods A **341** (1994) 305.

[15] L.A. Rivlin and V.S. Shil'dyaev, Izv. Vuzov Radiofizika 11 (1968) 572.

[16] R.W. Warren et. al., "Near ideal lasing with uniform wigglers", Nucl. Instrum. Methods A **285** (1989) 1.

[17] A. Bhattacharjee, S.Y. Cai, J.W. Dodd, and T.C. Marshall, "Optical spikes in free electron lasers: theory and experiment", Nucl. Instrum. Methods A **304** (1991) 99.

[18] V.L. Bratman and A.V. Savilov, "Competition of longitudinal modes and the scenario of single-mode regime build-up for the FOM-Fusion-FEM project", Nucl. Instrum. Methods A **358** (1995) 182.

[19] P.J. Eecen, A.V. Tulupov, and T.J. Schep, "Investigation of multi-frequency generation in the FEM", Nucl. Instrum. Methods A **341** (1994) 309.

[20] P.J. Eecen, A.V. Tulupov, and T.J. Schep, "Spectral dynamics of the FEM", Nucl. Instrum. Methods A **358** (1995) 178.

[21] P.J. Eecen, A.V. Tulupov, and T.J. Schep, "Spectral dynamics of a high-power, high gain FEM with a step-tapered undulator", Phys. Rev. E. **52** (1995) 5460.

[22] Private communications W.A. Bongers.

[23] W.H. Press et. al., *Numerical Recipes*, (Cambridge university press, Cambridge, 1986).

[24] J.M. Hammersley and D.C. Handscomb, *Monte Carlo Methods*, (Methuen & Co, London, 1964).

[25] W.B. Colson, "The nonlinear wave equation for higher harmonics in free-electron lasers", IEEE J. Quantum Electron. **QE-17** (1981) 1417.

Chapter 4

Spectral Dynamics of a Step-Tapered Undulator

Abstract *The time evolution of the power spectrum of the step-tapered undulator is investigated. The purpose of this undulator is to enhance the efficiency at high output power. The evolution is analysed with the multi-frequency code MFF. In this Chapter, space-charge forces are disregarded and the results that are obtained will be used as a benchmark for the interpretation in the next Chapters.*

In the small-signal regime, the gain curve of the step-tapered undulator is quite different from the gain curve of each of the two single undulators and of their sum. In the small-signal regime, the gain per pass is so high that the gain as a function of frequency is not the derivative of the spontaneous emission with respect to the frequency. Nonlinear interaction occurs already after a few passes. At saturation the gain remains high because each pass the out-coupled power has to be compensated in the low-quality cavity. The power spectrum evolves towards a state in which the power at the resonant wavelength of the second undulator section is suppressed. In a rather broad parameter regime, the microwave field evolves toward a stable power spectrum consisting of two peaks. The main peak is related to the resonant frequency of the first section, while the second peak is a lower sideband. The influence of the gap length, the relative polarisation of both sections and the reflection coefficient on the spectral behaviour is investigated.

4.1   Introduction

The FOM Free Electron Maser (FEM) is described in Chapter 3. A key element of the design is a step-tapered undulator which is essential in order to provide simultaneously a high gain in the small-signal regime and a high efficiency at high output power. This undulator is described in Section 3.2.1. In the small-signal regime, the fieldfree gap between the two sections induces a phase shift between the electrons and the ponderomotive potential well. This shift modifies the linear gain curve with respect to the sum of the linear gain curves of the two sections. The linear gain is high so that saturation is reached quickly. Then the second section of the undulator is an amplifier of the field that is generated in the first section. We recall that the low quality cavity consists of a waveguide with mirrors formed by partially reflecting structures that are described in Section 3.2.2. The dominant transverse mode in the oversized, rectangular, corrugated waveguide is the HE_{11}-mode.

An important problem is the evolution of the spectrum of the FEM with a step-tapered undulator. The spectral dynamics of the generated microwave beam is numerically analysed with the code MFF that is described in Chapter 3. We recall that space-charge forces play an important role in the physics of the FEM. These fields and there effects are discussed in Chapter 2. As a benchmark, the evolution of the spectrum of a step-tapered undulator is investigated in the Compton limit. In this limit the space-charge forces are negligible and the electrons interact in a potential formed by the undulator and microwave field. The parameters of the FEM that are used in this Chapter are given in Table 3.1, with one modification: since also the DC-forces are disregarded, the electron beam cross section is on average smaller and we will take an initial electron beam radius of $r_b = 1\text{mm}$. The results of this case will be used for the interpretation of the results including all space-charge fields in the following Chapters. The dynamics of the frequency spectrum, starting from noise, is analysed as it grows into the nonlinear regime. In the small-signal regime, the gain of the total system is appreciably larger than the cumulative gain of the separate sections. Although the main peak is still related to the fundamental resonance of the first undulator, it is strongly modified by the presence of the second section.

The gain is so high that the large-signal regime is reached within few passes. In this regime the peak of the fundamental resonance in the first undulator grows strongly, while the peaks at higher frequencies are suppressed. When the power grows beyond a certain value a sideband is generated at the lower frequency side of the surviving peak. No sideband is generated at higher frequencies. It will be shown that the gain distribution of the first section determines the power spectrum of the step-tapered undulator, while

the second section operates as an amplifier of the field that is generated in the first section. The presence of a variable drift section between the two sections of the undulator enables the experiment to modify the interaction in the second undulator section and modify the spectral dynamics. It will be shown that the spectral behaviour can range from coherent to chaotic.

This Chapter is organised as follows. In the next Section, the spontaneous emission and the linear gain that are generated in a step-tapered undulator are calculated. The effect of the length of the fieldfree gap on the spontaneous emission spectrum and the linear gain is analysed. In Section 4.3, the evolution of the power spectrum is analysed numerically. The profile of the reflection coefficient is taken to be wavelength independent. In the interesting parameter region, a stable spectrum is generated that consists of two peaks. The evolution of the main peak and the sideband in the spectrum is discussed and a comparison is made with spectra generated with a single undulator. We note that all presented results in this Chapter refer to the power spectra just before reflection at the adjustable mirror (see Fig. 3.3).

In Section 4.4 the influence of several parameters on the spectrum is investigated. The influence of a wavelength dependent reflection coefficient is investigated. When the frequency profile of the reflection coefficient is narrow enough the sidebands at both sides of the main peak are suppressed. The important effect of the suppression of the sidebands is the drop of power of the main peak in the frequency spectrum. The gap length is varied and the relative polarisation of both sections is changed. It is shown that for different gap lengths the spectra can go from stable to chaotic. Even in the chaotic case, the sidebands at higher frequencies are suppressed.

4.2 Linear Gain

At start-up, an electron beam is injected into the undulator in the absence of a co-propagating microwave field. The electrons that perform an oscillatory motion produce dipole radiation. This 'spontaneous' radiation [1, 2] is emitted in a small forward cone with angular opening of the order of $1/\gamma$ with respect to the direction of propagation of the electron beam. The FEM employs an electron beam with low energy γ. With these low energies the usual expressions for the undulator radiation that keep contributions upto $\mathcal{O}(1/\gamma^2)$ are not correct. The derivation of the spectral brightness that keeps contributions upto $\mathcal{O}(1/\gamma^3)$ is shown in the Appendix A. In contrast to the equations in FEL-literature where angles smaller than $1/\gamma$ are considered, in our derivation angles smaller than $\alpha \sim 1/\gamma^2$ around $\alpha = 0$, which is parallel to the z-axis are considered. For these angles, terms of order $\mathcal{O}(1/\gamma^4)$ are
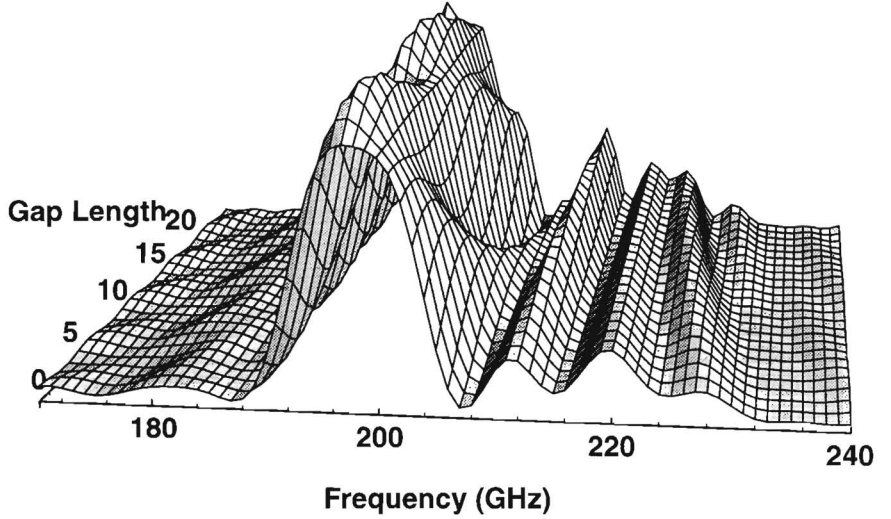
Figure 4.1: *The on-axis spontaneous emission spectrum at the end of the step-tapered undulator as a function of frequency and of gap length. Only the spectrum around the first harmonic of the radiation is depicted. The gap length is given in units of undulator periods.*

neglected. In Appendix A, the spontaneous brightness is given for a general undulator by Eq. (4.7). In the case of the step-tapered undulator, the spectral brightness is

$$
\begin{aligned}
\frac{\mathrm{d}^2 I_{\text{und}}}{\mathrm{d}\omega \mathrm{d}\Omega} = {} & \left(\frac{\mathrm{d}^2 I}{\mathrm{d}\omega \mathrm{d}\Omega}\right)(\text{section I}) + \left(\frac{\mathrm{d}^2 I}{\mathrm{d}\omega \mathrm{d}\Omega}\right)(\text{section II}) + \\
& \frac{e^2 \omega^2}{4\pi^2 c} \sum_{m=1}^{\infty} \sum_{n=1}^{\infty} \left(\frac{\sin \frac{1}{2} m \langle \beta_z \rangle^{(1)} \nu_m^{(1)}}{\frac{1}{2} m \langle \beta_z \rangle^{(1)} \nu_m^{(1)}}\right) \left(\frac{\sin \frac{1}{2} n \langle \beta_z \rangle^{(2)} \nu_n^{(2)}}{\frac{1}{2} n \langle \beta_z \rangle^{(2)} \nu_n^{(2)}}\right) \\
& \left(\frac{2\pi N_u^{(1)}}{\omega_u}\right) \left(\frac{2\pi N_u^{(2)}}{\omega_u}\right) \sqrt{|S_m^{(\sigma 1)}|^2 + |S_m^{(\pi 1)}|^2} \sqrt{|S_n^{(\sigma 2)}|^2 + |S_n^{(\pi 2)}|^2} \\
& 2\cos\left(\frac{1}{2} m \langle \beta_z \rangle^{(1)} \nu_m^{(1)} - n \langle \beta_z \rangle^{(2)} \nu_n^{(2)} \left(\frac{1}{2} + \frac{N_u^{(1)} + N_{gap}}{N_u^{(2)}}\right)\right),
\end{aligned}
\tag{4.1}
$$

where $N_{gap} = L_{gap}/\lambda_u$ is the length of the fieldfree gap in undulator periods and superscript [1] and [2] refer to values corresponding to the first and second section, respectively. The equation for the spontaneous emission spectrum of a single-section undulator $(\mathrm{d}^2 I/\mathrm{d}\omega \mathrm{d}\Omega)$ (section $\{I, II\}$) is given by Eq. (4.7). The on-axis spontaneous emission for the step-tapered undulator of the free-electron maser with parameters from Table 3.1 is plotted in Fig. 4.1 as a
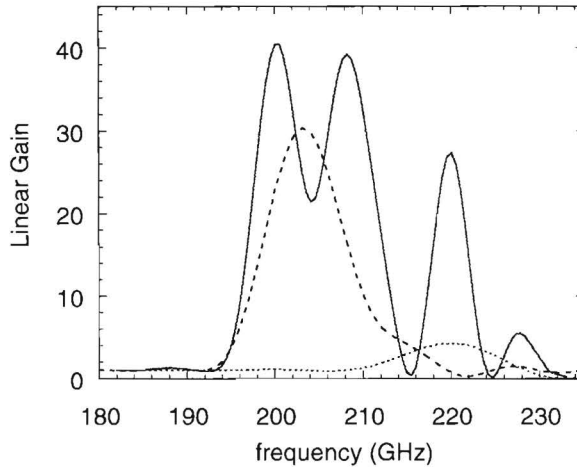
Figure 4.2: *The linear gain as a function of frequency. The solid line is the linear gain of the step-tapered undulator with both sections and an $1\frac{1}{2}\lambda_u$ gap length. The dashed line is the gain curve of the first section acting as a single undulator and the dotted line the one of the second section acting as a single undulator.*

function of the frequency and the gaplength. Only the first harmonic of the spontaneous emission is depicted in the figure. It is concluded that the spontaneous emission spectrum is weakly dependent of the gaplength.

During the first passes, the power in the microwave beam is relatively small and the FEM operates in the small-signal regime. The equations that describe the free-electron laser interaction are basically nonlinear. However, when the radiation field is weak, the electron beam is only little disturbed by the interaction with the radiation field and the equations may be linearised. Then the microwave power at the end of the undulator is proportional to the power of the initial microwave field. The ratio of the output power to the input power in the small-signal regime is called the linear gain. The gain as a function of the frequency in the small-signal regime determines a linear gain curve. Since the gain is linear in the small-signal regime, there the gain resulting from single-frequency calculations must be identical to the gain resulting from a multi-frequency calculation. The linear gain curves of the two sections separately are shown in Fig. 4.2 together with the gain curve of the full system. The dashed line shows the linear gain curve of the first section acting as a single undulator and the dotted line shows the linear gain curve of the second section also acting as a single undulator. The well separated peaks in these linear gain curves have frequencies of 203 GHz and
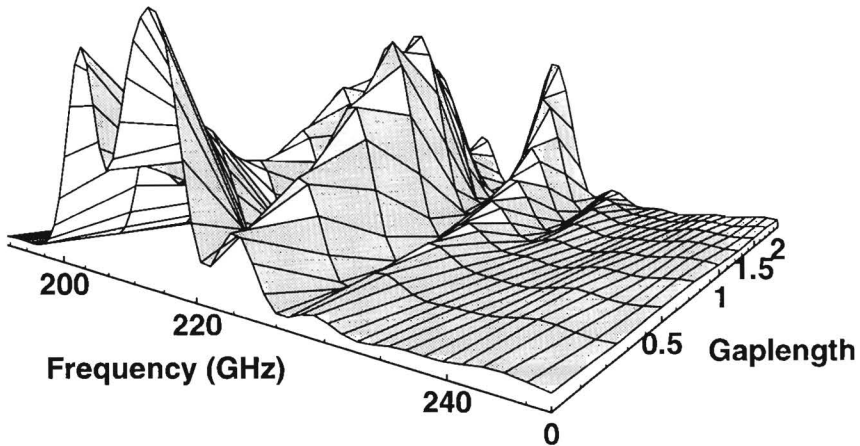
Figure 4.3: *The linear gain of the step-tapered undulator as a function of frequency and gaplength. The gaplength is plotted in units of undulator periods λ_u.*

220 GHz, with values 30 and 4.5 respectively. The actual spectrum of the composite undulator, the solid line in Fig. 4.2, clearly differs from the sum of the spectra of the independent oscillators. This shows that the prebunching of the electrons, as seen by the second section, is a major effect. The two peaks of the gain curve with the lowest frequencies (200 GHz and 208 GHz) result from the peak of the first undulator, modified by the gap and the second undulator. Clearly, in the composite case the gain is enhanced and the peak of the first section is split. The peak at 220 GHz is generated by the second undulator. Its gain is enhanced due to the prebunching of the electrons in the first section. It can be concluded that the step-tapered undulator is not the sum of two separate systems, but operates as a single system with a significant klystron effect [3]. The effect of the gaplength on the linear gain curve is shown in Fig. 4.3. In this figure the gain is plotted as a function of frequency and gap length. The length of the gap is given in undulator periods λ_u. A separate study of the linear gain curve as a function of the gaplength in the absence of space-charge fields and in the 1D, small signal, small-gain regime is presented in Ref. [4].

The FEM operates in the high-gain regime, where the gain is larger than one. Therefore, the results for the small-gain regime do not apply and, for example, Madey's theorem is not applicable to the present case. The latter means that the linear gain curve is not the derivative of the spontaneous emission with respect to the frequency.
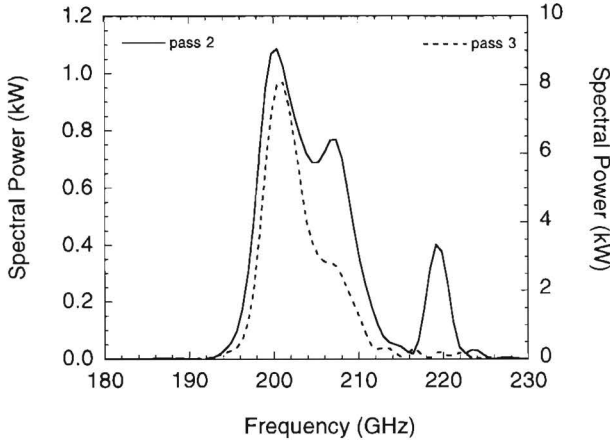
Figure 4.4: *Power spectrum at the end of the second (solid line) and of the third (dashed line) pass.*

4.3 Evolution of the Power Spectrum

From the single pass gain curve one might expect that the spectrum evolves toward a discrete spectrum with three well distinguished lines with about 10 GHz spacing. However, this is not the case as will be discussed in the following. The power spectra at the end of the second and third pass, just before the reflection, are plotted in Fig. 4.4. We will call the 'end of the pass' the longitudinal position just before the reflection at the adjustable mirror (see Fig. 3.3). The interaction region has been passed, but there has not been a full roundtrip from the position where the electrons are injected in the system. Fig. 4.4 shows that the power spectra change drastically during the two passes. At the end of pass two the three peaks in the linear curve of Fig. 4.2 are evidently still present, but the first peak is already dominant over the other peaks. This peak represents the resonance in the first section. One pass later, the microwave field at the resonant frequency of the second section has less gain than the field at the resonant frequency of the first section and, therefore, is relatively suppressed, as is shown by the dashed line in Fig. 4.4.

The system has a high linear gain so that already after a few passes the power in the microwave beam becomes large. At this stage the electrons become strongly bunched and the step-tapered undulator begins to operate as a nonlinear system. In this regime the power is reordered over the spectrum, and the total power starts to level off. These nonlinear effects are already observed after a few passes, well before the power of the stationary state is reached. In this nonlinear phase the bunching of the electrons in the first
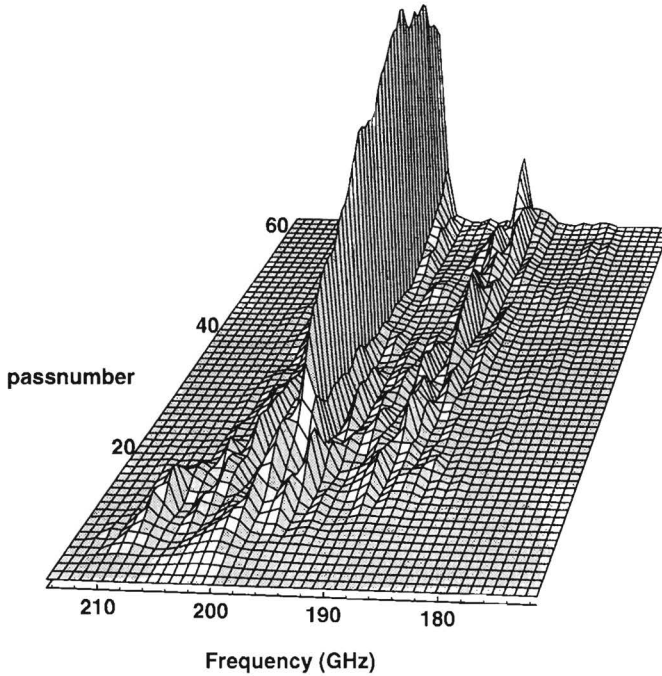
Figure 4.5: *The evolution of the power spectrum during the first 60 passes for a step-tapered undulator with $1\frac{1}{2}\lambda_u$ gap length.*

section is so strong that the second section is an amplifier of the main peak.

The transition from linear to nonlinear interaction between the electrons and microwave beam is presented in Fig. 4.5, where the evolution of the spectrum is shown during the first 60 passes. We mention that the numerical calculation involves the spectral width from 170 GHz to 230 GHz, which is only partial depicted in the figure. We recall that with the adopted reflection coefficient, 71% of the power in each frequency is coupled out per pass. A number of conclusions can be drawn from Fig. 4.5. After about 10 passes, two peaks in the spectrum survive at the positions of the largest peaks in the linear gain spectrum. The power at the position of the resonant frequency of the second section is orders of magnitude smaller. At a certain power level, one main peak grows from a relatively broad power spectrum. The position of this peak corresponds to the resonant frequency of the first section. The higher frequencies that are generated during the first passes are suppressed during the further evolution of the spectrum. This important effect is observed in all cases. During the first twenty passes, the power is transferred to the lower frequencies. This nonlinear process finally results in the gener-
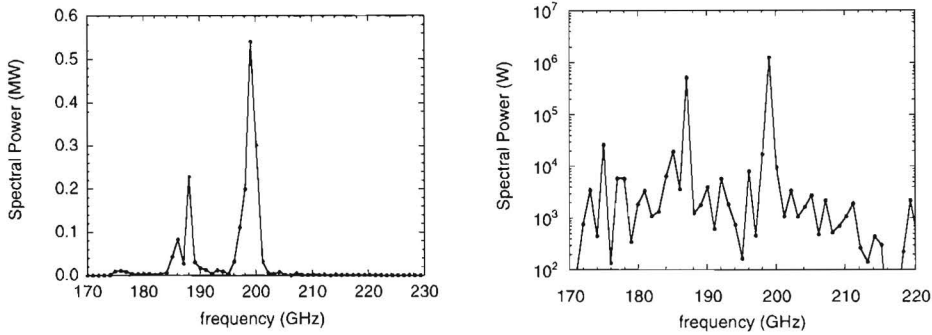
Figure 4.6: *The power spectrum at the end of the 130th pass (Figure on the left) and at the end of the 300th pass (Figure on the right) for a step-tapered undulator with $1\frac{1}{2}\lambda_u$ gap length. Note the logarithmic scale in the latter figure.*

ation of a single, lower frequency sideband. Calculations show that during the following passes the sideband exchanges energy with the main signal.

The profile of the power at the end of the 130th pass is plotted in the figure on the left in Fig. 4.6. At that time the system has acquired a double peaked spectrum with the main peak at 199 GHz and a sideband at 188 GHz. The main peak has 1.2 MW power within a 4 GHz frequency band, while the sideband has 0.4 MW power within a 5 GHz frequency band. These peaks continue to narrow in frequency in the following passes.

After 200 passes, the system enters a regime, where the spectral structure of the millimeter wave beam stays stable in the sense that the power in the frequency-spectrum at the end of each pass does not change during at least the next 200 passes. To this regime we will refer as the stable regime. The spectral power at the end of the 300th pass is plotted in the figure on the right in Fig 4.6. The main peak of the spectrum has a power of 1.3 MW contained within an 1 GHz frequency band. The corresponding sideband is generated at 187 GHz and has a power of 0.5 MW within an 1 GHz band. The total power, i.e. the sum of the power in all frequencies, is 1.92 MW, of which 68% in the main peak and 26% in the sideband. The remaining 6% of the total power is in other frequencies, mainly at the lower frequency side of the main peak.

It is illustrative to compare the previous case with the case where only the first section of the step-tapered undulator is present. The evolution of the spectrum during the first 150 passes is plotted in Fig. 4.7. The figure shows that the system evolves quickly into a stable regime. The main peak is of course determined by the resonance condition and a quite large and well
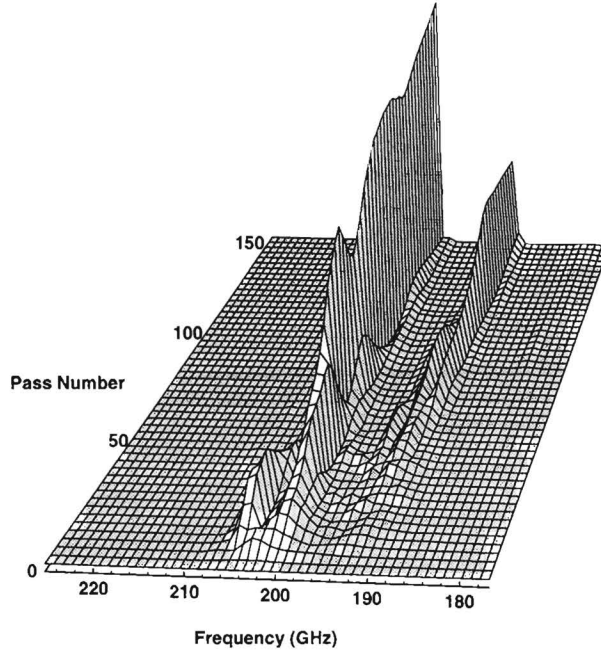
Figure 4.7: *The evolution of the power spectrum during the first 150 passes. The undulator consists of only the first section of the FEM.*

separated sideband is present. Also in this case sideband generation occurs only at the lower frequency side of the main peak. At the end of pass 150, the power of the main peak at 201 GHz is 0.85 MW within an 1 GHz frequency band. The sideband at 190 GHz has a power of 0.3 MW within an 1 GHz frequency band.

It is evident that although their time history is different, the spectrum of the single undulator (Fig. 4.7) is marginally different from the spectrum of the step-tapered undulator (the right figure in Fig. 4.6). However, their power distributions are different. This illustrates again that the second section acts like an amplifier. The spectrum generated by the step-tapered undulator contains more power because amplification of the second section enhances both the power in the main signal and in the sideband. The gain in the stable regime of the main signal and the sideband are compared in the first and second section separately. The gain in the first section is 5 to 20 times larger so this section dominates the spectral distribution. In the first section the gain of the main signal is larger than the gain of the sideband, while in the second section the gain of the sideband is larger than the gain of the main signal.
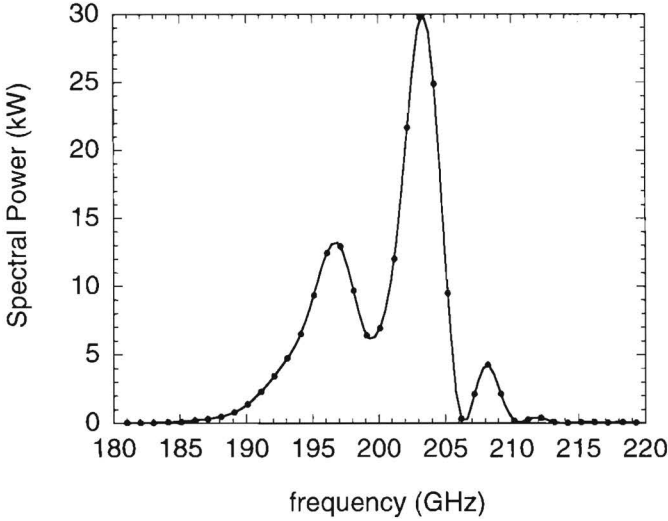
Figure 4.8: *Power spectrum of a single section undulator. The undulator has 30 periods and its parameters are the same as those of the first section of the FEM as given in Table 3.1.*

The sideband corresponds to a nonlinear resonance in the system. This resonance is due to the oscillation of the electrons in the potential well generated by the nonlinear interaction between the electrons and the microwave beam. The position of the sideband in the spectrum can be estimated analytically by assuming a monochromatic maser field a_s and a stationary electron distribution. The sideband is then incorporated as a perturbation. When the initial electron distribution is peaked at the bottom of the stable phase space area (see Chapter 2), the deeply trapped electrons bounce in the ponderomotive potential with frequency Ω_{syn}. This gives rise to sideband-growth [5, 6]. When applying the resonance condition for a low energy electron beam, one finds that the position of the sideband is approximately given by

$$\Delta k \simeq \pm \frac{(k_{z0} + k_u)\, \Omega_{syn}}{k_u}\, \frac{\Omega_{syn}}{c} \simeq \pm \frac{2(k_{z0} + k_u)}{\beta_z \sqrt{1 + a_u^2}} \sqrt{a_u a_s}, \qquad (4.2)$$

where a_u is the normalised undulator field and a_s is the monochromatic maser field of the main peak with wavenumber k_{z0}.

Multi-frequency calculations are performed for a somewhat longer single-section undulator than used in the calculations in Fig. 4.7. The undulator has the same parameters as the first section in the FEM, but here 30 undulator periods are taken in order to get overbunching faster. Therefore, the sideband

behaviour is shown more pronounced. The other parameters are the same as in the previous cases. The spectral power of the microwave field after the third pass is plotted in Fig. 4.8. Two sidebands are generated next to a main peak. The estimate for the position of the sidebands, given by Eq. (4.2), is $\Delta\nu \simeq \pm 5\,\text{GHz}$, which agrees with the positions in the figure. Obviously, the growth rates of the sidebands plotted in Fig. 4.8 are rather different.

Returning to Figs. 4.5, 4.6, and 4.7, the most striking result is that the sideband only grows at frequencies lower than the frequency of the main peak. The estimate for the frequency shift of the sideband, given by Eq. (4.2), is very close to the observed values in these Figures. This is remarkable, since this estimate is obtained from the argument that the electrons perform several synchrotron oscillations in the potential well. Since the electrons perform about half a synchrotron oscillation during their pass through the undulator, the frequency shift is based on qualitative arguments.

We will now give a tentative explanation why only the lower frequency sideband is present without having to take rude assumptions. Usually, these assumptions are infinite undulators, the low-gain limit, the Compton limit and treating the sideband as a small perturbation. Obviously, these assumptions are strongly violated in the present case of the FEM. When the FEM saturates, the electrons have performed about half a synchrotron oscillation in the ponderomotive well. The lower-frequency sideband has lower resonant energy than the one of the main frequency component and can still extract energy from the electrons that are at the bottom of the well of the main mode. The opposite holds for the higher-frequency sideband, that has higher resonant energy. This is schematically depicted in the left figure in Fig. 4.9. Two separatrices are depicted, one of the main component and the other of the lower-frequency sideband. It is obvious that the phase-space is more complicated than is depicted on the left in Fig. 4.9. A more realistic figure of the phase space is depicted in Fig. 2.6.

The generation of the lower-frequency sideband is also explained in the presence of slippage of the electrons with respect to the microwave field [7]. The microwave field, that consists of a main frequency component and a lower-frequency sideband has a field strength as is indicated in the right figure in Fig. 4.9. Due to the sideband, the field is amplitude and frequency modulated. For a lower-frequency sideband, the frequency in the peaks of the field envelope is lower than in the troughs of the field envelope. Electrons entering the undulator at the position corresponding to a trough in the field envelope, emit radiation and slip toward the peak in the field envelope. During this slippage, the frequency decreases and the electrons will stay (more or less) in resonance and emit more radiation than they would emit in the case that no sidebands were present. For electrons starting near the peak
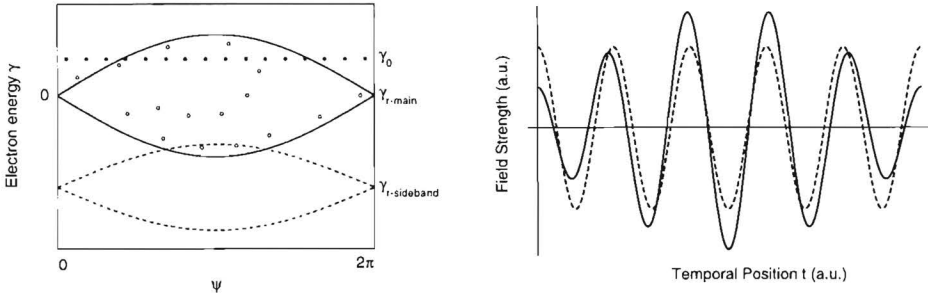
Figure 4.9: *On the left, a schematic plot of the phase-space is given. The solid line corresponds to the separatrix of the main frequency component and the dashed line to the one of the lower-frequency sideband. On the right, the field strength is plotted. Its amplitude and frequency are modulated by a lower-frequency sideband that has $\frac{1}{4}$ of the power of the main mode. The single-frequency reference signal of the main mode is depicted by the dashed line.*

in the field envelope, the opposite holds: when they slip toward the trough in the field, they experience an increasing frequency and therefore will emit less radiation in the higher frequency region than they would do without sideband. The effect of frequency modulated fields is that the amplitude grows in regions with lower frequency and decreases in regions with higher frequencies. This leads to the generation of the lower frequency sideband and to the suppression of field components with higher frequency. The latter occurs since the higher-frequency sideband modulates the field strength such that the frequency is higher in the peaks of the field envelope and lower in the troughs.

4.4 Suppressing the Lower Sideband

An ideal FEM would operate such that all power is confined in a narrow frequency band. Results presented in the previous Section have shown that the spectrum involves a sideband, which amplification may lead to an undesired transfer of energy. Therefore, in this Section possible means of suppressing this lower sideband will be investigated. The output power and its distribution over the spectrum is scanned as a function of the value of the reflection coefficient, its profile, the gap length and the relative polarisation of the undulator sections.
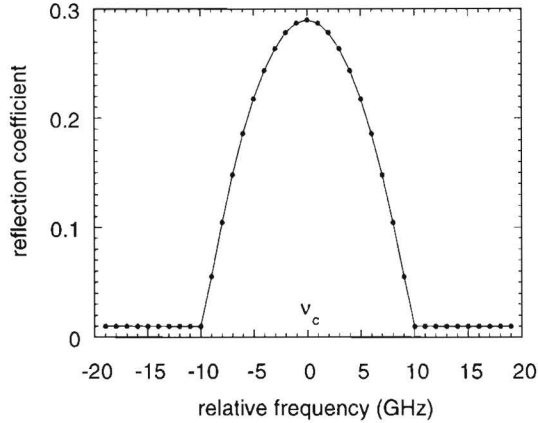
Figure 4.10: *Model for the profile of the reflection coefficient of the FEM. The centre of the curve is at ν_c, which can be chosen freely. The dots represent the $2l$ frequencies of the Fourier modes.*

4.4.1   Wavelength Selective Reflection

In the present design of the FEM, the reflection coefficient is frequency dependent, with a half width in frequency of approximately 7 GHz. The position of the maximum of the profile is variable. We model this profile by a parabolic shape shown in Fig. 4.10.

This profile is used to calculate the evolution of the spectrum for a step-tapered undulator with $1\frac{1}{2}\lambda_u$ gap length. On the basis of previous results (Fig. 4.6), the maximum value of the reflection coefficient is chosen to be at $\nu_c = 199$ GHz. The power spectrum at the end of the 100th pass is plotted in Fig. 4.11. At this stage the system is in the stable regime, which is reached much faster than in the case of a constant reflection coefficient. Due to the narrow profile of the reflection coefficient the sideband is suppressed. Compared to the results in Fig. 4.6, the peak in the power distribution is slightly shifted towards higher frequencies. When the centre of the reflection coefficient (Fig. 4.10) is situated at different positions in the spectrum, the sideband can be more or less suppressed.

An important drawback of the suppression of the sideband by means of a frequency selective reflection coefficient is the drop in power of the main peak. In the case of Fig. 4.11, the total power is only 0.9 MW, while in the case represented in the figure on the right in Fig. 4.6, the total power is 1.9 MW with 1.3 MW in the main peak. Hence, not only the power in the main peak, but also the efficiency decreases considerably. It can be concluded that the nonlinear interaction is such that the presence of a sideband enhances the
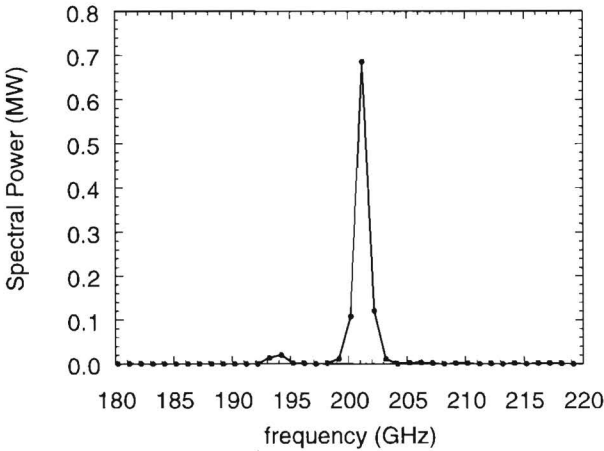
Figure 4.11: *Power spectrum after the 100th pass for a gap length of* $1\frac{1}{2}\lambda_u$ *and the profile of the reflection coefficient. The maximum of the reflection coefficient curve is at 199 GHz.*

power in the fundamental mode. Calculations with other maximum values for the peak value of the reflection coefficient in the range from .2 to .4 show that the total power in the steady state regime changes by not more than 10%. The history of the stable regime depends strongly on the reflection coefficient, but the final power that is reached is about the same.

A tentative physical model explaining the reduction in power of the main peak is the following: analysis shows that in the case of a suppressed sideband, the electrons are overbunched at the end of the first section. Because of this suppression the electrons are not able to cascade into the trapping well at the (lower) resonance energy of the second section. Consequently, at the beginning of the second section the electrons are too far in energy from the trapping well corresponding to the second section and, therefore, the amplification of the microwave field in the second section is smaller in the steady state, which has been observed in the numerical simulations.

In this perspective, the sideband at the lower frequency-side of the main peak can strongly enhance both the total output power as the power of the main peak. This sideband has a lower resonant energy and acts as an intermediate: it serves as a connecting region in phase space between the trapping well of the first section and the lower energy trapping well of the second section, providing a proper electron energy cascade throughout the step-tapered undulator.

4.4.2   Variation of the Reflection Coefficient

We have also investigated cases in which the reflection coefficient is either very large or very small. The profiles of the reflection coefficient are frequency independent and the gaplength is fixed at $1\frac{1}{2}\lambda_u$

The first section is considered as an independent undulator in two extreme cases. In the case that the reflection coefficient is small, 0.05, the main peak in the spectrum at 203 GHz develops rather slowly. The power saturates around 500 kW at the 300th pass. No sideband is developed. In the second case, the reflection coefficient is large, 0.9. Then the generated spectrum becomes broad. This broadening occurs mainly at lower frequencies than the resonant frequency.

Table 4.1 summarises the results for the step-tapered undulator for a number of reflection coefficients. We find that increasing the reflection coefficient enlarges the power in the stable regime in the main peak as well as in the sideband. The higher frequencies are still suppressed. In all cases of Table 4.1, a large main peak is generated together with a large sideband at the position given by Eq. (4.2). For the reflection coefficient of 0.32 the total spectral power is 2.1 MW and the corresponding electron efficiency is 6.9%. At the end of the first section 5.2% of the initial electron energy is transferred into microwave energy. The power in the sideband as a percentage of the total power increases with increasing reflection coefficient.

reflection coefficient	main peak power	sideband power
R=0.23	1.15 MW	0.35 MW
R=0.26	1.2 MW	0.4 MW
R=0.29	1.3 MW	0.5 MW
R=0.32	1.37 MW	0.54 MW

Table 4.1: *Power of the main peak the sideband in the steady state regime for different reflection coefficients.*

4.4.3   Variation of the Gap Lengths

In this Section the effect of different gap lengths on the spectrum is investigated. For cases with parameters of Table 3.1 with $r_b = 1$mm and a flat profile of the reflection coefficient, gap lengths of $1\frac{1}{2}\lambda_u$, $1\frac{1}{4}\lambda_u$ and $1\lambda_u$ are considered. It is clear that the linear gain curves depend on the gap length and the corresponding spectra in the nonlinear regime for the various gap lengths are quite diverse.
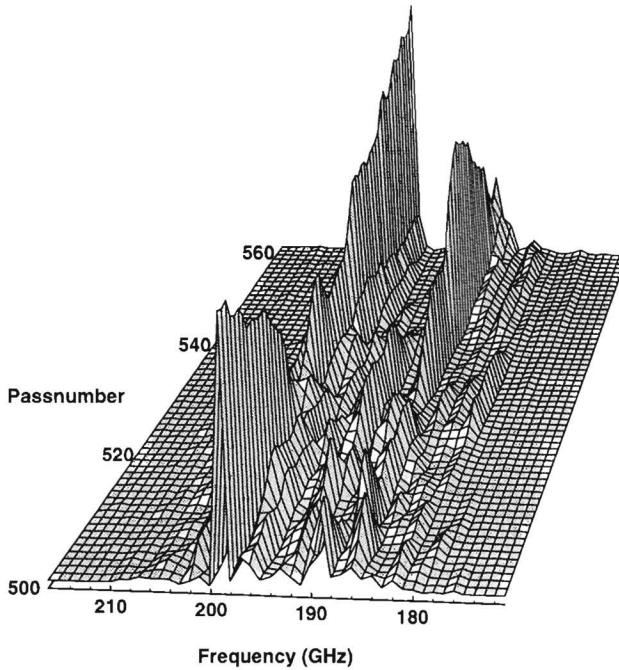
Figure 4.12: *Evolution of the power spectrum during pass 500 to pass 560. The two sections of the undulator are separated by a gap of $1\lambda_u$ length.*

In all cases the frequencies larger than the main frequency are suppressed. The stable regimes in the cases of $1\frac{1}{4}\lambda_u$ and $1\frac{1}{2}\lambda_u$ gap length have the same spectral distributions, which consist of a large main peak and a pronounced sideband. The difference is that the system with a gap length of $1\frac{1}{4}\lambda_u$ reaches the stable regime at higher pass numbers than the system with a gap length of $1\frac{1}{2}\lambda_u$.

In the case of a gap with $1\lambda_u$ length, the evolution of the spectrum, however, is much less smooth than in the other cases: there are more peaks in the spectrum and the power in the various peaks can be larger than the power in the main peak. The power distribution can change considerably over a few passes. This chaotic spectral behaviour is observed already from an early stage and seems to remain chaotic at least to the 1000th pass. As an illustration of the chaotic spectral behaviour, the evolution of the spectrum between pass 500 to pass 560 is plotted in Fig. 4.12. Even in this chaotic case the higher frequencies remain efficiently suppressed, but at the lower frequency side of the main peak strong mode competition occurs and even the power in the main peak can occasionally almost vanish.

4.4.4   Opposite Polarisation of the Second Section

The power spectrum after 150 passes is plotted in Fig. 4.13 for the case where the two undulator sections have the same polarisation. This means that in Eq. (3.2) the sign of B_{u2} is changed. The system is in the stable regime and the microwave power at higher frequencies than the main peak are again efficiently suppressed. As compared to the case indicated in Fig. 4.6, the power in the main peak as well as in the sideband is much smaller.
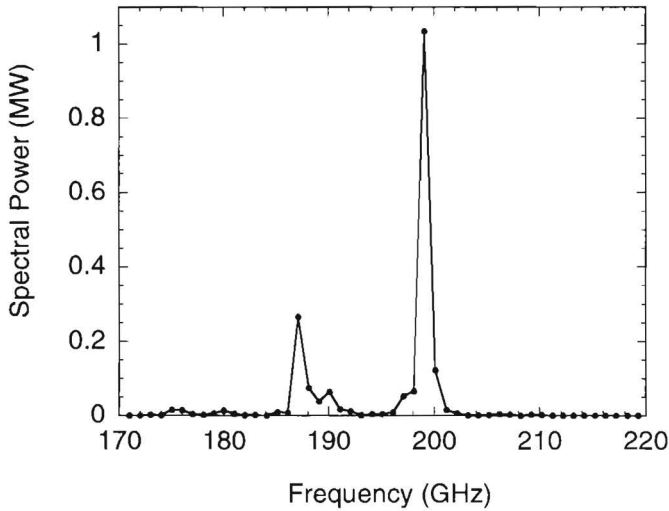

Figure 4.13: *Power spectrum at the end of the 150th pass with a gap of $1\frac{1}{2}\lambda_u$ length and opposite polarisation of the second section.*

4.5   Conclusions

The linear as well as the nonlinear behaviour of the step-tapered undulator and the evolution of its spectrum has been studied. The step-tapered undulator operates as a single system with a significant klystron effect. In most cases, the frequency spectrum evolves into a stable regime, in which it hardly changes from pass to pass. In the stable regime a narrow main peak is generated at the resonant frequency of the first section of the undulator. The major part of the total power is confined in this peak. In all cases that are investigated, the spectral power at the resonant frequency of the second section of the undulator is efficiently suppressed. In the nonlinear regime the first section plays a major role in the evolution of the frequency spectrum and

the second section acts like an amplifier of the radiation field generated in the first section. When the power in the main frequency is sufficiently high, a strong sideband is generated at the lower frequency side of the main peak. The behaviour of the spectrum, in particular the behaviour of the sideband, as a function of the value of the reflection coefficient, its profile, the gap length and the relative polarisation of the undulator sections is investigated. Except for the case with a step-tapered undulator with a gap length of $1\lambda_u$, the sideband is quite narrow, and contains a substantial part of the total RF power. A reflection coefficient with a sufficiently narrow profile will suppress the sideband, but, as a consequence, the power in the main peak will decrease. In the case of a step-tapered undulator with an $1\lambda_u$ gap length, the stable regime is not reached and the spectrum is quite broad. The power is confined in a 20 GHz interval below the resonant frequency of the first section and behaves chaotically.

Appendix A. Spontaneous Emission

In this section, the undulator radiation brightness for the linear undulator is described. The undulator radiation, or spontaneous radiation, is the synchrotron radiation caused by the periodic deflection of the electrons in the undulator. Since the undulator radiation is at virtually the same frequency as the resonant frequency for stimulated interaction, it provides the seed field for the stimulated radiation. The spectral properties of the undulator radiation are derived most easily from the Lienard-Wiechert potentials [9],

$$\frac{\mathrm{d}^2 I}{\mathrm{d}\omega\mathrm{d}\Omega} = \frac{e^2\omega^2}{4\pi^2 c}\left|\int_{-\infty}^{\infty} \boldsymbol{n} \times (\boldsymbol{n} \times \boldsymbol{\beta})\exp\left[\mathrm{i}\omega(t - \boldsymbol{n}\cdot\boldsymbol{r}/c)\right]\mathrm{d}t\right|^2, \tag{4.3}$$

where I_{und} is the far field radiation intensity emitted in the frequency range $d\omega$ and in a solid angle $d\Omega$ around the direction of observation $\boldsymbol{n}$, which in spherical coordinates is given by

$$\boldsymbol{n} = \hat{\mathbf{e}}_x \cos\theta\sin\alpha + \hat{\mathbf{e}}_y \sin\theta\cos\alpha + \hat{\mathbf{e}}_z \cos\alpha. \tag{4.4}$$

Since spontaneous emission is quite weak, the spectrum can be calculated from the unperturbed electron dynamics in the external fields. Betatron oscillations are omitted in the following. The electron dynamics, neglecting terms of $\mathcal{O}(1/\gamma^4)$, is characterised by

$$\boldsymbol{\beta} = \frac{a_u}{\gamma}\cos(\omega_u t)\hat{\mathbf{e}}_x + \left[\beta_{z0} - \frac{a_u^2}{4\beta_{z0}\gamma^2}\cos(2\omega_u t)\right]\hat{\mathbf{e}}_z, \tag{4.5}$$

$$\boldsymbol{r} = \frac{ca_u}{v_{z0}k_u\gamma}\sin(\omega_u t)\hat{\boldsymbol{e}}_x + \left[v_{z0}t - \frac{c^2a_u^2}{8v_{z0}^2k_u\gamma^2}\sin(2\omega_u t)\right]\hat{\boldsymbol{e}}_z, \tag{4.6}$$

where $\omega_u = c\beta_{z0}k_u$ and $\beta_{z0} = v_{z0}/c$. Usually, the spectral brightness is derived for angles smaller than $\alpha \sim 1/\gamma$ and terms of order $\mathcal{O}(1/\gamma^2)$ are neglected. However, in the case of the FEM, the electron energy γ is low. In contrast to the equations in FEL-literature, in the present derivation of the spectral brightness, angles smaller than $\alpha \sim 1/\gamma^2$ around $\alpha = 0$, which is parallel to the z-axis are considered. For these angles, terms of order $\mathcal{O}(1/\gamma^4)$ are neglected. In that case, the spectral brightness is

$$\frac{\mathrm{d}^2 I_{\mathrm{und}}}{\mathrm{d}\omega\mathrm{d}\Omega} = \frac{e^2\omega^2}{4\pi^2 c}\sum_{m=1}^{\infty}|H_m(\nu_m)|^2\left[|S_m^\sigma|^2 + |S_m^\pi|^2\right], \tag{4.7}$$

where the function $H_m(\nu_m)$ is defined as the integral over the interaction region of the oscillating part of the integral,

$$\begin{aligned}
H_m(\nu_m) &= \int_0^{2\pi N_u/\omega_u}\mathrm{d}t\exp\left(-\mathrm{i}m\nu_m\frac{\omega_u}{2\pi N_u}t\right)\\
&= \frac{2\pi N_u}{\omega_u}\frac{\sin\frac{1}{2}m\nu_m}{\frac{1}{2}m\nu_m}\exp\left(-\frac{1}{2}\mathrm{i}m\nu_m\right).
\end{aligned} \tag{4.8}$$

The functions $S_m^{(\sigma,\pi)}$ are defined as

$$\begin{aligned}
S_m^{(\sigma)} &= \beta_{z0}\alpha\cos\theta J_m(mZ,-m\xi)\\
&\quad - \frac{a_u}{\gamma}\left\{J_{m+1}(mZ,-m\xi) + J_{m-1}(mZ,-m\xi)\right\},
\end{aligned} \tag{4.9}$$

$$S_m^{(\pi)} = \beta_{z0}\alpha\sin\theta J_m(mZ,-m\xi), \tag{4.10}$$

where $J_n(x,y)$ is the generalised Bessel function [10]. For large N_u, the spectrum consists of a series of sharp peaks centered at $\omega_m = m\omega_1$. The fundamental frequency ω_1 and the frequency deviation from the mth harmonic ν_m are given by

$$\omega_1 = \frac{\omega_u}{1 - \beta_{z0} + \frac{1}{2}\beta_{z0}\alpha^2}, \qquad \nu_m = 2\pi N_u\frac{m\omega_1 - \omega}{m\omega_1}. \tag{4.11}$$

Note that for $\gamma \gg 1$ the usual approximation for resonant frequency $\omega_1|_{\gamma\gg1} = \omega_u 2\gamma^2/(1 + a_u^2/2 + \gamma^2\alpha^2)$ holds. The frequency dependence of the emitted light is determined by the function $(\sin\nu/\nu)^2$. The spectral width is therefore the same for all harmonics, $\delta\omega \simeq \omega/N_u$. The parameters ξ and Z that have been introduced are,

$$\xi = \frac{a_u^2}{8\beta_{z0}\gamma^2(1 - \beta_{z0} + \frac{1}{2}\beta_{z0}\alpha^2)}, \qquad Z = \frac{a_u\alpha\cos\theta}{\gamma(1 - \beta_{z0} + \frac{1}{2}\beta_{z0}\alpha^2)}. \tag{4.12}$$
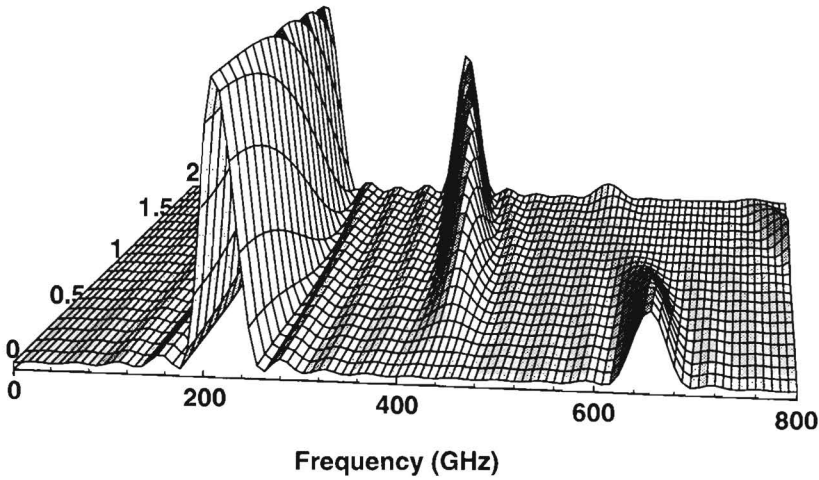
Figure 4.14: *Undulator radiation from a linear undulator with 5 undulator periods. The power at a specific frequency at angle $\gamma^2\alpha$ is plotted. The odd harmonics are emitted on-axis.*

In Fig. 4.14 the brightness produced in an undulator of 5 periods with $a_u = 0.75$ is shown. The energy of the electrons is $\gamma = 4.4$. With these low energies, the usual expressions for the undulator radiation that keep contributions upto $\mathcal{O}(1/\gamma^2)$, are not correct. The equations that are presented here keep contributions upto $\mathcal{O}(1/\gamma^4)$. The first harmonic is at $210\,\text{GHz}$. In the figure also the second and third harmonic are plotted. Only the odd harmonics are emitted on-axis.

The derivation of the spontaneous emission was based upon the emission of a single particle. The effect of the real structure of the electron beam, such as finite energy spread and emittance has not been considered. According to Eq. (4.11), the resonant frequency depends on the electron energy, observation angle and undulator field. Hence, the presence of finite energy spread will lead to line broadening of the emitted radiation. From Eq. (4.11), the frequency shift of an electron moving with energy slightly different from the nominal value can directly be evaluated. For a Gaussian energy distribution with RMS σ_ε, the RMS frequency shift over the electron beam distribution is

$$\left(\frac{\delta\omega}{\omega}\right)_\varepsilon = \frac{1 + \frac{a_u^2}{2}}{\gamma^2\beta_{z0}^2\left(1 - \beta_{z0} + \frac{1}{2}\beta_{z0}\alpha^2\right)}\sigma_\varepsilon, \tag{4.13}$$

neglecting terms of order $\mathcal{O}((\delta\gamma)^2/\gamma^2)$. This will decrease the peak intensity and increase the spectral width of the emitted radiation. The two other sources of inhomogeneous broadening are the natural beam divergence and the transverse dimension of the electron beam. For Gaussian angular and spatial distributions, with RMS values $\sigma_{\alpha_{x,y}}$ and $\sigma_{x,y}$, respectively, the contributions to the inhomogeneous broadening is

$$\left(\frac{\delta\omega}{\omega}\right)_{\alpha_{x,y}} = \frac{\beta_{z0}}{2(1 - \beta_{z0} + \frac{1}{2}\beta_{z0}\alpha^2)}\sigma_{\alpha_{x,y}}^2, \tag{4.14}$$

$$\left(\frac{\delta\omega}{\omega}\right)_{x,y} = \frac{a_u^2}{4\gamma^2\beta_{z0}^2(1 - \beta_{z0} + \frac{1}{2}\beta_{z0}\alpha^2)}k_u^2\sigma_{x,y}^2. \tag{4.15}$$

References of Chapter 4

[1] N.M. Kroll, "Relativistic synchrotron radiation in a medium and its implications for stimulated shock radiation", in *Physics of Quantum Electronics: Free-electron Generators of Coherent Radiation*, Vol. 7 (1980) p. 335.

[2] J.M.J. Madey, "Relationship between mean radiated energy, mean squared energy and spontaneous power spectrum in a power series expansion of equations of motion in a free-electron laser", Nuovo Cimento **50B** (1979) 64.

[3] N.S. Ginzburg and M.I. Petelin, Int. J. Electronics **59** (1985) 291

[4] A.A. Varfolomeev and T.V. Yarovoi, "FEL gain as a function of phase displacement induced by undulator intersection gaps", Nucl. Instrum. Methods A **375** (1996) 352.

[5] N.M. Kroll, P.L. Morton, and M.N. Rosenbluth, IEEE J. Quantum Electron. **QE-17**, 1436 (1981),
M.N. Rosenbluth, H.V. Wong, and B.N. Moore, Phys. Fluids B **2** (7) (1990) 1635.

[6] R.C. Davidson and J.S. Wurtele, "Single-particle analysis of the free-electron laser sideband instability for primary electromagnetic wave with constant phase and slowly varying phase", Phys. Fluids **30** (1987) 557;
R.C. Davidson and J.S. Wurtele, "Influence of untrapped electrons on the sideband instability in a helical wiggler free-electron laser", Phys. Fluids **30** (1987) 2825.

[7] R.W. Warren, J.C. Goldstein, and B.E. Newnam, "Spiking mode operation for a uniform-period wiggler", Nucl. Instrum. Methods A **250** (1986) 19.

[8] M. Caplan, et. al. Nucl. Instrum. Methods A **331** (1993) 243.
A.V. Tulupov, et. al. Nucl. Instrum. Methods A **341** (1994) 305.

[9] J.D. Jackson, *Classical Electrodynamics*, (John Wiley & Sons, Inc.) 1962.

[10] G. Dattoli, L. Giannessi, L. Mezi, and A. Torre, "Theory of generalized Bessel functions", Il Nuovo Cimento B **105** (1990) 327.

Chapter 5

Spectral Dynamics of the FOM Free Electron Maser

Abstract   *In this Chapter we will discuss the actual case of the FOM Free Electron Maser. This FEM is presently under construction at the FOM-Institute for Plasma Physics 'Rijnhuizen' in the Netherlands.*

The nonlinear spectral dynamics is investigated with the numerical code MFF that is described in Chapter 3. The design parameters of the FOM FEM will be used. Space-charge forces are included in the calculations. These forces play a role because the FEM operates in between the high-gain Compton and Raman regime. The fast-oscillating longitudinal space-charge forces counteract the bunching process and the slowly-varying equilibrium space-charge forces enlarge the electron beam radius. The experimentally measured profile of the reflection coefficient is used. The spectral evolution is calculated in the ranges of 130, 200, and 250 GHz. The gaplength is fixed at $1\frac{1}{2}\lambda_u$. It is found that single-peaked power spectra are excited and that the power is emitted in a narrow frequency bandwidth. In order to reach maximum output power, the maximum value of the reflection coefficient should be positioned a few GHz below the frequency corresponding to maximum linear gain. The fast tunability of the operating frequency of the FEM, keeping the profile of the reflection coefficient fixed, is investigated.

5.1   Introduction

In this Chapter the spectral dynamics of the FOM Free Electron Maser (FEM) is investigated. This FEM [1]-[5] is described in Chapter 3 and is under construction at the FOM-Institute for Plasma Physics 'Rijnhuizen' in the Netherlands. We recall that the power of the generated cw microwave field must be at least 1 MW which must be emitted within a small spectral range. The operating frequency is tuneable from 130 to 260 GHz within a minute and over several percent on a much faster timescale. In this Chapter the evolution of the power spectrum is investigated for the FEM with the actual design parameters. These parameters are given in Table 3.1. The length of the fieldfree gap is fixed at $1\frac{1}{2}\lambda_u$ and the experimentally determined profile (Fig. 3.4) for the reflection coefficient is used in the calculations.

The stable, coherent operation in a narrow frequency band is a crucial requirement for the success of the FEM. One dimensional calculations have shown that multimode excitation can be avoided by properly adjusting the system parameters [6, 7]. An important parameter is the length of the field-free gap.

In this Chapter we report about the three-dimensional calculations including all space-charge fields. In Chapter 2 it is discussed that the fast oscillating longitudinal space-charge field modifies the ponderomotive potential such that the electron bunching is counteracted. This results in a lower gain. The DC-space-charge forces that are associated with the equilibrium beam density are included in the calculations. The latter forces lead to a larger electron beam cross-section.

The results, that will be presented in this Chapter are the state-of-the-art predictions of the spectral dynamics of the FOM FEM. The evolution of the power spectrum is investigated in the 130, 200, and 250 GHz regions. In order to operate at these different frequencies, the initial electron energy and the position of the profile of the reflection coefficient must be adapted.

It is shown that the FEM can have stable operation in the entire frequency domain from 130 GHz upto 250 GHz. The stable operation can only be reached when the position of the maximum value of the reflection coefficient is carefully chosen. Over the entire frequency range the microwave field evolves toward a single peaked power spectrum, that couples out more than 1 MW per pass. The power is contained within a maximum frequency range of 4 GHz. The fast tunability is investigated by changing the electron energy over a few percent. In the 200 GHz range, the system can be tuned over a few percent in frequency.
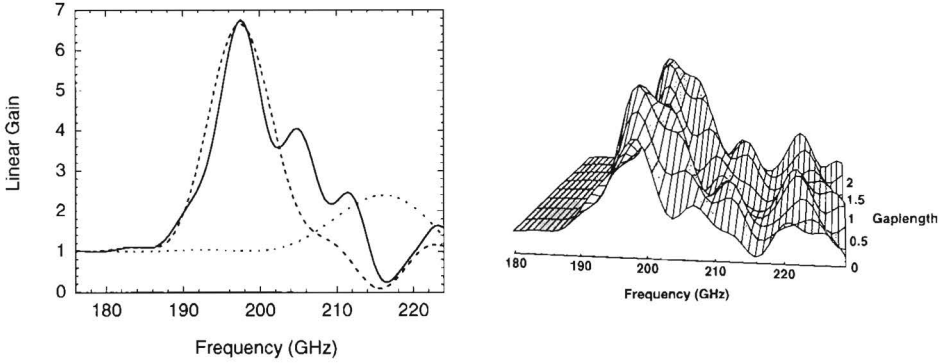
Figure 5.1: *In the figure on the left, the solid line indicates the linear gain curve for the step-tapered undulator and the dashed and dotted lines are the linear gain curves for the first and second section separately, respectively. The electron energy is $\gamma = 4.425$. The result may be compared with Fig. 4.2, where the gain curve is shown disregarding all space-charge forces. In the figure on the right, the gain is shown as a function of the gaplength in λ_u.*

5.2   Gain in the Small-Signal Regime

The (linear) gain of the step-tapered undulator in the small-signal regime as a function of the frequency is shown by the solid line in Fig. 5.1 and the dashed and dotted lines indicate the gain curves for the first and second section separately, respectively. The maxima for these linear gain curves are 6.4 at 198 GHz and 2.4 at 216 GHz, respectively. The initial electron energy is $\gamma = 4.425$. It is verified that the gain curves that are calculated with the multi-frequency code are identical to the gain curves that are obtained from single-frequency calculations. The linear gain curve for the step-tapered undulator has a maximum value of 6.4 at 198 GHz. By comparing Fig. 5.1 and Fig. 4.2, it is shown that space-charge forces reduce the maximum gain from 40 to 6.4 and shift the peak in the gain curve to lower frequencies by 4 GHz.

The initial electron energy is in the range from $\gamma = 3.71$ to $\gamma = 4.912$, in order to operate from 130 GHz to 250 GHz, respectively. In addition, the central frequency of the profile of the reflection coefficient is adapted. The linear gain curves corresponding to these energies are given in Fig. 5.2. In the 130 GHz range, the maximum linear gain is 13.5, which is considerably larger than the one in Fig. 5.1. In the 250 GHz range, the maximum linear gain has dropped to 6.0. The linear gain decreases with increasing operating frequency and it takes more passes to reach high power levels and final saturation.
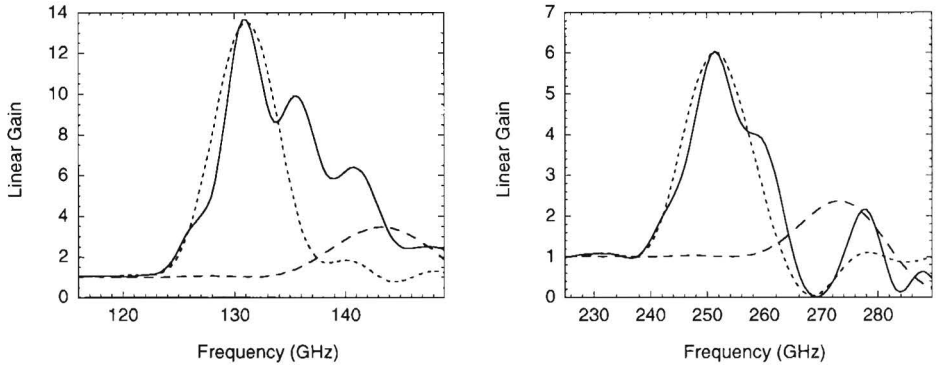
Figure 5.2: *The solid lines indicate the linear gain curves of the step-tapered undulator around 130 GHz and 250 GHz. The initial electron energies are $\gamma = 3.71$ and $\gamma = 4.912$, respectively. The dashed and dotted lines indicate the linear gain curves for the first and second section separately, respectively.*

It is clear that in all cases, the linear gain of the step-tapered undulator differs from the sum of the gain of the separate sections. However, the maximum linear gain is determined by the first section. In a single-section undulator, the electrons remain in the same phase with respect to the ponderomotive potential well. In the field-free gap, the electrons propagate with different velocity than the phase velocity of the microwave field. Therefore, the phase of the electrons in the local potential well in the second section is determined by the length of the gap. The effect of the gaplength on the gain is shown in right figure of Fig. 5.1. In this figure, the linear gain is shown as function of the gaplength that is measured in undulator periods.

5.3   Spectral Evolution

In the small-signal regime, the various frequency components of the microwave field grow independently. The growth rates of the frequency components of the microwave field depend on the linear gain and the reflection coefficient. A peak in the power spectrum grows at the position where the linear gain times the reflection coefficient has a maximum. When the power increases, nonlinear effects become important. These nonlinear effects occur well before saturation. The evolution of the power spectrum is calculated for three values of the electron energy, $\gamma = 3.71$, $\gamma = 4.425$, and $\gamma = 4.912$. The corresponding linear gain curves are plotted in Fig. 5.1 and Fig. 5.2, respectively.

The long term evolution of the power spectra for these cases are depicted

γ	3.71	4.425	4.912
frequency at maximum linear gain	131 GHz	198 GHz	251 GHz
maximum linear gain	13.5	6.4	6.0
operating frequency	131 GHz	195 GHz	246 GHz
saturated power	1.14 MW	1.50 MW	1.58 MW

Table 5.1: *The frequencies of maximum linear gain, the maximum linear gain are given for three values of the initial electron energy γ. The operating frequency to which the microwave field evolves as well as the outcoupled power per pass are give.*

in the upper figures in Fig. 5.3, Fig. 5.4 and Fig. 5.5, respectively. In these figures, the outcoupled power is plotted versus pass number and frequency. In the lower figures, the total integrated outcoupled power is plotted as a function of pass number. Also the outcoupled power at the final pass together with the profile of the reflection coefficient is shown. The position for the frequency with maximum reflection coefficient is in all these cases (roughly) optimised to reach maximum outcoupled power. Note that this maximum and also the generated peak in the power spectrum is downshifted with respect to the frequency corresponding to maximum linear gain.

In all cases, the following evolution of the power spectrum takes place. In the small-signal regime, the microwave power grows with different growth rates for these cases, therefore, starting at the same initial power, the saturated regime is reached at different pass numbers. This is easiest observed in the figures depicting the outcoupled power as a function of pass number. All cases show the tendency that although nonlinear effects are important, a peak is generated at the frequency of maximum linear gain times reflection coefficient. Due to nonlinear processes, in all cases this peak is suppressed in favour of other frequency components. As a consequence, the power spectrum is broadened. During a number of passes mode-competition occurs and a peak in the power spectrum is generated at the frequency component with maximum nonlinear growth. In all cases, this nonlinear peak is at lower frequencies than the frequency of maximum linear growth. This shift in frequency is larger for higher operating frequency. This is summarised in Table 5.1. Due to further nonlinear processes this peaks narrows during the succeeding passes.

The power spectrum in the quasi-stationary regime changes hardly from pass to pass. According to the figures, there is suppression of the components of the microwave field at the resonant frequency of second section right from the beginning. Then, the total outcoupled power per pass is depicted in the
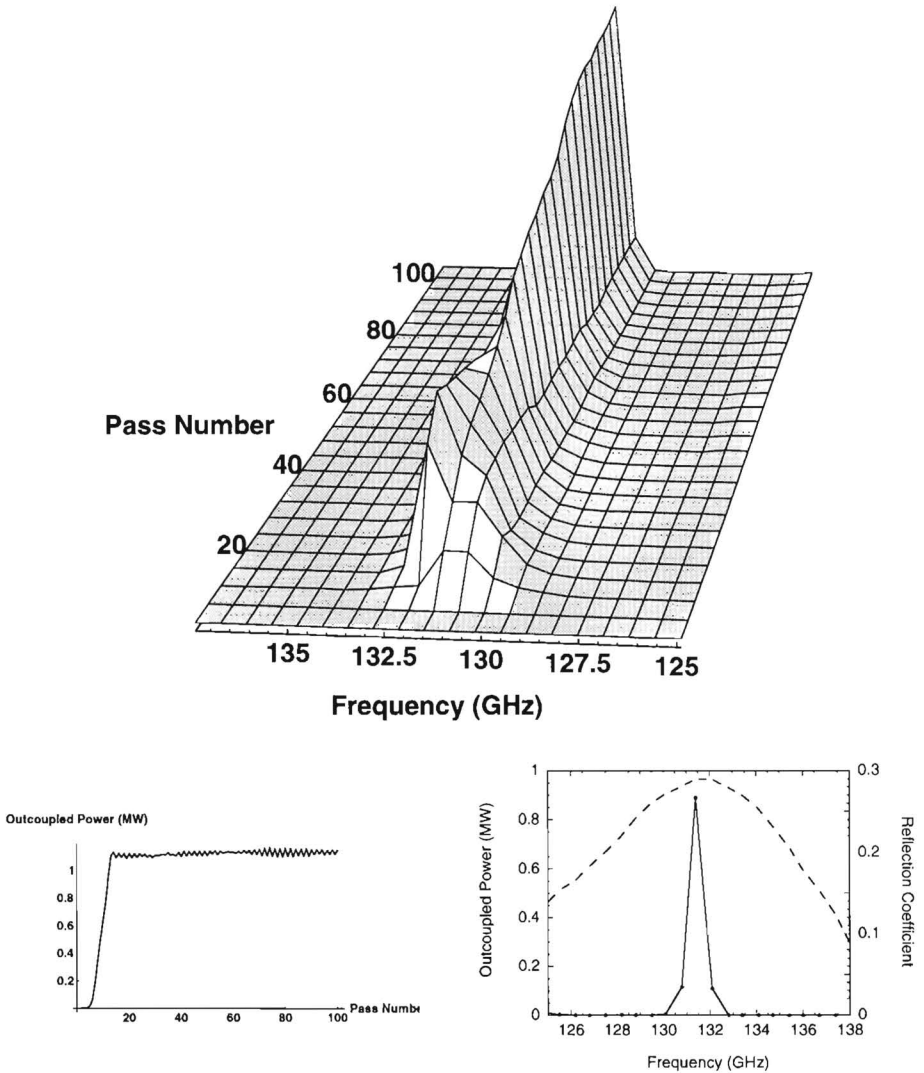
Figure 5.3: In the upper figure the evolution of the power spectrum is shown for operation at 130 GHz during the first 100 passes. The profile of the reflection coefficient is depicted by the dashed line in the lower right figure and the length of the fieldfree gap is $1\frac{1}{2}\lambda_u$. The total outcoupled power is shown in the lower left figure. The outcoupled power as a function of frequency at the end of the 100th pass is shown by the solid line in the lower right figure.

Figure 5.4: *In the upper figure the evolution of the power spectrum is shown for operation at 200 GHz during the first 145 passes. The profile of the reflection coefficient is depicted by the dashed line in the lower right figure and the length of the fieldfree gap is $1\frac{1}{2}\lambda_u$. The total outcoupled power is shown in the lower left figure. The outcoupled power as a function of frequency at the end of the 145th pass is shown by the solid line in the lower right figure.*
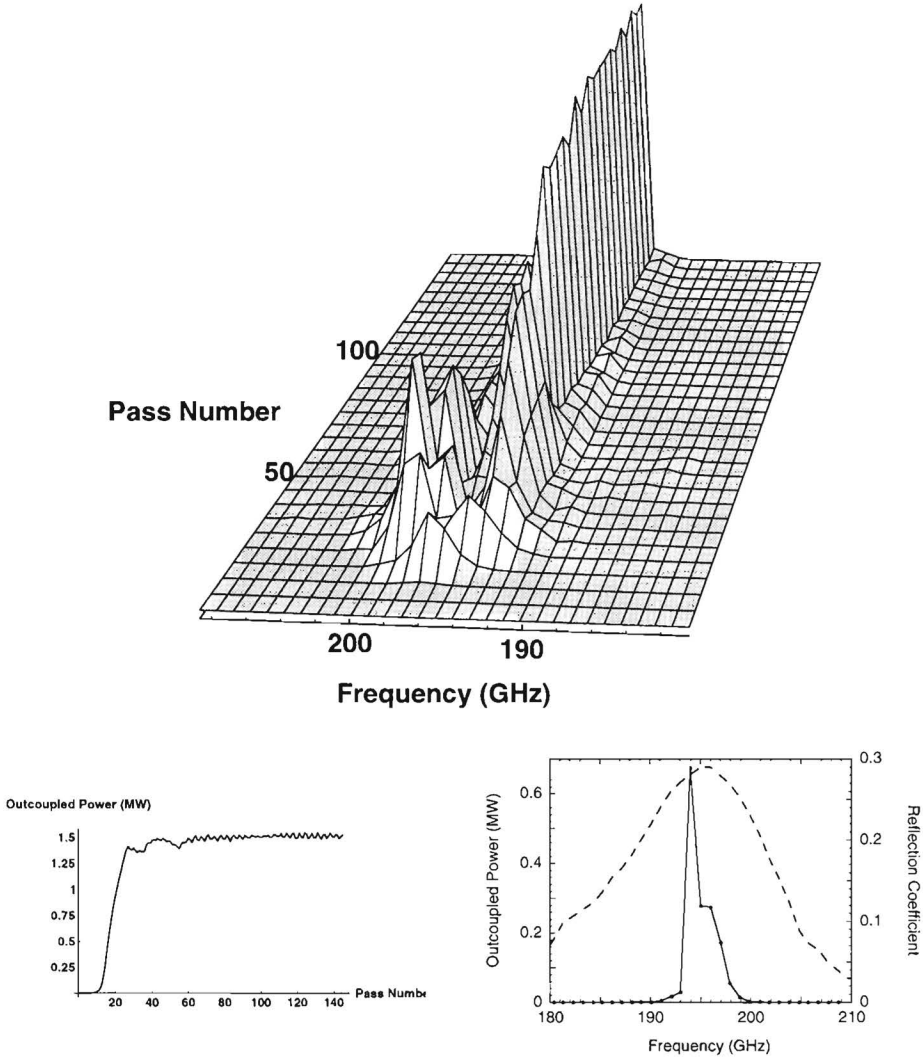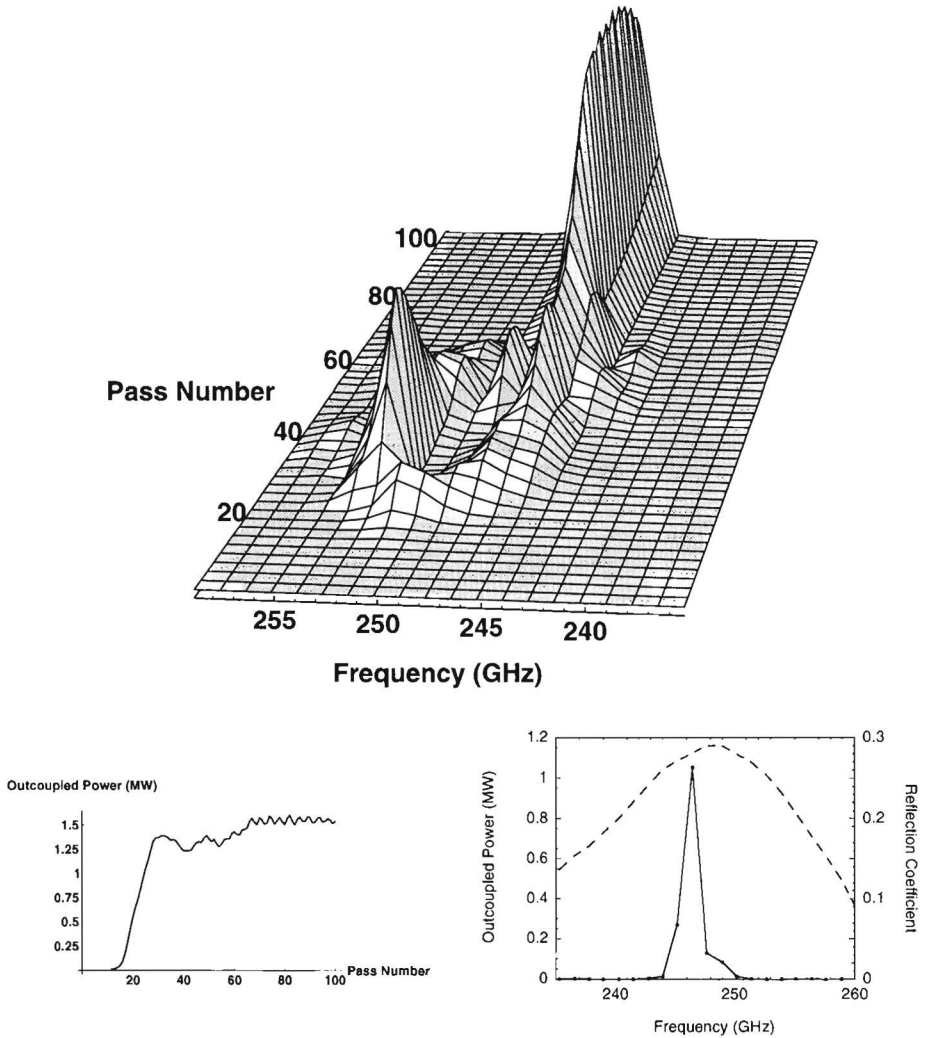
Figure 5.5: *In the upper figure the evolution of the power spectrum is shown for operation at 250 GHz during the first 100 passes. The profile of the reflection coefficient is depicted by the dashed line in the lower right figure and the length of the fieldfree gap is $1\frac{1}{2}\lambda_u$. The total outcoupled power is shown in the lower left figure. The outcoupled power as a function of frequency at the end of the 100th pass is shown by the solid line in the lower right figure.*
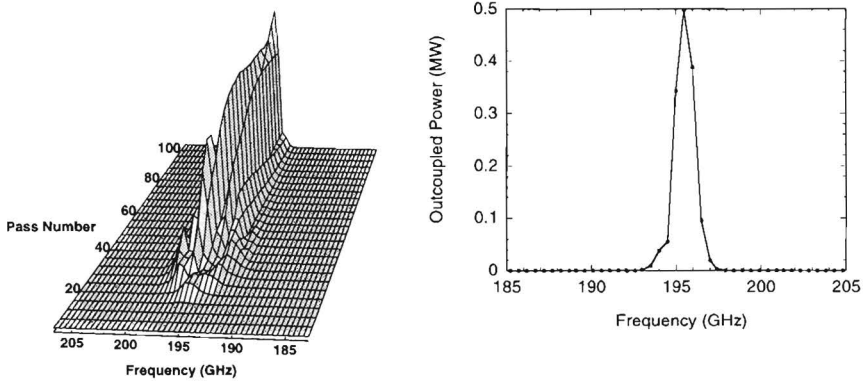
Figure 5.6: *In these figures, the evolution of the power spectrum is shown for half the frequency spacing of the previous cases, i.e. $N = 400$. The evolution must be compared with the evolution that is shown in Fig. 5.4.*

lower right figures of Fig. 5.3, Fig. 5.4, and Fig. 5.5.

For operation at 130 GHz the power spectrum evolves toward a single narrow peak, centered around 131 GHz, that has 1.12 MW within 3 GHz bandwidth. The total outcoupled power is 1.14 MW, therefore 98% of the outcoupled power is contained in the narrow peak. For operation at 200 GHz, the total outcoupled power is 1.5 MW and the peak in the spectrum couples out 1.4 MW per pass within a frequency band of 4 GHz. For operation at 250 GHz the total outcoupled power at the end of the 100th pass is 1.58 MW of which the peak contains 1.53 MW within 4 GHz bandwidth. So, note that the outcoupled power becomes maximal in the final single-peak operation. In all cases considered, the power spectrum remains stable during (at least) the next 50 to 100 passes. In Fig. 5.6, it is shown that the calculations are stable for the choice of N, that determines the spacing between the frequency components. In this figure, the spectral evolution is shown for $\gamma = 4.425$ with frequency spacing that is half of that in Fig. 5.4. The values of N for these figures are $N = 400$ and $N = 200$, respectively. The outcoupled power at the 100th pass is shown on the right in Fig. 5.6. The total outcoupled power is 1.45 MW, of which 1.44 MW is contained within a narrow peak centered around 195 GHz.

We conclude that in the operating regime, $\gamma = 3.71$ to $\gamma = 4.912$, the microwave field evolves toward a stable single-peaked power spectrum if the reflection coefficient is properly adapted. The sideband modes are suppressed. The total outcoupled power is well above the 1 MW. For increasing oper-

ating frequency, the shift between the frequency of maximum linear growth and the final operating frequency increases. This is the reason that it takes more passes for the system to settle down. The increasing shift in frequency between the frequency of maximum linear gain and the final operating frequency increases for increasing frequency contradicts the predictions that are obtained by the analysis of the maximum extraction efficiency in Chapter 2.

5.4   Fast Tuning of the Operation Frequency

In this Section, the tunability of the operating frequency over a few percent is investigated. The maximum value for the profile of the reflection coefficient will be kept fixed and only the electron energy is changed. This is investigated for the $\gamma_0 = 4.425$ (200 GHz) case described in the previous Section. There the outcoupled power was optimised around 195 GHz. In this Section, the electron energy is chosen at $\gamma = \gamma_0 + \Delta\gamma$, where $\Delta\gamma$ is given in Table 5.2. The relationship between $\Delta\gamma$ and the frequency of maximum linear gain is given in Table 5.2. Again, we consider the growth of the radiation from start-up. When $\Delta\gamma = +0.065$, there is no effective amplification of microwave power. In this case, the maximum of the linear gain times reflection coefficient is equal to one. The $\gamma = \gamma_0 - 0.05$, $\gamma = \gamma_0 + 0.05$, $\gamma = \gamma_0 + 0.10$, and $\gamma = \gamma_0 + 0.15$ are given in Fig. 5.7 and Fig. 5.8, where the evolution of the outcoupled power is depicted. Changing the energy $\Delta\gamma$ has the tendency to shift the peak outward the profile of the reflection coefficient. In all cases, the microwave power evolves toward a peak, that may be rather broad but contains reasonable large power. The numbers that correspond to these figures are given in Table 5.2, where for each value of $\Delta\gamma$ the frequency of maximum linear gain, the operating frequency to which the microwave field evolves and the total outcoupled power per pass are given. In addition, in the lower rows the outcoupled power of the peak in the power spectrum and its spectral width are given.

The Table shows that $\Delta\gamma = 0$ is the optimised case. Fast tuning of the frequency of the generated microwave power, without adjusting the profile of the reflection coefficient leads to a large drop in efficiency. With the current profile of the reflection coefficient, a change of the electron energy of $2\frac{1}{2}\%$ leads to a drop in the outcoupled power of 20%. The figures show that for electron energies other than the optimised, it takes longer for the power spectrum to settle down to a narrow power spectrum that couples out high power. The limit on the tunability to higher frequencies is a direct result from the nonlinear shift of the operating frequency in the large-signal regime. Given the electron energy, where the power can grow in the small-signal

Figure 5.7: *The evolution of the power spectrum and the total outcoupled power is shown for the operation at 195 GHz that is shown in Fig. 5.4, but we have changed the initial electron energy γ_0. The left and right figures correspond to electron energies of $\gamma = \gamma_0+0.05$ and $\gamma = \gamma_0-0.05$, respectively.*

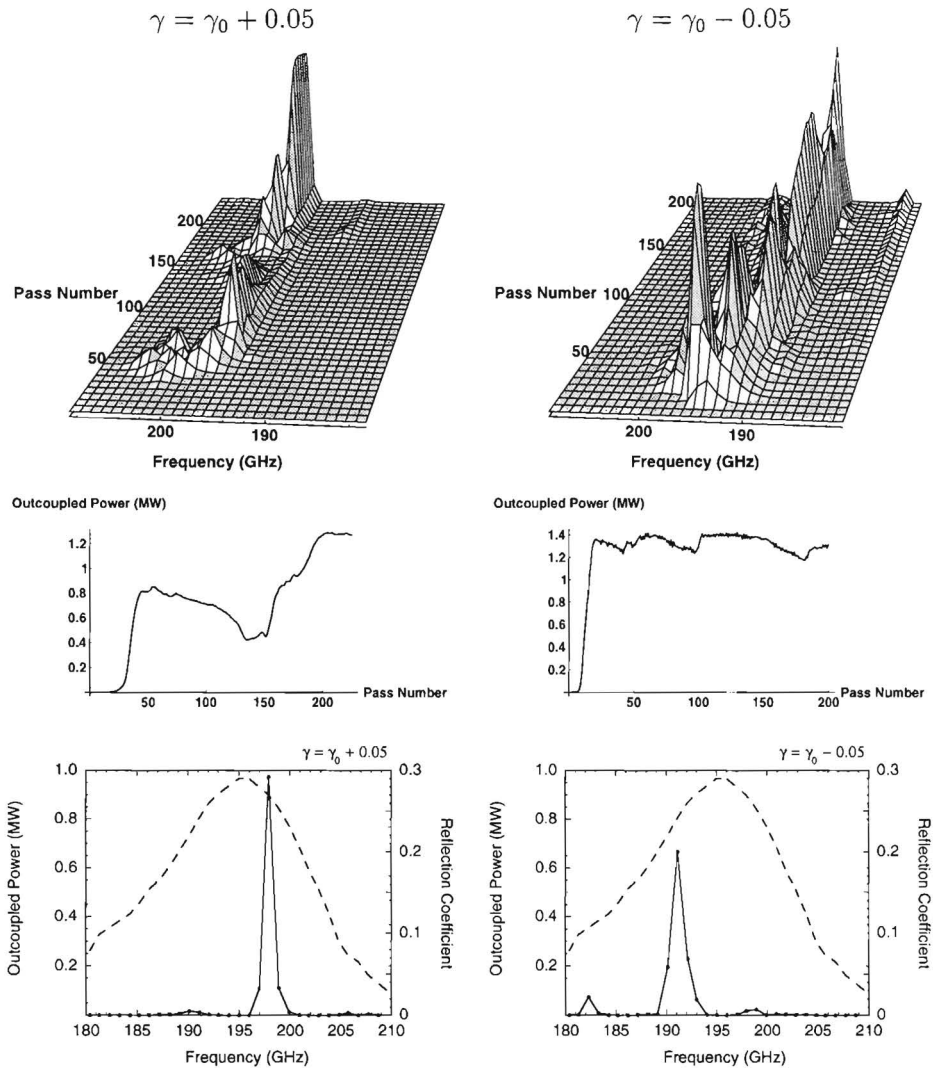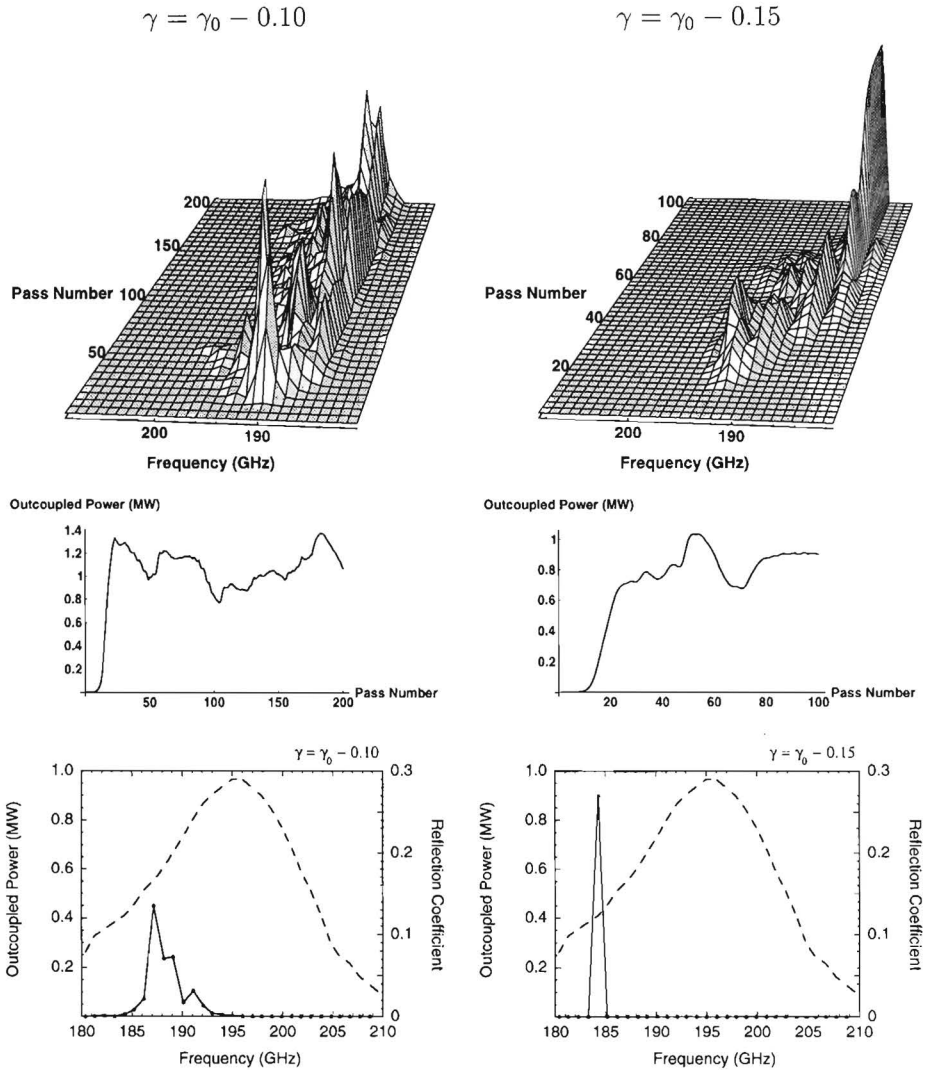$$\gamma = \gamma_0 - 0.10 \qquad\qquad \gamma = \gamma_0 - 0.15$$

Figure 5.8: *The evolution of the power spectrum and the total outcoupled power is shown for the operation at 195 GHz that is shown in Fig. 5.4, but we have changed the initial electron energy γ_0. The left and right figures correspond to electron energies of $\gamma = \gamma_0 - 0.10$ and $\gamma = \gamma_0 - 0.15$, respectively.*

$\Delta\gamma$	+0.05	0	-0.05	-0.10	-0.15
frequency of maximum linear gain (GHz)	203.0	198.5	194.0	189.5	185.0
operating frequency (GHz)	197.9	194.1	191	188.2	184.3
total outcoupled power (MW)	1.27	1.53	1.31	1.28	0.90
outcoupled power in peak (MW)	1.19	1.39	1.15	1.05	0.76
width of the peak (GHz)	3	4	4	5	3

Table 5.2: *The frequencies of maximum linear gain are given for each value of $\Delta\gamma$. The operating frequency to which the microwave field evolves as well as the total outcoupled power per pass are given. The lower rows denote the outcoupled power in the peak in the power spectrum and its spectral width.*

regime, the peak at saturation shifts to lower frequencies. This means that a peak at the higher frequency side of the profile of the reflection coefficient can only be reached when the small-signal regime is circumvented. This can be accomplished by first generating power at lower frequency and then changing the electron energy such that the desired wavelength is reached. However, the corresponding drop in the efficiency is still present.

5.5 The influence of the gap length

The spectral behaviour of the step-tapered undulator depends on the length of the field-free gap between the two sections. This has been studied in Refs. [7]–[8]. The gaplength will in particular influence the role of the second section of the undulator in the interaction. We recall that the length of the gap determines the phase of the electrons in the local potential well of the second section. The immediate effect is a change of the gain in the small-signal regime. The influence of the gaplength is investigated for operation with electron energy $\gamma = 4.424$, i.e. an operating frequency around $200\,\text{GHz}$, and with the profile of the reflection coefficient. The evolution of the power spectrum with gaplength of $1\frac{1}{4}\lambda_u$ and $1\lambda_u$ is shown in Fig. 5.9 and Fig. 5.10, respectively. The evolution may be compared with the evolution in Fig. 5.4. In both cases the total outcoupled power is $1.36\,\text{MW}$ within a narrow spectral bandwidth. The temporal evolution of the power spectrum in these cases is less stable than for a gaplength of $1\frac{1}{2}\lambda_u$ and the final bandwidth of the generated power is broader.
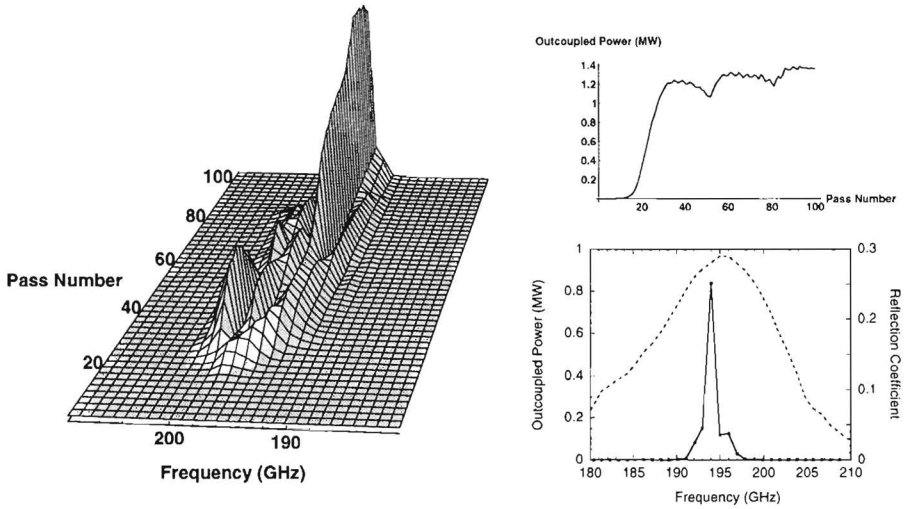
Figure 5.9: *The evolution of the power spectrum is shown on the left with a gaplength of $1\frac{1}{4}\lambda_u$. The frequency dependent reflection coefficient is shown in the lower right figure by the dashed line together with the outcoupled power at the 100th pass. The total outcoupled power as a function of passnumber is shown in the upper right figure.*

Figure 5.10: *The evolution of the power spectrum is shown on the left with a gaplength of $1\lambda_u$. The frequency dependent reflection coefficient is shown in the lower right figure by the dashed line together with the outcoupled power at the 100th pass. The total outcoupled power as a function of passnumber is shown in the upper right figure.*
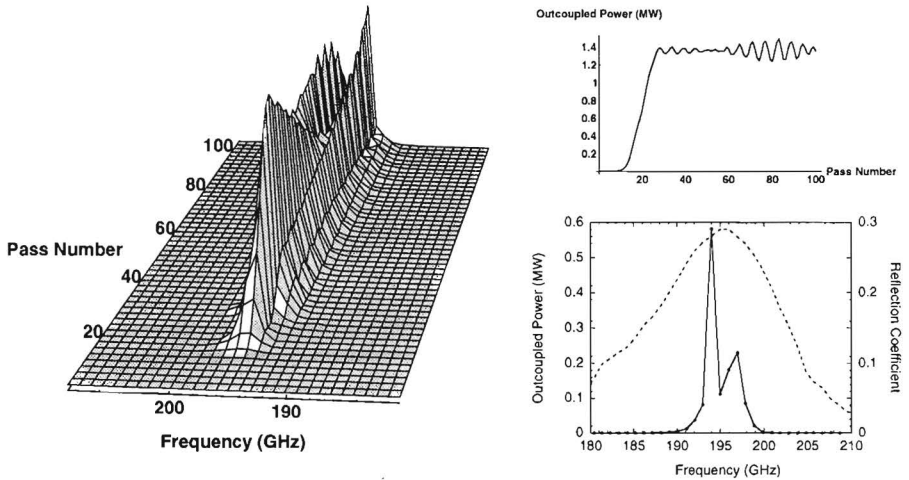
5.6 Conclusions

The calculations that are presented in this Chapter conclusively predict that the FEM has a stable mode of operation, in which power is emitted in a narrow, single-peaked spectrum. The central frequency of the profile of the reflection coefficient must be carefully chosen in order to reach maximum output power and most stable operation. This value is slightly below the frequency corresponding to maximum linear gain. The stable, coherent operation of the FEM is predicted to hold in the entire frequency domain from 130 GHz upto 250 GHz. This frequency range can be reached by solely changing the electron energy and the position of the profile of the reflection coefficient. Over the whole frequency range from 130 GHz to 250 GHz, the microwave power evolves toward a single peaked power spectrum, that couples out more than 1 MW per pass. The power is contained within a maximum frequency range of 4 GHz. It would be excellent when the FEM would meet these predicted results. The fast tunability is investigated. It is found that behaviour of the power spectrum depends critically on the position of the profile of the reflection coefficient. With a fixed position and value of the reflection coefficient, the operating frequency can be changed by adjusting the electron energy. In this way, a shift of operating frequency by $2\frac{1}{2}\%$ leads to a drop in efficiency of 20%.

References of Chapter 5

[1] P.W. van Amersfoort, W.H. Urbanus, A.G.A. Verhoeven, A. Verheul, A.B. Sterk, A.M. van Ingen, and M.J. van der Wiel, "A electrostatic free-electron maser for fusion: design considerations", Nucl. Instrum. Methods A **304** (1991) 168.

[2] W.H. Urbanus, P.W. van Amersfoort, R.W.B. Best, A.B. Sterk, A.G.A. Verhoeven, and M.J. van der Wiel, "A free-electron maser for thermonuclear fusion", Nucl. Instrum. Methods A **318** (1992) 16.

[3] W.H. Urbanus, R.W.B. Best, W.A. Bongers, A.M. van Ingen, P. Manintveld, A.B. Sterk, A.G.A. Verhoeven, and M.J. van der Wiel, "Design of the 1 MW, 200 GHz, FOM fusion FEM", Nucl. Instrum. Methods A **331** (1993) 235.

[4] W.H. Urbanus et. al., "A 130-260 GHz, 1 MW free-electron maser for fusion", Nucl. Instrum. Methods A **358** (1995) 155.

[5] A.G.A. Verhoeven, W.A. Bongers, C.A.J. van der Geer, P. Manintveld, F.C. Schüler, W.H. Urbanus, and M.J. van der Wiel, "A broad-tuneable free electron maser for ECW applications", Proceedings of the ninth joint workshop on electron cyclotron emission and electron cyclotron heating, Borrego Springs, California, (1995) 309.

[6] V.L. Bratman and A.V. Savilov, "Competition of longitudinal modes and the scenario of single-mode regime build-up for the FOM-Fusion-FEM project", Nucl. Instrum. Methods A **358** (1995) 182.

[7] M. Caplan, R.W.B. Best, A.G.A. Verhoeven, M.J. van der Wiel, W.H. Urbanus, V.L. Bratman, and G.G. Denisov, "Predicted performance of a DC beam driven FEM oscillator designed for fusion applications at 200-250 GHz", Nucl. Instrum. Methods A **331** (1993) 243.

[8] P.J. Eecen, A.V. Tulupov, and T.J. Schep, "Spectral dynamics of a high-power, high gain FEM with a step-tapered undulator", Phys. Rev. E. **52** (1995) 5460.

Chapter 6

On the Reflection Coefficient and on the Gap Length

Abstract   *In the previous Chapter, it is found that the fast tunability is limited by the narrow profile for the reflection coefficient. In this Chapter, a frequency independent reflection coefficient is considered and the resulting evolution of the power spectrum is compared with the results of the previous Chapter. It is found that the influence of the shape of the reflection coefficient on the spectral behaviour is quite large. In the present case, the outcoupled power exceeds the 1 MW level and is generated within a broad frequency bandwidth. The power spectra consist of multiple peaks. This behaviour is observed for operation in the entire range from 130 GHz to 250 GHz. The effect of changing the reflection coefficient or the gap length on the spectral dynamics is reported.*

The role of the fast oscillating longitudinal space-charge fields on the spectral dynamics is investigated by comparing the spectral evolution when all space-charge forces are disregarded (see Chapter 4) with the spectral behaviour including only the fast oscillating longitudinal space-charge fields. Since the AC-space-charge forces counteract the bunching process, these forces reduce the gain and stabilise the spectrum. It is shown that the influence of the DC-forces on the spectral behaviour is large by comparing numerical calculations including these DC-forces and disregarding these DC-forces.

6.1   Introduction

In the previous Chapter we predicted that the FOM Free Electron Maser (see Chapter 3) is capable of generating high cw microwave power in the frequency range from 130 GHz to 250 GHz. At least 1 MW of microwave power is generated within a narrow spectral range. The small bandwidth of the generated microwave radiation is, among others, determined by the profile of the reflection coefficient. In the present Chapter, we will investigate the FEM with the parameters that are given in Table 3.1. In contrast to the previous Chapter, here the reflection coefficient is frequency independent.

A broad profile of the reflection coefficient modifies the evolution of the microwave power with respect to the one that is presented in the previous Chapter. The question is whether the power spectrum remains single peaked in the case the reflection profile is broadened. We will show that the power spectrum in the present case strongly differs from those presented in the previous Chapter. This holds in the entire frequency domain between 130 GHz and 250 GHz. Although a narrow main peak in the spectrum is still generated, we will show that sidebands are also generated. These sidebands only appear at frequencies below the frequency of the main peak. The influence of the reflection coefficient and the length of the gap between the two sections of the step-tapered undulator on the spectral behaviour is analysed. As a comparison, the spectral dynamics of the first section operating as a single undulator is investigated. With the single section undulator, the electrons perform less than half a synchrotron oscillation in the potential well and no sideband is generated.

Another issue that is addressed in this Chapter is the influence of the DC-forces on the spectral behaviour. We call the DC-forces the effective equilibrium Lorentz force on the electron beam, which is discussed in Section 2.2.1. The implementation of the DC-forces in the numerical code is discussed in Chapter 3. These forces cause the electron beam radius to be broader on average and cause large oscillations on the beam radius. By comparing the results of calculations where only the fast oscillating space-charge forces are included with the results of Chapter 4, the effects of these fast oscillating space-charge forces on the generated spectrum are investigated. The role of the DC-forces is important as the comparison will show between the results of calculations where only the fast oscillating space-charge forces are included and the results including all space-charge forces.

6.2 Frequency Independent Reflection Coefficient

In this Section, the evolution of the power spectrum is investigated when the FEM is operating with initial electron energies $\gamma = 3.71$, $\gamma = 4.424$, and $\gamma = 4.912$. For these energies, the FEM operates near $130\,\mathrm{GHz}$, $200\,\mathrm{GHz}$, and $250\,\mathrm{GHz}$, respectively. Note that these frequencies have also been considered in Chapter 5. In this Section, we consider a frequency independent reflection coefficient. That way, the evolution of the power spectrum may be quite different. Power may be generated in a broader frequency range, since the profile of the reflection coefficient that is considered in the previous Chapter rapidly decreases from the central frequency. Of course, the gain per pass does not depend on the reflection, however, the gain over many passes is strongly influenced by the magnitude and profile of the reflection coefficient. The linear gain curves of the step-tapered undulator for initial electron energies $\gamma = 3.71$, $\gamma = 4.424$, and $\gamma = 4.912$ are shown in Fig. 5.1 and Fig. 5.2.

For the aforementioned initial electron energies, the evolution of the power spectrum is shown in Fig. 6.1, Fig. 6.2, and Fig. 6.3, respectively. In these figures the outcoupled power (per pass) is shown as a function of frequency and pass number. In the lower left figures the outcoupled power integrated over frequency is plotted and in the lower right figures the outcoupled power at the end of the 200th pass is shown. In all cases, the power spectrum evolves quickly toward a broad spectrum with a dominant peak. In the first phase of the evolution, this peak is at the frequency of maximum linear gain. At a later stage, this peak shifts nonlinearly toward lower frequencies. Upon comparing these results with those presented in Fig. 5.3, Fig. 5.4, and Fig. 5.5, it is seen that the spectral evolution depends quite strongly on the shape of the reflection coefficient.

Although there is heavy mode competition and generation of power over a broad frequency interval, the power at frequencies higher than the main peak are effectively suppressed in all cases. It is seen that in the nonlinear regime, at the onset of overbunching at the end of the first section as well as at the end of the second section, sidebands appear. These sidebands appear on the lower frequency side of the main peak in the spectrum. We recall that overbunching means that the electrons reach the bottom of the potential well before the end of the undulator and start to absorb energy from the microwave field. The electrons perform between one half and a complete synchrotron oscillation in the ponderomotive potential. As soon as the bunches start to absorb energy from the microwave field sidebands appear in the spectrum. The distance
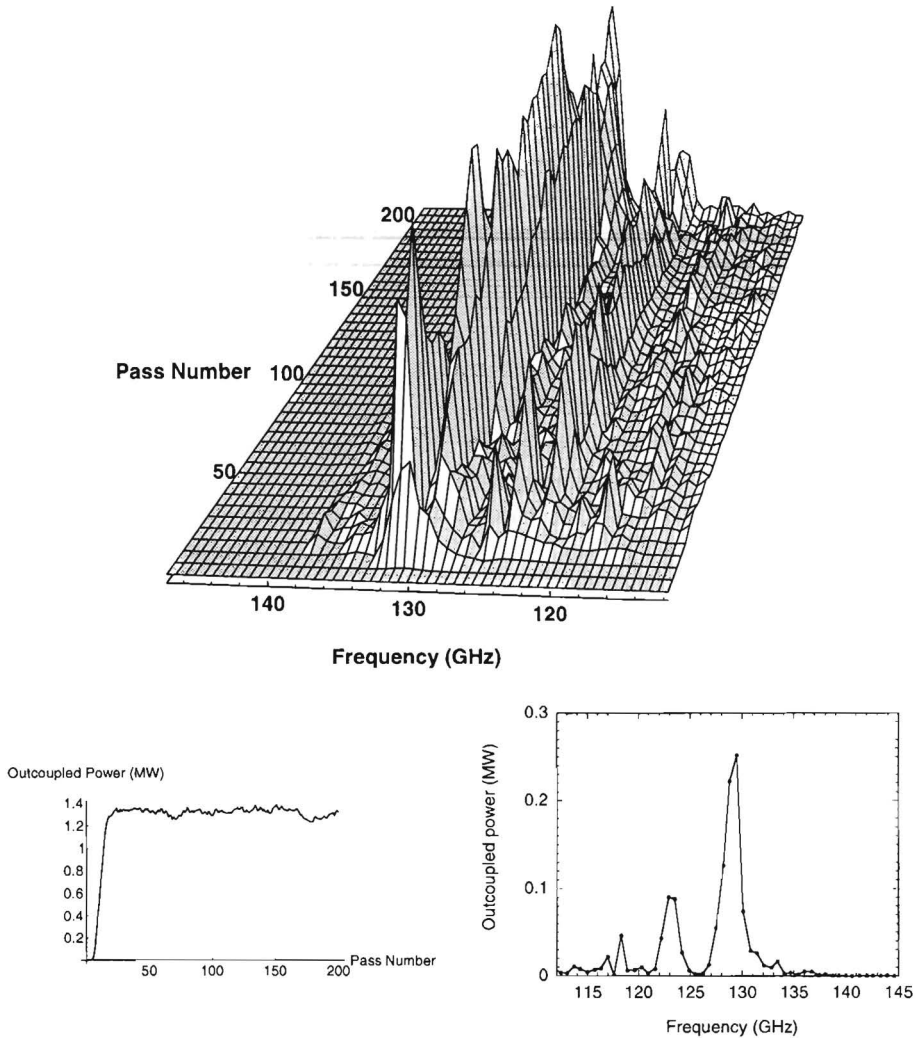
Figure 6.1: The spectral evolution for an electron energy of $\gamma = 3.71$ (130 GHz). The first 200 passes are shown for a step-tapered undulator with $1\frac{1}{2}\lambda_u$ gap length. In the lower left figure the total outcoupled power is plotted as a function of pass number. The outcoupled power as a function of frequency at the end of the 200th pass is shown in the lower right figure.
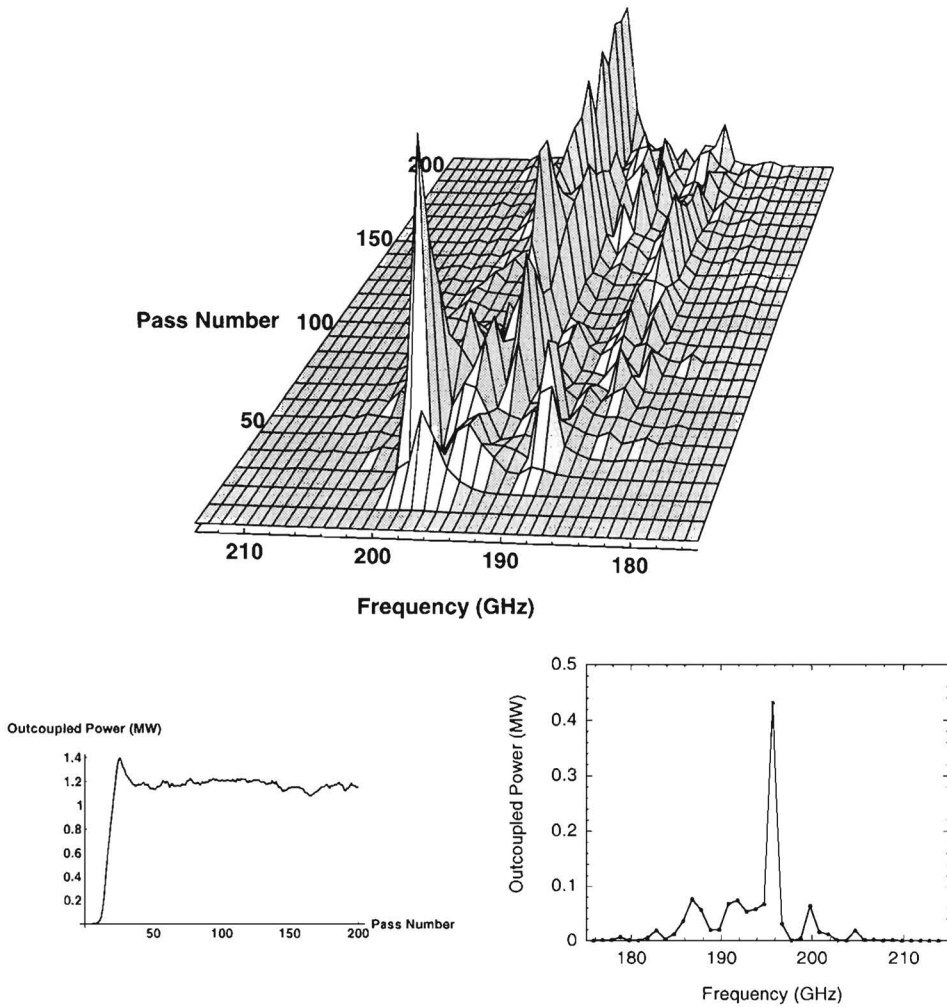
Figure 6.2: *The spectral evolution for an electron energy of* $\gamma = 4.424$ *(200 GHz). The first 200 passes are shown for a step-tapered undulator with* $1\frac{1}{2}\lambda_u$ *gap length. In the lower left figure the total outcoupled power is plotted as a function of pass number. The outcoupled power as a function of frequency at the end of the 200th pass is shown in the lower right figure.*

Figure 6.3: *The spectral evolution for an electron energy of* $\gamma = 4.912$ *(250 GHz). The first 200 passes are shown for a step-tapered undulator with* $1\frac{1}{2}\lambda_u$ *gap length. In the lower left figure the total outcoupled power is plotted as a function of pass number. The outcoupled power as a function of frequency at the end of the 200th pass is shown in the lower right figure.*
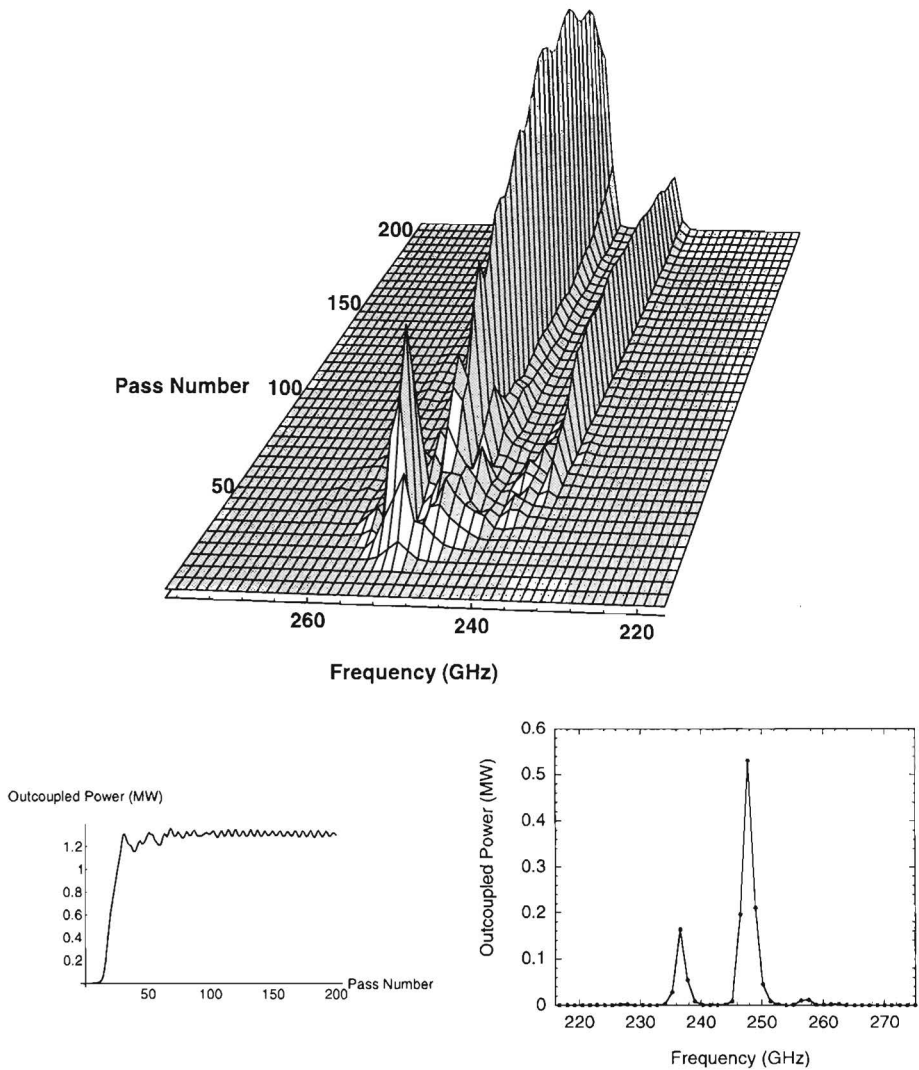
electron energy γ	3.71	4.424	4.912
frequency at maximum linear gain	131 GHz	198 GHz	251 GHz
frequency of main peak	129.5 GHz	195.7,GHz	247.7 GHz
saturated outcoupled power	1.27 MW	1.20 MW	1.30 MW
outcoupled power main peak	0.73 MW	0.55 MW	1.00 MW

Table 6.1: *The frequencies of maximum linear gain, the frequency of the main peak to which the microwave field evolves as well as the total outcoupled power and the outcoupled power in the main peak per pass are given. The numbers that are shown correspond to the Fig. 6.1, Fig. 6.2, and Fig. 6.3.*

in frequency between the main peak and the sideband corresponds to the energy oscillation in the potential well. The higher frequency sideband is energetically unfavourable and is not generated.

The frequency of maximum linear gain, the frequency of the main peak to which the microwave field evolves as well as the total outcoupled power and the outcoupled power in the main peak are given in Table 6.1. When the FEM operates around 130 GHz, the power spectrum keeps fluctuating. An appreciable part of the power is in two sidebands. These peaks are equally spaced at 6 GHz in the spectrum. In literature [1]–[3], the larger peak is attributed to a sideband, while the other is said to be generated by the so-called 'frequency doubling mechanism'. These numerical results in these Refs. are obtained with long undulators, in which the electrons perform many synchrotron oscillations. In the FEM, however, the electrons perform less than a full synchrotron oscillation.

When the FEM operates around 200 GHz, see Fig. 6.2, the spectrum has similar characteristics as for operation around 130 GHz. For operation around 250 GHz, see Fig. 6.3, the power spectrum settles down toward a spectrum that consists of two quasi-stable narrow peaks. Note that during pass 180 to pass 200, the main peak shifts towards a lower frequency. The visual effect of this shift in the figure is that it appears as if the power drops. The sideband follows this behaviour and the frequency spacing between the main peak and the sideband peak is kept constant.

Upon comparing the present results with the results of simulations employing a narrow profile of the reflection coefficient as are shown in Chapter 5, the following observations are made. The power spectrum is slightly less stable and has a multi-peaked spectrum. Also these peaks are broader and the total outcoupled power may be changed. In the 130 GHz case, more power is coupled out as compared to the single-peaked spectrum of Fig. 5.3. For operation around 200 GHz and 250 GHz it is shown that distributing the

spectral power over a wide spectral domain decreases the total outcoupled power by 20% and 15% with respect to the single-peaked spectra of Fig. 5.4 and Fig. 5.5, respectively. The frequencies of the main peak in the power spectrum are about the same. We conclude that the narrow profile of the reflection coefficient stabilises the power spectrum and confines the microwave power within a single peaked spectrum.
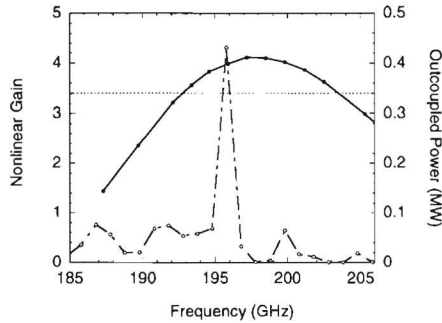

Figure 6.4: *The (nonlinear) gain is indicated by the solid line. The initial power for the microwave field is for all frequency components 0.2 MW. Note that the nonlinear gain is depending on the initial radiation power. The dashed flat line indicates the inverse reflection coefficient. The outcoupled power at the end of the 200th pass is indicated by the dashed line.*

We consider the initial electron energy of $\gamma = 4.424$, i.e. operation around 200 GHz. The solid line in Fig. 6.4 indicates the gain in the large-signal regime, where we have taken as initial power 0.2 MW. In this regime, the gain depends on the initial power of the radiation field. The curve in Fig. 6.4 is pointwise calculated in the single-frequency limit. The maximum in the gain curve is unchanged when the initial power is increased. The horizontal dashed line is the inverse of the reflection coefficient. It is clear that in the single-frequency limit, the microwave field for frequencies that have larger gain than 3.4 saturates at higher power than 0.68 MW (3.4×0.2 MW), and others at lower power. For example, the component at 190 GHz couples out only 4 kW after 10 passes. From Fig. 6.4 it is concluded that the peak in the power spectrum is not at the frequency of maximum linear gain and not at the frequency of maximum nonlinear gain. It has shifted to 1 GHz below the frequency of maximum nonlinear gain. A result that is revealed only by the use of a multi-frequency code. Furthermore, the frequency components at the lower frequencies than 192 GHz would never grow to the present power levels in the single-frequency limit. The power at these frequencies (<192 GHz) only grow because of nonlinear feeding of the main peak.

6.2.1 Single-Section Undulator

The spectral evolution of the microwave field generated by the first section of the undulator alone is represented on the right in Fig. 6.5. The dashed line represents the gain as a function of frequency in the small-signal regime. The linear gain has a maximum of 6.4 at 198 GHz. The total outcoupled power per pass grows quickly to a maximum around pass 40. Then the outcoupled power is 0.70 MW per pass and remains unchanged. The power spectrum narrows toward a peak positioned at the frequency of maximum linear gain. This process continues in time. The electrons do not overbunch and no sideband is generated. The outcoupled power at the end of the 150th pass is indicated by the solid line. Almost all power is in the main peak. The efficiency, i.e. the ratio of generated power over initial power of the electrons, is 2.75% at saturation. This value is close to the estimated value in Section 2.3.2.
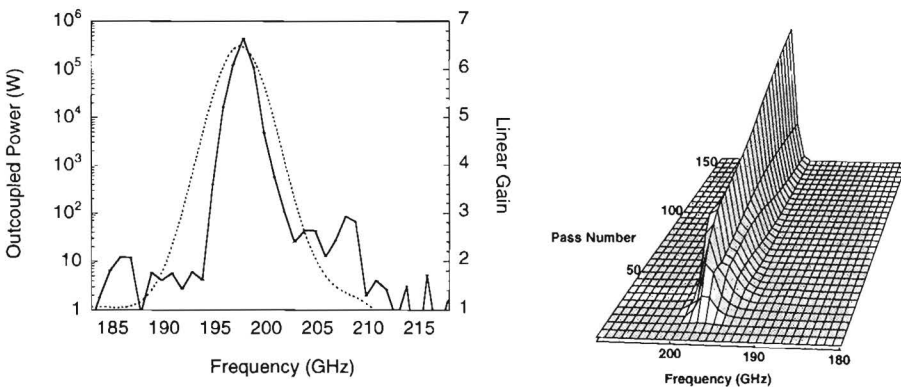

Figure 6.5: *In the figure on the left, the linear gain curve of the first section acting as a undulator is indicated by the dashed line. The outcoupled power after 150 roundtrips is indicated by the solid line. In the figure on the right, the outcoupled power per pass during the first 150 roundtrips is plotted.*

Also in the case of a single section undulator, upon comparing Fig. 6.5 and Fig. 4.8, it is concluded that the space-charge fields reduce the gain. In the case the space-charge forces are disregarded (Fig. 4.8), the electrons overbunch at the end of the undulator and a large sideband is generated. On the other hand, adding the second section, see Fig. 6.2, also increases the gain with the result that the power spectrum is less stable and a sideband is generated.
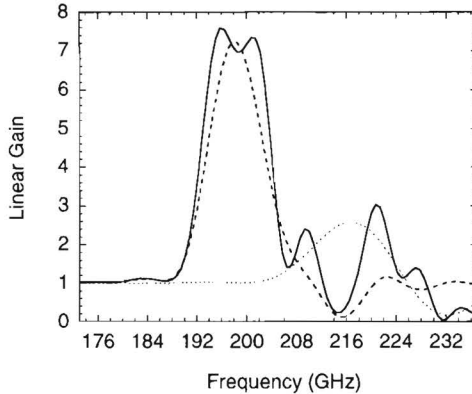
Figure 6.6: *The solid line is the linear gain curve of the step-tapered undulator. The dashed and dotted lines are the linear gain curves for the first and second section separately, respectively.*

6.3   The influence of DC-forces

In this Section, we present results of simulations disregarding the DC-forces in the case of a frequency-independent profile of the reflection coefficient. What we call DC-forces are the effective equilibrium Lorentz forces as are described in Section 2.2.1. These radial forces play no direct role in the generation of the ponderomotive well. However, indirectly they do influence the interaction because the betatron oscillation and the radius of the electron beam are modified. Since in the presence of these DC-forces the electron beam is on average larger, the radius of the electron beam is chosen to be smaller, 0.92 mm. The effect of the DC-forces on the electron beam radius and the betatron oscillation is shown in Fig. 2.1.

The solid line in Fig 6.6 is the linear gain curve in the absence of DC-forces. The dashed and dotted lines are the linear gain curves for the first and second section separately, respectively. The main peak is dominated by the first section. As compared to the linear gain curve where also the fast oscillating space-charge fields are disregarded, see Fig. 4.2, the gain has dropped from 40 to 7.5. As compared with the linear gain curve including the DC-forces (see Fig. 5.1), the maximum linear gain is a little larger.

The temporal evolution of the power spectrum is shown in Fig. 6.7. The outcoupled power at the end of each pass is plotted from pass 10 to 90. Because of the high linear gain, the system quickly reaches high power levels. The power spectrum of the microwave beam evolves towards a single, pronounced peak. At the end of the 90th pass, this peak couples out 1.0 MW
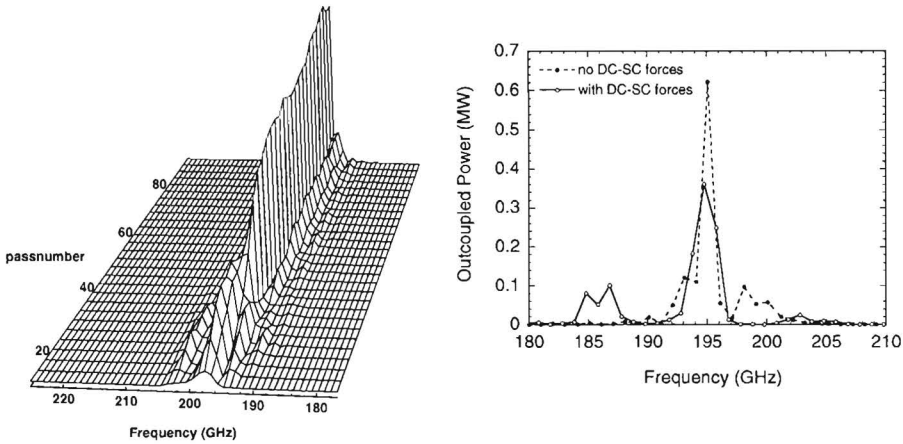
Figure 6.7: *The evolution of the power spectrum, from pass 10 to 90 in the case the longitudinal space-charge fields are included and the DC-force is disregarded. The reflection coefficient is wavelength independent; the gaplength is $1\frac{1}{2}\lambda_u$. In the figure on the right, the outcoupled power after 90 passes is shown as a function of frequency for the cases the DC-forces are whether or not disregarded.*

within a 4 GHz frequency interval. The corresponding electron efficiency is 5.5%. At the end of the first section 3.7% of the initial electron energy is transferred into microwave energy.

The single peaked spectrum is in contrast with the one when also the fast oscillating space-charge forces are omitted, see Fig. 4.4. In the latter case, a substantial sideband is generated at the lower frequency side. This shows that the longitudinal space-charge forces counteract the bunching process and, hence, reduce the gain. The reduction of the gain is favourable for the generation of single-peaked power spectra. The design parameters are such that with fast oscillating space-charge forces, the local growth of the microwave power in the first as in the second section leads to half a synchrotron oscillation of the electrons, while in the case where these space-charge fields are disregarded the electrons tend to perform more than half a synchrotron oscillation in the potential well, see Fig. 4.4. The latter is always accompanied by sideband generation.

In the figure on the right in Fig. 6.7, the spectra generated with and without the DC-forces are shown after the 100th pass. The total outcoupled power is approximately the same in both cases, 1.20 MW and 1.26 MW, respectively, and the main peaks in the power spectra are generated at the same frequency.

6.4   Discussion

In this Chapter it is shown that the amplitude and shape of the profile of the reflection coefficient have large influence on the power spectrum. With a broad profile, the power spectrum is less stable and evolves toward a multi-peaked spectrum. The profile of the reflection coefficient stabilises the power spectrum and suppresses the sidebands, provided that the maximum reflection is placed at the proper frequency. Employing a broad reflection profile, the output power exceeds the 1 MW level and the width in frequency of the signal is of the order of 15–20 GHz, which is a power spectrum consisting of multiple narrow peaks. These peaks appear at lower frequencies than the one of the main peak in the power spectrum. At higher frequencies than the frequency of the main peak, the power spectrum is completely suppressed. It has been discussed that the sideband is associated with the overbunching of the electrons. This suggests that a reduction of the reflection coefficient will prevent sidebands to appear. Indeed, numerical simulations have shown that for operation between 200 GHz and 250 GHz the sideband does not appear when the frequency independent reflection coefficient is 25% or less. For example, for operation around 200 GHz, the generated spectrum with lower reflection coefficient generates a narrow, single-peaked power spectrum that couples out 1.1 MW at 25% reflection and 0.85 MW at 20% reflection. The same behaviour of the power spectrum is observed for operation near 250 GHz. For operation around 130 GHz, the frequency independent reflection coefficient must decrease to 15% in order to confine the power spectrum to a single peak.

Another suggestion to stabilise the generated power spectrum while using a frequency independent reflection coefficient is to vary the length of the fieldfree gap between the two sections of the step-tapered undulator. The gain depends on the length of the gap, and, generally, the value of the maximum gain decreases when the length differs from $1\frac{1}{2}\lambda_u$. The effect of the lower gain is indeed a stabilising influence on the power spectrum. In this context, we would like to show a final result, where the FEM operates around 130 GHz with a frequency independent reflection coefficient and a gaplength of $1\frac{1}{4}\lambda_u$. This case may be compared with Fig. 6.1. The power spectrum is quasi-stable: the power spectrum hardly changes from pass to pass (like in Fig. 6.3), and there are multiple narrow peaks. This would be an example of stable three-colour operation.

In this Chapter we have also analysed the influence of the two types of space-charge forces, the fast oscillating space-charge force and the DC-force. The fast oscillating space-charge fields counteract the bunching process and reduce the gain. This has a stabilising effect on the power spectrum. At
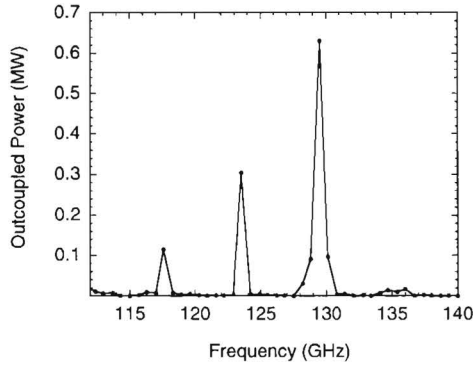
Figure 6.8: *The quasi-stable power spectrum for a frequency independent reflection coefficient and a gaplength of $1\frac{1}{4}\lambda_u$. The initial electron energy is $\gamma = 3.71$.*

saturation, the electrons are less overbunched at the end of the first section as well as at the end of the second section, so that the generation of sidebands is reduced. On average, the DC-forces lead to a larger radius for the electron beam. Also the betatron oscillation is modified by these forces. These DC-forces do not modify the ponderomotive potential well, but they have quite an influence on the power spectrum. Although the outcoupled power and the position of the main peak change marginally, the generated spectrum when disregarding these forces is much narrower with respect to the full simulation.

We mention here that when the frequency dependent reflection coefficient is considered and the DC-forces are disregarded, the power spectrum converges quickly towards a stable single peak. The maximum of the profile of the reflection coefficient must coincide with the position of the main peak in Fig. 6.7. The power spectrum in the stable regime couples out approximately the same power as was found including all space-charge forces, see Fig. 5.4. The single peak in the spectrum couples out 1.4 MW per pass within a frequency interval of 5 GHz.

References of Chapter 6

[1] D. Iracane and H. Delbarre, "Stability of a free-electron lasers spectrum in the continuous beam limit", Phys. Rev. Lett. **66** (1991) 33.

[2] D. Iracane, P. Chaix, and J.L. Ferrer, "Spectral behavior of high-power Compton free-electron lasers. I. Broadening and asymptotic equilibrium", Phys. Rev. E **49** (1994) 800.

[3] D. Iracane, P. Chaix, and H. Delbarre, "Spectral behavior of high-power Compton free-electron lasers. II. Effect on filtering and tapering on sideband generation", Phys. Rev. E **49** (1994) 815.

Summary

The Free-Electron Maser (FEM) is a source of intense, tuneable, microwave radiation. The active medium of a free-electron maser is a high-energy electron beam, that is deflected by the periodic force of an undulator. The periodic magnetic field of the undulator together with the microwave field generate a periodic potential well for the electrons. In this potential well the electrons are trapped. As the electrons emit radiation and loose energy, they become localised toward the bottom of the potential well. As a result, the electron beam density is periodically perturbed. This 'bunching' causes the emitted radiation to approximately add in phase. This process leads to the stimulated emission of radiation. When the density of the electron beam is large, the interaction becomes more complicated. The corresponding longitudinal space-charge field has the largest effect on the interaction. This field causes an outward force on the electrons in the bunches. Therefore, this field counteracts the bunching process. Another effect of the density is the DC-force that is associated with the equilibrium current density. This force causes the cross section of the electron beam to be larger on average and modifies the betatron oscillations.

The first FEM is currently being constructed at the FOM-Institute for plasma physics 'Rijnhuizen'. The generated microwave radiation will be used for heating of magnetised plasmas. For the FEM to be a success, generation of high power microwave radiation within a small frequency bandwidth is crucial. There are many reasons why an investigation of the spectral behaviour of the FEM is necessary. An important reason is that the FEM is equipped with a step-tapered undulator, consisting of two sections with different strengths and lengths that are separated by a field free gap. This undulator can provide high efficiency at high output power, but the different resonance conditions in the two sections might lead to multi-peaked power spectra. The FEM is equipped with a low-quality cavity for the microwave field, that couples out 71% of the microwave power each roundtrip.

We have developed a multi-frequency model of the FEM. The solution is numerically determined by means of a newly developed Multi-Frequency FEM code that is called MFF. This code calculates the electron trajectories in the six-dimensional phase-space in the presence of the microwave field and all relevant space-charge fields. The latter fields consist of the longitudinal, fast oscillating space-charge fields that counteract the bunching process and the DC-forces associated with the equilibrium electron beam density. The equations are not averaged over an undulator period and slippage of the electrons with respect to the microwave field is included.

The operating frequency of the microwave radiation can be adjusted over

the entire frequency range from 130 GHz to 250 GHz. This is accomplished by changing the electron energy and simultaneously adjusting the centre frequency of the profile of the reflection coefficient. Numerical calculations of the FEM with the experimentally determined (narrow) profile of the reflection coefficient are done in the entire frequency range. It is found that the power spectrum depends critically on the centre frequency of the profile of the reflection coefficient. In order to have most stable operation with highest outcoupled power, this centre frequency must be put a few GHz below the frequency that corresponds to maximum linear gain. The generated power exceeds the 1 MW and the power is generated within a frequency range of a few percent of the central frequency. When the central frequency and the amplitude of the reflection coefficient is fixed, the operating frequency can be changed over a few percent by changing the electron energy. Experimentally, this can be done within a few milliseconds. We have investigated the evolution of the power spectrum when the electron energy is slightly changed and the reflection coefficient is fixed. It is found that a shift of the operating frequency by $2\frac{1}{2}\%$ leads to a drop in efficiency of 20%. The outcoupled must remain more than 1 MW, this way, the operating frequency may be changed over 5%.

The dynamics of the power spectrum generated in the FEM is studied with and without the effects of the space-charge fields and with a frequency independent reflection coefficient. In the small-signal regime, the microwave radiation is generated over a broad spectrum and the linear growth rate of the microwave power as a function of frequency has several peaks. The gain is quite large and the large-signal regime is quickly reached. During the transition from the small-signal to the large-signal regime mode-competition occurs. At first, a peak is generated in the power spectrum at the frequency of maximum linear gain. When the system enters the saturated regime, this peak shifts toward a lower frequency that is located around the frequency corresponding to maximum nonlinear gain. In the large-signal regime, the power spectrum at frequencies larger than the one of the main peak is completely suppressed in all cases. It is observed that as soon as the electrons start to overbunch, i.e. the electrons start to absorb energy from the microwave field, a large sideband is generated at the lower frequency side of the main peak. The behaviour of the multi-peaked power spectrum is investigated as a function of some parameters, such as the reflection coefficient and the length of the gap between the two undulator sections. Reducing the reflection coefficient reduces the generation of the sidebands and stabilises the evolution of the power spectrum.

Spectraal Gedrag van Vrije-Electronen Masers

In dit proefschrift worden aspecten van de vrije-electronen maser (FEM) beschreven. Dit is een laser die millimeter straling maakt met een hoog vermogen. De straling wordt gemaakt door een bundel electronen door een periodieke magnetische structuur, de undulator, te sturen. De electronen hebben zo'n hoge energie dat ze bijna met de lichtsnelheid bewegen. Hierdoor kunnen de electronen even snel bewegen als de potentiaal put, die is gevormd door de gecombineerde velden van de undulator en de millimeter straling. Als de electronen door de versnelde beweging stralen, verliezen ze energie en vallen naar de bodem van de potentiaalput. De hiermee samenhangende klontering van de electronen zorgt ervoor dat de fase van de door de individuele electronen uitgezonden straling ongeveer dezelfde is. Dit leidt tot 'gestimuleerde' emissie. Als de electronen dichtheid groot is, treden er complicerende effecten op. De grootste invloed op de interactie is van het longitudinale ruimteladings veld. De hiermee samenhangende kracht drijft de geklonterde electronen uit elkaar. De vorming van straling wordt dus tegengewerkt. Een andere invloed van de dichtheid is de DC-kracht, die samenhangt met de evenwichtsdichtheid van de electron bundel. Deze DC-kracht maakt de electronbundel gemiddeld breder.

De eerste FEM wordt gebouwd op het FOM-Instituut voor Plasmafysica 'Rijnhuizen'. De straling zal worden gebruikt voor de verhitting van magnetisch opgesloten plasma's. Hiertoe is het belangrijk dat de straling van de FEM in een nauwe frequentie bandbreedte wordt geëmiteerd. Er zijn redenen om aan te nemen dat de FEM wel eens een breed spectrum zou kunnen genereren. Zo wordt bijvoorbeeld in de FEM een undulator gebruikt die bestaat uit twee losse undulatoren met verschillende sterkte en lengte, welke zijn gescheiden door een gat zonder magneetveld. De twee delen van de undulator hebben verschillende resonantiefrequenties, waardoor een spectrum zou kunnen worden gemaakt bestaande uit meerdere pieken. Om de evolutie van het vermogensspectrum te bestuderen hebben wij een multifrequentie model gemaakt. De oplossing van dit model wordt numeriek bepaald door middel van een simulatieprogramma dat door ons is ontwikkeld. Dit programma berekent de gegenereerde electromagnetische velden en de banen die de electronen beschrijven in de driedimensionale ruimte. De velden bestaan uit zowel het stralingsveld als uit alle relevante ruimteladingsvelden.

Het spectrale gedrag van de vrije electronen maser is bestudeerd met een frequentie-onafhankelijke reflectiecoëfficiënt. In het laagvermogen regime wordt straling gegenereerd over een breed spectrum. De lineaire groeisnelheid van het microgolfvermogen als functie van de frequentie heeft meerdere

pieken. Bij hoger vermogen wordt de groei niet-lineair en treedt er heftige competitie tussen de diverse frequentie componenten op. Bij het opstarten van de FEM wordt eerst een piek in het vermogensspectrum gegenereerd bij de frequentie met maximale lineaire groei. Bij hoog vermogen verschuift deze piek naar lagere frequenties. Zodra de electronen de maximale energie hebben afgegeven en dan weer energie van het stralingsveld gaan absorberen, wordt er naast de nauwe piek in het spectrale vermogen ook een zijband gegenereerd. Het vermogen in deze parasitaire piek kan groeien tot een kwart van het totale vermogen. Er is onderzocht hoe deze parasitaire piek zou kunnen worden onderdrukt. Dit kan bijvoorbeeld worden gedaan door de reflectiecoëfficiënt te verlagen.

De frequentie waarop de FEM werkt kan worden gevarieerd in het frequentie interval van 130 GHz–250 GHz. Hiertoe moet zowel de energie van de electronen als de centrale frequentie van het profiel van de reflectiecoëfficiënt worden aangepast. Er zijn simulaties gedaan die het experimenteel gemeten profiel voor de reflectiecoëfficiënt gebruiken. Deze simulaties voorspellen dat de FEM in het hele domein van 130 GHz tot 250 GHz straling genereert in een nauwe, enkele piek in het vermogensspectrum. Het uitgekoppelde vermogen komt ruim boven de 1 MW. Als de FEM inderdaad dit vermogensspectrum gaat genereren zou dat een zeer succesvolle werking van het apparaat zijn. De positie van het profiel voor de reflectiecoëfficiënt is kritisch voor een stabiele en optimale werking van de FEM. De centrale frequentie van het profiel moet een paar GHz lager worden geplaatst dan de frequentie waarbij maximale lineaire groei optreedt. Experimenteel kan een zeer snelle verandering van de frequentie binnen millisecondes worden bereikt door alleen de electron energie te variëren. Op deze manier blijft de reflectiecoëfficiënt onveranderd en kan de frequentie waarop de FEM werkt worden versteld. Dit gaat wel ten koste van het uitgekoppelde vermogen, want een verandering van frequentie van $2\frac{1}{2}$% leidt tot een afname van het uitgekoppelde vermogen met 20%. Als wordt verlangd dat de FEM meer dan 1 MW moet blijven leveren, kan de frequentie op deze manier met maximaal 5% worden veranderd.

Dankwoord

Het vier jaar durende onderzoek dat heeft geleid tot dit proefschrift zou niet zo succesvol zijn geweest zonder de hulp en steun van veel mensen. Hierbij bedank ik iedereen die interesse voor mijn promotieonderzoek heeft getoond en heeft geholpen bij het afronden van dit proefschrift.

Ik bedank mijn promotor en dagelijkse begeleider Theo Schep voor zijn hulp en steun. Henk Hagedoorn ben ik erkentelijk voor zijn bereidheid als tweede promotor op te treden.

I would like to thank Andre Tulupov for the help and interest in my investigations. He shared his broad knowledge and insight of the FEM with me. The various discussions with Malcolm Caplan were quite usefull.

Alle kasteel-'Rijnhuizen'-bewoners en andere collega's hebben voor een gezellige en plezierige werkomgeving gezorgd. Bart Faatz bedank ik voor de vele discussies die tot op heden zijn blijven bestaan. Met mijn kamergenoten Gertjan van Werkhoven en Ronald Nijboer heb ik een gezellige tijd gehad.

Waldo Bongers heeft het profiel van de reflectiecoëfficiënt gemeten. Deze experimentele resultaten heb ik gebruikt in dit proefschrift.

Helma en Christine bedank ik voor hun liefde en vrolijkheid, mijn ouders voor hun aandacht, mijn schoonouders, Marc, Arjan en Marnix voor hun interesse. Het is voor mij een eer dat beide opa's van onze dochter Christine paranimf willen zijn en mij willen bijstaan tijdens de verdediging van dit proefschrift.

Curriculum Vitae

7 oktober 1967	Geboren te Harenkarspel.
1980 · 1986	Ongedeeld VWO aan de openbare scholengemeenschap 'Huygenwaard' te Heerhugowaard.
1986 – 1992	Studie Natuurkunde aan de Universiteit van Amsterdam. Afstudeerrichting theoretische natuurkunde. Afstudeerproject bij prof.dr. J. Smit getiteld: 'Strongly Coupled QED'.
1992 – 1996	Promotieonderzoek aan het FOM-Instituut voor Plasmafysica 'Rijnhuizen'. Promotor: prof.dr.ir. T.J. Schep. De resulaten zijn beschreven in dit proefschrift.

Stellingen

behorende bij het proefschrift

Spectral Behaviour

of

Free Electron Masers

Pieter Jan Eecen

Eindhoven, 28 november 1996

De tweede sectie van de undulator van de FOM-FEM is belangrijk als versterker van de straling die is gegenereerd in de eerste sectie. In verzadiging wordt het spectrale vermogen nabij de resonante frequentie van de tweede sectie altijd onderdrukt door de interactie. In tegenstelling tot beweringen van A.A. Varfolomeev and T.V. Yarovoi zijn de pieken in de lineaire gain kromme nabij deze frequentie niet van belang voor het spectrale gedrag bij verzadiging.

A.A. Varfolomeev and T.V. Yarovoi, *FEL gain as a function of phase displacement induced by undulator intersection gaps* Nucl. Instr. and Meth. A 375 (1996) 352;
Dit proefschrift, hoofdstukken 4, 5 en 6.

Als het spectrale gedrag van de FOM-FEM overeenkomt met de voorspellingen die zijn beschreven in dit proefschrift, betekent dit een gezamenlijk succes voor dit proefschrift en voor de FOM-FEM.

Dit proefschrift.

De FOM-FEM werkt in een gebied tussen de Compton en de Raman limiet. Er is een verschil tussen de frequenties corresponderend met maximale groei in het laag-vermogen gebied en maximale groei in het hoog-vermogen gebied van de FEM. Dit verschil neemt toe wanneer de frequentie waarmee de FOM-FEM werkt hoger wordt. In de Compton limiet zou dit andersom zijn. De verklaring voor dit effect kan worden toegeschreven aan de mate waarin de ruimteladingskrachten belangrijk zijn.

Dit proefschrift, hoofdstukken 2 en 5.

Het nauwe frequentieprofiel van de reflectiecoefficient van de FOM-FEM is essentieel voor het opwekken van straling binnen een enkele, nauwe piek in het vermogensspectrum. Dit profiel is tevens de oorzaak dat de snelle verstembaarheid van de FOM-FEM (binnen microsecondes) is beperkt tot 5% van de werkfrequentie.

Dit proefschrift, hoofdstuk 5.

-V-

Het computersysteem van het Regionaal Bureau voor de Arbeidsvoorziening kan niet worden beveiligd tegen oneigenlijk gebruik zolang een werknemer van het RBA onder de ogen van (toekomstige) uitkeringsgerechtigden zijn naam en wachtwoord invoert.

-VI-

Resultaten van numerieke berekeningen die vanwege vertrouwelijkheid van het computerprogramma en het onderliggende model niet nagerekend kunnen worden door derden dienen te worden afgewezen voor wetenschappelijke publicatie.

-VII-

Eerbiediging van de persoonlijke levenssfeer is een grondrecht. Het is niet zo zeer de voortgaande technische ontwikkeling die een gevaar vormt voor de privacy van sommige in Nederland verblijvende personen, als wel de wetgeving die steeds meer een inbreuk op de privacy mogelijk maakt.

-VIII-

Het streven van banken om 'global players' te worden leidt tot het veronachtzamen van de wensen van de individuele cliënt en speelt derhalve gespecialiseerde banken in de kaart.

P. Jagersma, Trouw, 14-9-1995

-IX-

Het openbaar ministerie is bereid grote sommen geld te betalen aan kroongetuigen in strafzaken. Als reactie hierop is inmiddels ook een verdachte hiertoe bereid. Los van het feit dat het betalen van getuigen tot meineed zou kunnen leiden werkt deze ontwikkeling klassejustitie in de hand.

-X-

Eigen waarneming heeft bevestigd dat in de Amsterdam Arena de kwaliteit van de grasmat en de aanmoedigingen van de supporters benedenmaats zijn. Opzwepend enthousiasme van het publiek zal de voetbalspelers vleugels geven. Dit zal de grasmat ten goede komen.